

## Copyright Warning & Restrictions

The copyright law of the United States (Title 17, United States Code) governs the making of photocopies or other reproductions of copyrighted material.

Under certain conditions specified in the law, libraries and archives are authorized to furnish a photocopy or other reproduction. One of these specified conditions is that the photocopy or reproduction is not to be “used for any purpose other than private study, scholarship, or research.” If a user makes a request for, or later uses, a photocopy or reproduction for purposes in excess of “fair use” that user may be liable for copyright infringement,

This institution reserves the right to refuse to accept a copying order if, in its judgment, fulfillment of the order would involve violation of copyright law.

**Please Note: The author retains the copyright while the New Jersey Institute of Technology reserves the right to distribute this thesis or dissertation**

Printing note: If you do not wish to print this page, then select “Pages from: first page # to: last page #” on the print dialog screen



The Van Houten library has removed some of the personal information and all signatures from the approval page and biographical sketches of theses and dissertations in order to protect the identity of NJIT graduates and faculty.

## ABSTRACT

### STUDIES OF SOLAR WHITE-LIGHT FLARES AND SMALL-SCALE MAGNETIC STRUCTURES OBSERVED IN THE NEAR INFRARED

by  
Yan Xu

Using the most advanced infrared imaging technology as developed by NJIT, detailed study of solar white-light flares and small magnetic structures, such as faculae and pores, are presented in this dissertation. The investigations focus on near-infrared observations at  $1.56 \mu\text{m}$ , which are good proxy of the deepest layer of the solar photosphere.

I made fundamental contributions in two areas of near infrared (NIR) solar physics: (1) the first detection and understanding of white-light flares in the NIR and (2) clearly demonstrated non-existence of “dark faculae”. Several high-resolution observations have been carried out at BBSO and National Solar Observatory/Sacramento Peak. The data benefited from a newly developed state-of-the-art near-infrared photometric system and the high-order adaptive optics system. In addition to the near-infrared observations, visible continuum and G-band images were obtained simultaneously, as well as the data from satellites, such as Michelson Doppler Imager (MDI) on board the Solar and Heliospheric Observatory (SoHO) and the Ramaty High Energy Solar Spectroscopic Imager (*RHESSI*), were acquired for comparison.

For flare study, the very first near-infrared observations of two white-light flares are presented. The flare morphology and dynamics are briefly summarized as follows: (1) Significant intensity enhancements appeared in the near-infrared and visible continua and G-band. The maximum intensity enhancements are much higher than the prediction of any existing models: 25% to 66% of the NIR continuum and 45% to 76% for the visible white-light; (2) The flares were typical two ribbon flares. During the impulsive phase, two major flare ribbons moved apart. The flare ribbons in the near-infrared and other wavelengths were both temporally and spatially well correlated with *RHESSI* hard X-ray; (3) All ribbons

showed a brighter core surrounded by a faint halo structure. The ribbon separation speeds were about 28 km/s in the first and 24 km/s in the second event based on NIR observations. The derived electric fields in the reconnection current sheet  $E_c$  are about 23 V cm<sup>-1</sup> and 22 V cm<sup>-1</sup>, respectively; (4) The NIR emission and the impulsive HXR emission up to 800 keV were well correlated with a small delay of less than two minutes; (5) The high resolution and high cadence images gave us the first chance to measure the cooling time of flares at photospheric height. We found that the cooling process could be characterized by two steps: A quick temperature drop, which is related to the cooling process of the bright cores, and a relatively slow decay related to the halo structures. The time scale is in the order of less than 30 seconds and a few minutes for these two steps, respectively. The findings and results can be explained by combination of several existing models.

The high-resolution data are also used for the study of small magnetic structures. Images observed in different wavelengths represent the properties of faculae or pores in different layers of the solar atmosphere from the bottom of the photosphere using near-infrared at 1.56  $\mu\text{m}$  to the upper photosphere using G-band. Both statistical studies and individual examinations show that the contrasts of faculae and pores have the same sign in both the near-infrared and visible continua. In other words, no so-called “dark faculae” that are bright in the visible but dark in the near-infrared was found. The previously observed “dark faculae” are most likely unresolved pores or due to non-simultaneous observations. In addition, a threshold for the magnetic flux density that separates pores from faculae was determined.

**STUDIES OF SOLAR WHITE-LIGHT FLARES AND SMALL-SCALE  
MAGNETIC STRUCTURES OBSERVED IN THE NEAR INFRARED**

by  
**Yan Xu**

**A Dissertation  
Submitted to the Faculty of  
New Jersey Institute of Technology and  
Rutgers, the State University of New Jersey - Newark  
in Partial Fulfillment of the Requirements for the Degree of  
Doctor of Philosophy in Applied Physics**

**Federated Physics Department**

**August 2005**

**Copyright © 2005 by Yan Xu  
ALL RIGHTS RESERVED**

**APPROVAL PAGE**

**STUDIES OF SOLAR WHITE-LIGHT FLARES AND SMALL-SCALE  
MAGNETIC STRUCTURES OBSERVED IN THE NEAR INFRARED**

**Yan Xu**

---

Dr. Haimin Wang, Dissertation Advisor Date  
Distinguished Professor of Physics, Associate Director of the Center for  
Solar-Terrestrial Research and the Big Bear Solar Observatory, NJIT

---

Dr. Carsten Denker, Dissertation Co-advisor Date  
Assistant Professor of Physics, NJIT

---

Dr. Philip R. Goode, Committee Member Date  
Distinguished Professor of Physics, Director of the Center for  
Solar-Terrestrial Research and the Big Bear Solar Observatory, NJIT

---

Dr. Dale E. Gary, Committee Member Date  
Professor of Physics, Director of the Solar  
Array in Owens Valley Radio Observatory, NJIT

---

Dr. Zhen Wu, Committee Member Date  
Associate Professor of Physics, Department Chair,  
Rutgers University, Newark

## BIOGRAPHICAL SKETCH

**Author:** Yan Xu  
**Degree:** Doctor of Philosophy  
**Date:** August 2005

### Undergraduate and Graduate Education:

- Doctor of Philosophy in Applied Physics,  
New Jersey Institute of Technology, Newark, New Jersey, 2005
- Bachelor of Science in Astrophysics,  
University of Science and Technology of China, Hefei, Anhui, China, 1998

**Major:** Applied Physics

### Publications in Refereed Journals:

- Yan Xu, Wenda Cao, Jun Ma, Klaus Hartkorn, Ju Jing, Carsten Denker, and Haimin Wang, 2005, *Search for Dark Faculae using New 2.5 Å Bandpass NIR Lyot Filter*, *Astrophysical Journal*, 628, 167.
- Yan Xu, Wenda Cao, Chang Liu, Guo Yang, Ju Jing, Carsten Denker, and Haimin Wang, 2005, *High Resolution Observations of Multi-Wavelength Emissions During Two X-class White-Light Flares*, *Astrophysical Journal*, submitted.
- Yan Xu, Wenda Cao, Chang Liu, Guo Yang, Jiong Qiu, Ju Jing, Carsten Denker, and Haimin Wang, 2004, *Near-Infrared Observations at 1.56 Microns of the 2003 October 29 X10 White-Light Flare*, *Astrophysical Journal*, 607, 131.
- Yan Xu, Guo Yang, Jiong Qiu, Tom J. Spirock, Ju Jing, Carsten Denker, and Haimin Wang, 2004, *Visible and Near-Infrared Contrast of Faculae in Active Region NOAA 8518*, *Chinese Journal of Astronomy and Astrophysics* 4, 481.
- Jiong Qiu, Gordon Hurford, Yan Xu, and Haimin Wang, 2005, *RHESSI Observations of Solar Flare Elementary Bursts*, *Astrophysical Journal*, submitted
- Wenda Cao, Klaus Hartkorn, Jun Ma, Yan Xu, Jingshan Wang, Thomas J. Spirock, and Haimin Wang, 2005, *First Light for the Near-Infrared Narrow-Band Tunable Birefringent Filter of Big Bear Solar Observatory*, *Solar Physics*, submitted.
- Ju Jing, Jiong Qiu, Jun Lin, Ming Qu, Yan Xu and Haimin Wang, 2005, *Magnetic Reconnection Rate and Flux-Rope Acceleration of Two-Ribbon Flares*, *Astrophysical Journal*, 620, 1085.
- Guo Yang, Yan Xu, Wenda Cao, Haimin Wang, Carsten Denker, and Thomas R. Rimmele, 2004, *Photospheric shear flows along the magnetic neutral line of Active Region NOAA 10486*, *Astrophysical Journal*, 617, 151.

- Carsten Denker, Dulce Mascarinas, Yan Xu, Wenda Cao, Guo Yang, Haimin Wang, and Philip R. Goode, 2004, *High-Spatial Resolution Imaging Combining High-Order Adaptive Optics, Frame Selection, and Speckle Masking Reconstruction*, *Solar Physics*, 227, 217.
- Ju Jing, Vasyl B. Yurchyshyn, Guo Yang, Yan Xu, and Haimin Wang, 2004, *On the Relation between Filament Eruptions, Flares, and Coronal Mass Ejections*, *Astrophysical Journal*, 614, 1054.
- Guo Yang, Yan Xu, Haimin Wang, and Carsten Denker, 2003, *High Spatial Resolution Observations of Pores and The Formation of A Rudimentary Penumbra*, *Astrophysical Journal*, 597, 1190.
- Ju Jing, Jeongwoo Lee, Thomas J. Spirock, Yan Xu, and Haimin Wang, 2003, *Periodic Motion Along A Solar Filament Initiated by A Subflare*, *Astrophysical Journal*, 584, 103.

To my wife, Xiaoyan; parents, Jingshan Xu and Ximin Lu.

## ACKNOWLEDGMENT

With the deepest sense of gratitude, I would like to express my sincere thanks to Dr. Haimin Wang, my thesis advisor, for his immense help, encouragement and personal guidance in all the time of my research. His wide knowledge and integral view of research has deeply impressed me. I am really glad to have him be my advisor.

I would like to thank Dr. Carsten Denker, my co-advisor, who was always available for detailed instructions and stimulating suggestions. His rigorous style of research has deeply indebted me to him.

I thank Dr. Philip R. Goode, Dr. Dale E. Gary and Dr. Zhen Wu for reviewing my dissertation, giving feedback and spending time to be my thesis committee members.

My acknowledgment would not be complete without mentioning Dr. Jiong Qiu. She spent a lot of time helping me with programming and giving constructive suggestions on all the aspects of my studies. I am also grateful to Dr. Wenda Cao, not only for his great help on instrumentations and observations, but also for his friendship.

During this work, I have collaborated with many colleagues. I wish to thank Dr. Guo Yang, who led me in my first observing run at Big Bear Solar Observatory; Chang Liu, for his valuable discussion and contributions, especially in the research of solar flares. Also, I would like to thank Drs. Thomas J. Spirock, Klaus Hartkorn, Ju Jing and Mr. Ming Qu for their support and friendship.

I welcome the opportunity to give my thanks to the observing staffs at Big Bear Solar Observatory and National Solar Observatory at Sacramento Peak, for their remarkable support and assistance. I warmly thank Dr. Matt Penn of National Solar Observatory/Kitt Peak. He shared his observing time with me and therefore gave us the opportunity to test our new instrument in advance.

My special gratitude is due to my parents Jingshan Xu and Ximin Lu. Their support and courage allowed me to finish this work.

Especially, I owe my loving thanks to my wife Xiaoyan Wang for her inspiration and moral support. The completion of this work is under her understanding and love.

This work is supported by grants from NSF, NASA, and Air Force.

# TABLE OF CONTENTS

<b>Chapter</b>	<b>Page</b>
1 INTRODUCTION . . . . .	1
1.1 The Sun . . . . .	1
1.1.1 Overview . . . . .	1
1.1.2 Observing the Sun . . . . .	4
1.2 Solar Flares . . . . .	5
1.2.1 Overview . . . . .	5
1.2.2 Magnetic Fields and Solar Flares . . . . .	9
1.2.3 Particle Acceleration . . . . .	15
1.2.4 Hard X-ray Emission . . . . .	16
1.3 Small-Scale Magnetic Features . . . . .	18
1.3.1 Magnetic Flux Tubes . . . . .	19
1.3.2 Bright Points . . . . .	27
1.4 Observations in the Near-Infrared Spectral Range . . . . .	30
1.4.1 Better Seeing Conditions . . . . .	31
1.4.2 Opacity Minimum . . . . .	35
1.4.3 Less Requirements for Adaptive Optics System . . . . .	36
1.4.4 Less Scattered Light . . . . .	37
1.4.5 Larger Zeeman Splitting . . . . .	37
1.4.6 Other Advantages and Some Issues of the NIR Observation . . . . .	37
1.5 Outline of this Dissertation . . . . .	39
2 WHITE-LIGHT FLARES OBSERVED IN THE NEAR-INFRARED . . . . .	42
2.1 Abstract . . . . .	42
2.2 Introduction . . . . .	42

**TABLE OF CONTENTS**  
**(Continued)**

<b>Chapter</b>	<b>Page</b>
2.2.1 White-Light Flares . . . . .	42
2.2.2 The Flare Emission Models . . . . .	43
2.2.3 Our New Observations . . . . .	47
2.3 Observation and Data Reduction . . . . .	48
2.3.1 The New Near-Infrared Camera . . . . .	48
2.3.2 The Telescope . . . . .	50
2.3.3 The Setup and Data Reduction . . . . .	50
2.4 Results . . . . .	55
2.4.1 Overview of the Flares . . . . .	55
2.4.2 Comparison of NIR with HXRs . . . . .	58
2.4.3 Comparison of NIR, Visible and G-band . . . . .	64
2.4.4 Flare Dynamics and Electric Field in the Reconnection Region . . . . .	67
2.4.5 Cooling Time . . . . .	69
2.5 Summary and Discussion . . . . .	71
<b>3 PROPERTIES OF FINE MAGNETIC STRUCTURES . . . . .</b>	<b>73</b>
3.1 Abstract . . . . .	73
3.2 Introduction . . . . .	74
3.3 First Approach of Searching Dark Faculae . . . . .	77
3.3.1 Observation . . . . .	77
3.3.2 Data Analysis and Result . . . . .	82
3.3.3 Discussion . . . . .	89
3.4 Second Approach of Searching Dark Faculae Using the Newly Developed Narrow Bandpass Lyot Filter . . . . .	89

**TABLE OF CONTENTS**  
**(Continued)**

<b>Chapter</b>	<b>Page</b>
3.4.1 Observation . . . . .	89
3.4.2 Data Analysis and Result . . . . .	97
3.4.3 Discussion . . . . .	101
4 SUMMARY . . . . .	102
REFERENCES . . . . .	104

## LIST OF TABLES

<b>Table</b>	<b>Page</b>
1.1 The Visible Importance Classification . . . . .	8
1.2 The Soft X-ray Flare Classification . . . . .	8
2.1 Specifications of the Rockwell Infrared Camera. . . . .	49
2.2 Setup Details of the October-November Observing Run, 2003. . . . .	53
2.3 Basic Measurements of Two WLFs. . . . .	57
3.1 Calibration Coefficients. . . . .	84
3.2 Sensor Specifications of the NIR SU320-1.7RT In Ga As Camera. . . . .	84
3.3 Magnetic Threshold Values. . . . .	87
3.4 Design Requirements of the Lyot Filter System. . . . .	93
3.5 Observation Details and Comparison with Previous Observations . . . . .	98

## LIST OF FIGURES

Figure	Page
1.1 Views of the Sun ( <a href="http://sohowww.nascom.nasa.gov/">http://sohowww.nascom.nasa.gov/</a> , 2005 August 10.), Courtesy: SoHO/MDI . . . . .	2
1.2 Absorption effect in the Earth’s atmosphere. ( <a href="http://www.ipac.caltech.edu">http://www.ipac.caltech.edu</a> , 2005 August 1.) . . . . .	5
1.3 Light curves in different wavelengths during a “typical flare”. <i>x</i> -axis denotes the time (minute). Adapted from (Golub & Pasachoff 1997) . . . . .	7
1.4 This figure shows several solar flares detected by NOAA satellite (GOES) in July 2005 including an X1.2, an M5, an M3.2 and few C-class flares. . . . .	8
1.5 Photospheric flows and magnetic field configuration of active region NOAA 10486 observed on 2003 October 29. To illustrate the high spatial resolution local correlation tracking results, we provide different views of (a) flow vectors, (b) azimuth angle of the velocity vectors, (c) magnitude of the velocity vectors, and (d) MDI magnetogram with superposed magnetic neutral lines. See Yang et al. (2004) . . . . .	11
1.6 Schematic diagram of a disrupted magnetic field that forms in an eruptive process. Colors are used to roughly denote the plasma layers in different temperatures. This diagram incorporates the two-ribbon flare configuration of Forbes & Acton (1996) and the CME configuration of Lin & Forbes (2000). . . . .	13
1.7 Schematic reconnection to explain rapid magnetic field changes associated with solar flares. (a) Initial magnetic field configuration before the flare. Penumbra fields are in gray and umbral areas are in black. (b) Magnetic field configuration after the flare. Dashed-dotted line represents the connection of a dipolar area far away from the neutral line (Liu et al. 2005). . . . .	14
1.8 Schematic diagram of an electron swing-by around a proton. . . . .	17
1.9 Two sunspots are shown in this figure. They were observed at 18:52:48 UT (Top) and 18:44:54 UT (Bottom) on 2003 November 2. The lower one is much larger and more complex than the one at the top. . . . .	21
1.10 The cluster model of a sunspot proposed by Parker (1979). . . . .	22
1.11 A cartoon showing both the sound-speed variations and the subsurface flow patterns of a sunspot (Courtesy: SoHO/MDI). Adapted from Zhao (2004b) . . . . .	23
1.12 This figure shows the full disk line-of-sight magnetogram from SoHO/MDI obtained at 17:00:02 UT on 2005 July 1. . . . .	24

**LIST OF FIGURES**  
(Continued)

<b>Figure</b>	<b>Page</b>
1.13 Vertical cut of a magnetic flux tube. The thick curve at $z = 0$ denotes the optical depth in the photosphere where $\tau_{5000} = 1$ . See Steiner et al. (2001). . . . .	26
1.14 This figure shows MDI magnetograms obtained from 2003 October 26 to 2003 November 2. The areas marked with red circles indicate the formation of a sunspot from several small spots. The two blue ellipses refer to the flare areas on 2003 October 29 and November 2. . . . .	28
1.15 Images of Active Region NOAA 10486 obtained at 20:33:28 UT in the G-band (Top) and 20:34:19 UT in the visible continuum (Bottom) on 2003 October 29. Two small images show the sub-areas marked with white boxes in the larger images, which contain bright facular points. . . . .	29
1.16 Picture of the dome and the causeway at the Big Bear Lake. This figure is from <a href="http://bbso.njit.edu">http://bbso.njit.edu</a> , 2005 August 1 . . . . .	33
1.17 The BBSO 65 cm reflecting telescope and three refracting telescopes (15 cm, 20 cm, and 25 cm). (From <a href="http://bbso.njit.edu">http://bbso.njit.edu</a> , 2005 August 1.) . . . . .	34
1.18 This plot shows the total opacity at the photospheric level due to $H^-$ absorption including bound-free transition (dotted-dashed line) and free-free transition (dashed line). (Adapted from the class notes of Dr. Sitko in the Department of Physics, University of Cincinnati, more details can be found in Doughty & Fraser (1966a); Doughty et al. (1966b).) . . . . .	36
1.19 The basic setup showing the working-principle of the Adaptive Optics System at NSO/SP. For a detailed description of the AO system, see Hartkorn (2003); L'ena et al. (1998). . . . .	38
2.1 The rockwell NIR camera, mounted in the optical table behind the interference filter and NDs. . . . .	49
2.2 Setup diagram of the October-November observing run in 2003. . . . .	51
2.3 A picture showing the real setup of Figure 2.2. . . . .	52

**LIST OF FIGURES**  
(Continued)

<b>Figure</b>	<b>Page</b>	
2.4	Upper Panel: Speckle reconstructed image of active region NOAA 10486 obtained with frame selection and high-order AO system at 16:48 UT on 2003 October 29. The annotation of the axes refers to heliographic coordinates corresponding to a FOV of $81 \times 81''$ . Lower Panel: NIR image of the same active region during the flare taken on 20:42 UT with a FOV of $91 \times 91''$ . The bright patches marked by white boxes are NIR flare kernels. . . . .	54
2.5	NIR time sequence of the X10 flare from 20:40 UT to 20:47 UT on 2003 October 29. RHESSI HXR contours (blue) correspond to the 50 - 100 keV channel with 60 integration. The local NIR intensity maxima are shown in red. Two flare ribbons are correlated with strong HXR kernels. HXR contour levels are drawn at 0.17, 0.25, 0.60, and 0.80 of the maximum intensity, except for the first two frames, where they correspond to 0.7 and 0.8 for the first frame and 0.4, 0.6, and 0.8 for the second, when the HXR kernels were weaker. . . .	59
2.6	Light-curves of the contrasts for the NIR and HXR flux in the X10 flare on October 29, 2003 (upper panel), and X8 flare on November 2, 2003 (lower panel). The lowest plot in lower panel shows the seeing variation in the second event. In the lower panel, the error for NIR ALC (red) is $\pm 0.02$ , for NIR MLC (black) is $\pm 0.031$ . . . . .	60
2.7	Light-curves of the contrasts for the NIR and HXR flux in the X10 flare on October 29, 2003 (upper panel), and X8 flare on November 2, 2003 (lower panel). The lowest plot in lower panel shows the seeing variation in the second event. In the lower panel, the error for NIR ALC (red) is $\pm 0.02$ , for NIR MLC (black) is $\pm 0.031$ . . . . .	63
2.8	Short-exposure images of active region NOAA 10486 obtained with frame selection and HOAO system at 20:42 UT on 2003 October 29 (left) and at 17:17 UT on 2003 November 2 (right). October 29. (top) NIR, (middle) visible (bottom) G-band. In each column (event), the FOVs are the same for all three wavelengths. . . . .	65
2.9	Background-subtracted difference images in the NIR (top), visible (middle) and G-band (bottom) on 2003 October 29 (left) and 2003 November 2 (right). Images in the left column (first event) are scaled between $\pm 0.35$ , images in right column (second event) are scaled $\pm 1.0$ . . . . .	66
2.10	Color-encoded NIR difference images showing the temporal evolution of the flare ribbons from 20:40 UT to 20:47 UT. The background is an MDI line-of-sight magnetogram. . . . .	68

**LIST OF FIGURES**  
(Continued)

<b>Figure</b>	<b>Page</b>
2.11 NIR and G-band light-curves of selected regions during flare peaks. (A1) to (A4) shows NIR cooling patterns during the first event, (C1) to (C4) are corresponding G-band curves during the first event and (D1) to (D4) are corresponding NIR in the second event. . . . .	70
3.1 Diagram shows the physics why dark faculae are dark. . . . .	76
3.2 NIR images of active region NOAA 8518 observed on April, 1999. (a) April 19, (b) April 20, (c) April 21, (d) April 25, (e) April 26, and (f) April 27. . . . .	79
3.3 MDI magnetograms taken from April 19 to 27, 1999. The white box shows the similar FOV of IR images in Figure 3.3. The magnetograms were scaled between $-400$ G and $+250$ G. . . . .	80
3.4 The NIR In Ga As camera. (From the web site of Sensors unlimited, INC) . . . . .	81
3.5 Images of active region NOAA 8518 at different wavelengths observed on April 19, 1999. (a) NIR filtergram, (b) visible light filtergram, (c) magnetogram, and (d) sub-frames from (a), (b), and (c) depicting the region of interest. The magnetograms were scaled between $-400$ G and $+250$ G. . . . .	82
3.6 Diagram of the setup for the April, 1999 observing run at BBSO. . . . .	83
3.7 Panels (a), (c), and (e) show scatter plots for the visible contrast as a function of the NIR contrast, and (b), (d), and (f) show plots for the averaged quantities. . . . .	86
3.8 Panels (a), (c), and (e) show plots for the NIR contrast as a function of magnetic flux density, and (b), (d), and (f) show plots for the visible contrast as a function of magnetic flux density. . . . .	88
3.9 Design of the Birefringent Lyot Filter. See Wang et al. (2001) for details. . . . .	91
3.10 This plot illustrates the transmission profile of each modular and the combination of them. (Cao et al. 2005b) . . . . .	92
3.11 Snapshot of active region NOAA 10707 on 2004 December 1. (a) NIR filtergram at 17:50 UT and (b) Visible light filtergram at 17:49 UT. The two images have the same FOV. Sub-areas marked by white boxes are dark pores selected visually. (c) The lowest contrasts of these small areas in the NIR are plotted as a function of those in visible. The straight line shows the linear fit of this plot. (d) Contrasts versus the absolute value of the corresponding magnetic flux density. . . . .	94

**LIST OF FIGURES**  
**(Continued)**

<b>Figure</b>	<b>Page</b>
3.12 Snapshot of active region NOAA 10707 on 2004 December 2. (a) NIR filtergram at 16:14 UT and (b) Visible light filtergram at 16:14 UT. The two images have the same FOV. Sub-areas marked by white boxes are dark pores selected visually. (c) The lowest contrasts of these small areas in the NIR are plotted as a function of those in visible. The straight line shows the linear fit of this plot. (d) Contrasts versus the absolute value of the corresponding magnetic flux density. . . . .	95
3.13 Snapshot of active region NOAA 10486 on 2003 October 29. (a) NIR filtergram at 20:58 UT and (b) Visible light filtergram at 20:58 UT. The two images have the same FOV. Sub-areas marked by white boxes are dark pores selected visually. (c) The lowest contrasts of these small areas in the NIR are plotted as a function of those in visible. The straight line shows the linear fit of this plot. (d) Contrasts versus the absolute value of the corresponding magnetic flux density. . . . .	96
3.14 Two NIR images taken on 2004 December 2 at 16:14 UT and 18:14 UT. Sub areas marked (a), (b), and (c) show the evolution of small pores. This evolution can be misinterpreted as “dark faculae”. . . . .	99

# CHAPTER 1

## INTRODUCTION

### 1.1 The Sun

#### 1.1.1 Overview

The Sun is one of the  $10^{20}$  main-sequence stars observed in the universe. It has an average mass of  $10^{33}$  g, an average temperature of 6000 K, an average volume of  $1.4 \times 10^{33}$  cm<sup>3</sup> and a typical spectral type of G2V. On the other hand, the Sun is very special to us. It is the nearest star to the Earth. Almost all the energy we need comes from the Sun. The total radiative energy received by the Earth is known as the solar constant, 'S' =  $1.367 \pm 0.002$  W m<sup>-2</sup> (Cox 2000). It is also the only star that can be observed by two dimensional photography with short exposure covering all the electromagnetic range, from  $\gamma$ -ray to the radio band.

With the improvement of telescopes and other instruments, more solar structures and active phenomena were observed. Such as umbrae and penumbrae, granulations, pores, faculae, plages, flares and coronal mass ejections (CMEs). However, the physics behind these observational phenomena was not well understood. Solar research is not only important because of interests in studying the Sun itself. A more important goal is to understand the mechanisms of solar activities and predict them before their occurrences, because these activity, such as solar flares and CMEs, can strongly affect the Earth and human life. For instance, they can disturb the structure of the Earth's thermosphere, heat the stratosphere, endanger space crafts and power systems, affect microwave communication and cause magnetic storms. All these effects are summarized descriptively as space weather problems.

The Earth consists of several layers, which from the innermost to the outermost are the core, the mantle, the crust and the atmosphere and which again can be divided into the troposphere, the stratosphere, the mesosphere, the thermosphere and the exosphere. Quite similar to the Earth, the Sun also has many different layers as shown in Figure 1.1.

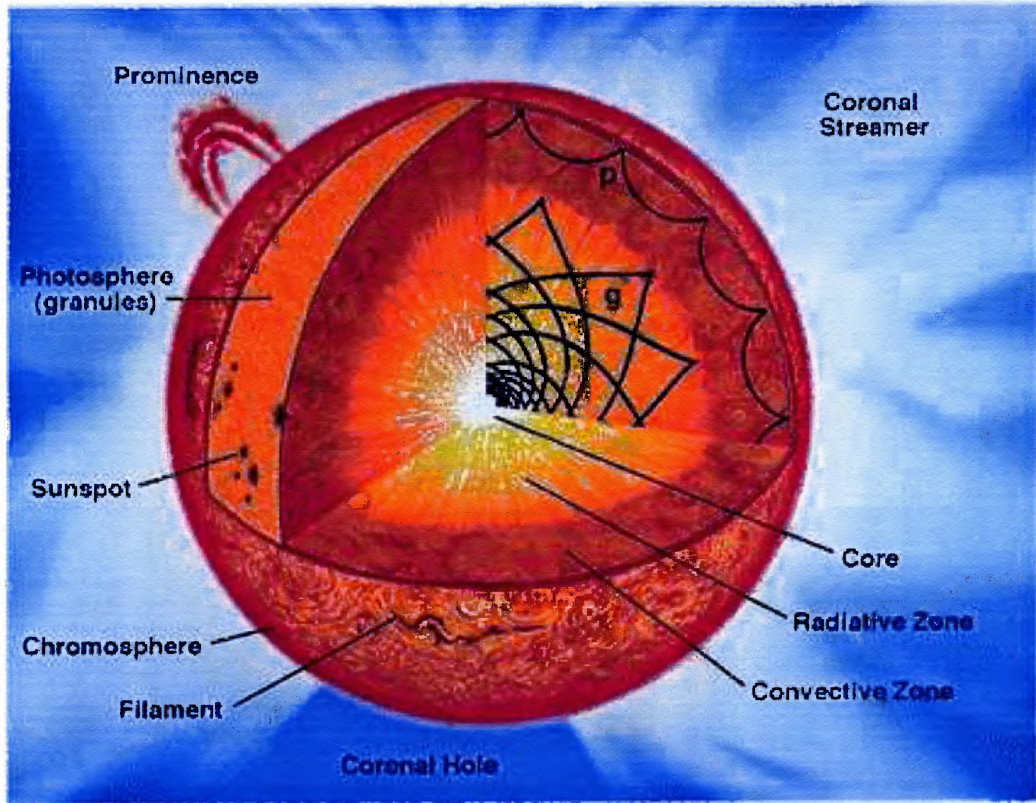


**Figure 1.1** Views of the Sun (<http://sohowww.nascom.nasa.gov/>, 2005 August 10.), Courtesy: SoHO/MDI

A standard solar model can be established by solving the following equations (Stix 2002)

$$\frac{\partial T}{\partial m} = \begin{cases} -\frac{3\kappa L}{256\pi^2\sigma r^4 T^3} & \text{(in a stable layer),} \\ \left(\frac{\partial T}{\partial m}\right)_c & \text{(in an unstable layer),} \end{cases} \quad (1.1)$$

$$\frac{\partial r}{\partial m} = \frac{1}{4\pi\rho r^2}, \quad (1.2)$$

$$\frac{\partial P}{\partial m} = -\frac{Gm}{4\pi r^4}, \quad (1.3)$$

$$\frac{\partial L}{\partial m} = \varepsilon - T \frac{\partial S}{\partial t}. \quad (1.4)$$

and

$$\rho = \rho(P, T), \quad (1.5)$$

$$dS = dS(P, T), \quad (1.6)$$

$$\varepsilon = \varepsilon(\rho, T), \quad (1.7)$$

$$\kappa = \kappa(\rho, T). \quad (1.8)$$

with certain boundary conditions at the center

$$r(0) = 0, m = 0, L(0) = 0, \quad (1.9)$$

and at the outer boundary

$$r = r_{\odot}, L(r_{\odot}) = L_{\odot}, P = 0, T = 0. \quad (1.10)$$

Where  $T$ ,  $m$ ,  $L$ ,  $P$ ,  $\rho$  are the temperature, mass, luminosity, pressure, and density interior to a sphere of radius  $r$ ,  $\varepsilon(\rho, T)$  is the nuclear energy sources,  $S$  the specific entropy (entropy per unit mass),  $\kappa$  the opacity, and  $\sigma$  the Stefan-Boltzmann constant. The result shows that a core with high temperature ( $1.5 \times 10^7$  K), high density ( $1.5 \times 10^2$  g cm<sup>-3</sup>) and high luminosity must exist, where thermonuclear fusion proceeds and therefore provides all of the Sun's energy. The thickness of the solar core is about 1/4 of the solar radius. Once energy is produced, it is released outward via radiation, consequently, the region surrounding the core of the Sun is named the radiation zone. The temperature is cooler in this area than the temperature inside. At about  $0.71 R_{\odot}$ , the opacity  $\kappa$  will increase very rapidly and the temperature gradient increases too. When the Schwarzschild criterion is satisfied, convection supersedes radiation as the major mechanism of energy transportation. This region is known as the convection zone. Next to the convection zone is the photosphere. It is the thinnest, but most important region. It is also understood as the bottom of the solar

atmosphere. In this stratum, the main free-path of photons increases very quickly and becomes comparable with the scale height  $H$ , i.e., the solar plasma changes from completely opaque to transparent. The photosphere is the visible surface of the Sun and most of the solar radiation that we receive comes from this layer. The temperature continues to decrease until the plasma reaches the top of the photosphere, which is also called the temperature minimum region (TMR). Above this is a 2000 km thick layer defined as the chromosphere. Within the chromosphere, after a layer with slowly increasing temperature, the temperature rises drastically from about  $2 \times 10^4$  K to a few million Kelvin in a region with a thickness of about 100 km, named the transition region. The temperature rise in this region is still an open question since this region is far away from the energy source, the solar core. The outermost region is known the corona. It does not have a clear outer boundary like the other layers. The corona stretches far out into interplanetary space, even to or beyond the Earth's orbit. Although all the layers, from chromosphere to corona, emit visible light, the coronal radiation is too weak to be seen directly except during a total solar eclipse or by an artificial eclipse, i.e., an occulting disk covering the bright solar disk.

### 1.1.2 Observing the Sun

In general, solar information can be collected by observations of electromagnetic radiation, particle flux (solar wind and high energy particles), and neutrinos. Among them, electromagnetic radiation, including  $\gamma$ -ray, X-ray (hard X-ray and soft X-ray), ultraviolet, visible, infrared and radio emission, is the most important. Figure 1.2 shows the atmospheric windows which are not affected by the absorption of the Earth's atmosphere. It is clear that ground-based observations are limited to the spectral range of visible, radio and a few infrared regions.

In order to observe in other wavelength regions, telescopes and detectors need to be put at very high altitudes. For instance, they can be carried by space-crafts such as the Ramaty High Energy Solar Spectroscopic Imager (RHESSI) (Lin et al. 2002), the Solar and

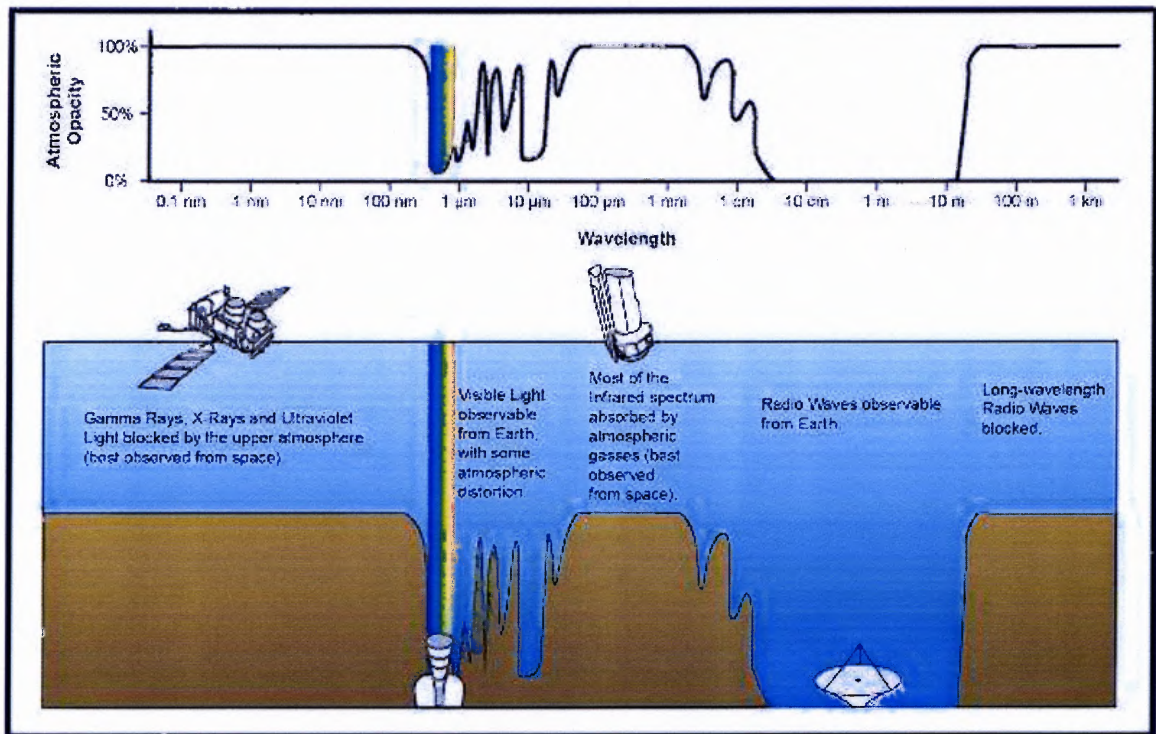


**Figure 1.2** Absorption effect in the Earth's atmosphere. (<http://www.ipac.caltech.edu>, 2005 August 1.)

Heliospheric Observatory (SoHO) (Scherrer et al. 1995), Transition Region and Coronal Explorer (TRACE) (Handy et al. 1999), by rocket missions, by air balloons and by airplanes. In the following sections, a few topics in solar physics are reviewed that are related to this dissertation.

## 1.2 Solar Flares

### 1.2.1 Overview

Solar flares are the most energetic events on the Sun (Wang & Tang 1993). They are defined as sudden, tremendous enhancements of solar brightness. The first flare observation was carried out independently by R. C. Carrington and R. Hodgson on 1859 September 1 (Tandberg-Hanssen & Emslie 1988). They found a significant contrast enhancement in the optical continuum against the strong photospheric background, which lasted for a few

minutes. We now know that it was a so-called “White-Light Flare”. Before the launch of space-telescopes, flare observations were limited to a few optical spectral lines, especially 6563 Å, with the famous name of the H $\alpha$  line. One of the reasons is that H $\alpha$  is very strong among all the Fraunhofer lines. During a flare, it becomes an emission line. Therefore, even for a weak event, the flare emission in H $\alpha$  is very prominent compared to its background and is therefore easy to detect.

When a large flare occurs, the total energy released is as much as  $10^{25}$  to  $10^{26}$  J (Lin & Hudson 1976). At the time as the H $\alpha$  enhancement, the flare energy release can be detected anywhere in the entire electromagnetic spectrum, as well as in energetic particles (protons and electrons) and mass flows. Solar flares are not isolated events. Contrarily, they are very complicated and always associated with other activities, such as filament eruptions and CMEs. Figure 1.3 (Golub & Pasachoff 1997) shows a typical time profile for a solar flare. Basically, there are three stages of energy release. The first one is the precursor, in which the magnetic energy is built up and triggered. Soft X-ray and H $\alpha$  emissions start to appear. After the precursor follows the impulsive phase. This is the major part of the flare. The  $\gamma$ -ray, hard X-ray (HXR), radio waves and visible light are emitted impulsively. The last step is the decay stage. The gradual decay of soft X-rays is the primary signature of the decay stage. The relationship between different emissions as a function of time will be discussed in detail in Chapter 2. Before that, one important aspect should be addressed, which is called the “Neupert Effect”. It has been found that the rise phase of the soft X-ray emission closely resembles the time integrated hard X-ray emission (Neupert 1968). The Neupert Effect has been proven by statistical studies and explained well by numerical models (Dennis & Zarro 1993; Veronig et al. 2002). This has led to the suggestion of a causal relationship between the non-thermal and thermal emission. However, a quantitative description of the Neupert effect is still unavailable (Golub & Pasachoff 1997).

In general, flares can be classified by the area of the flare brightening (the importance classification) or by the soft X-ray flux (X-ray classification) observed, for exam-

ple by the Geostationary Operational Environmental Satellite (GOES) within the bandpass of 1–8 Å. Table 1.1 and Table 1.2 list the importance classification according to the certain limitations (Tandberg-Hanssen & Emslie 1988) and the soft X-ray flare classification (Golub & Pasachoff 1997). Figure 1.4 gives an example of a series of solar flares observed by GOES soft X-ray detector.

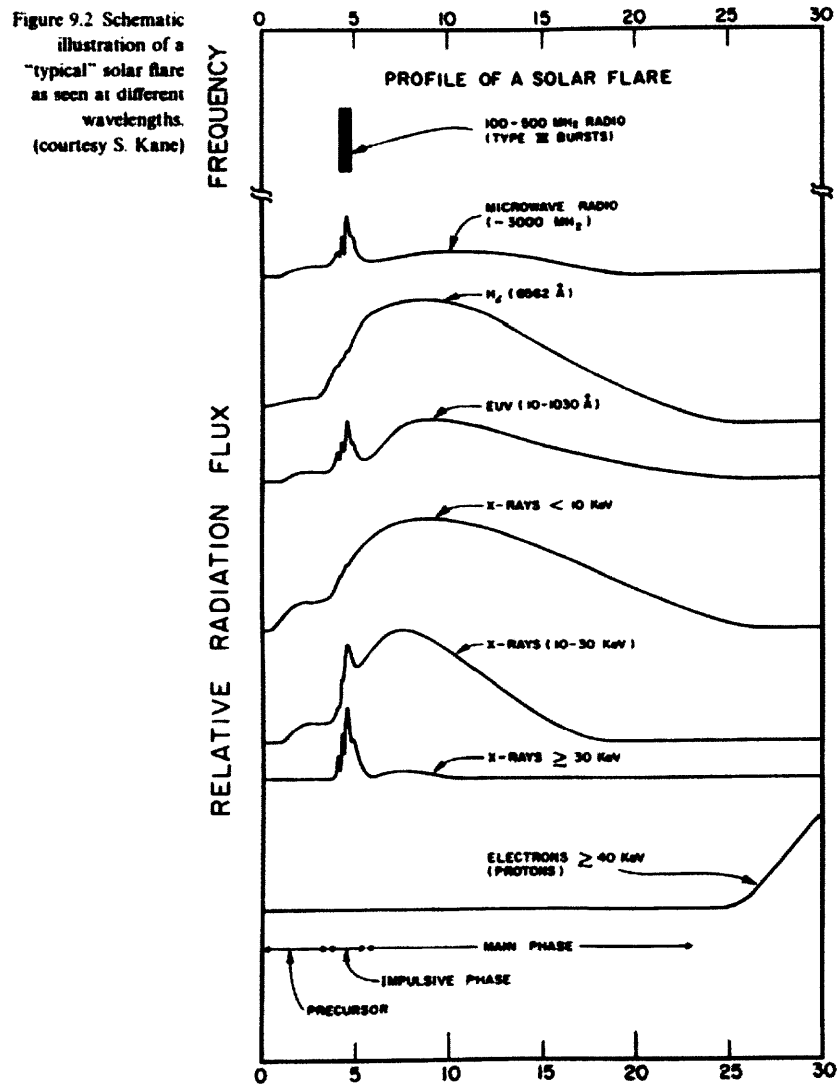
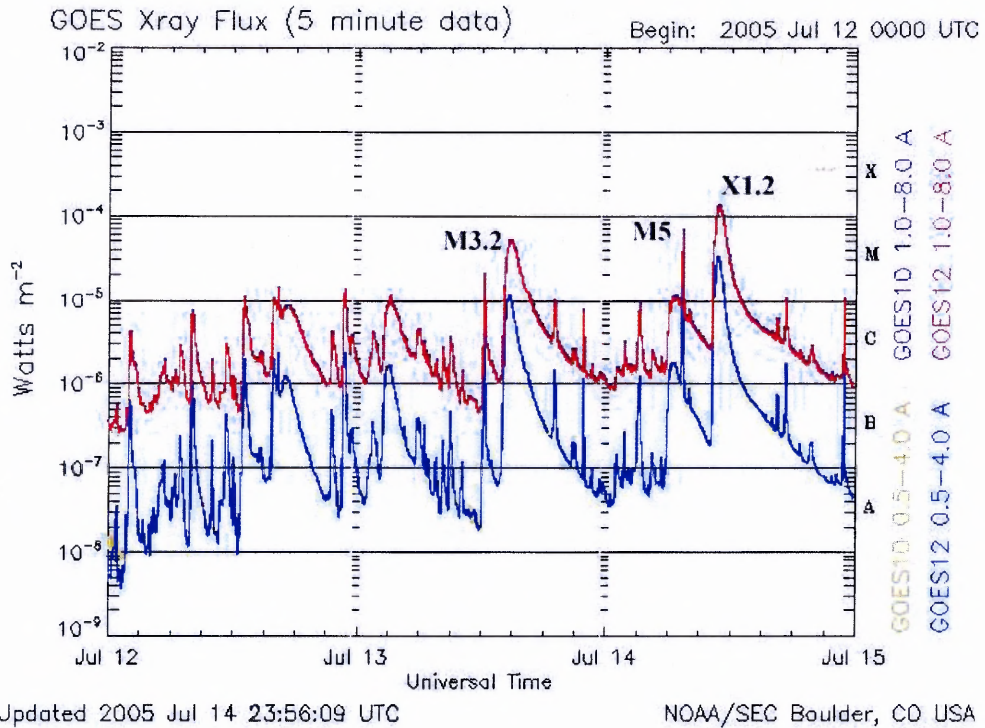


Figure 1.3 Light curves in different wavelengths during a "typical flare". x-axis denotes the time (minute). Adapted from (Golub & Pasachoff 1997)



**Figure 1.4** This figure shows several solar flares detected by NOAA satellite (GOES) in July 2005 including an X1.2, an M5, an M3.2 and few C-class flares.

**Table 1.1** The Visible Importance Classification

Corrected area		Relative intensity evaluation		
Square degrees	Millionths of hemisphere	Faint (f)	Normal (n)	Brilliant (b)
<2.06	<100	Sf	Sn	Sb
2.06-5.15	100-250	1f	1n	1b
5.15-12.4	250-600	2f	2n	2b
12.4-24.7	600-1200	3f	3n	3b
>24.7	>1200	4f	4n	4b

**Table 1.2** The Soft X-ray Flare Classification

Class	I ( $W m^{-2}$ )
B	$10^{-7}$
C	$10^{-6}$
M	$10^{-5}$
X	$10^{-4}$

### 1.2.2 Magnetic Fields and Solar Flares

Magnetic fields are present almost everywhere in the solar atmosphere. Their distribution is very complicated and can be divided into three types:

1. Active region magnetic fields, centered with sunspots, are the strongest fields. In the center of a sunspot, the field strength will be as high as a few thousand gauss. Most magnetic fields in active regions are bi-polar configurations. The field strength decreases as the height increases from photosphere to corona.
2. Similar to the Earth's dipole magnetic fields, solar magnetic fields can also be detected in the polar regions. However, the origin of this fields is not the same as on Earth. In the Sun, they only concentrate around the polar regions and are not symmetric. In addition, the electrical conductivity  $\sigma$  of the solar atmosphere is very high, resulting in a time scale of about 11 years for the evolution of polar magnetic fields (Leighton 1964; Devore & Sheeley 1987; Sheeley et al. 1987). This means that the field lines are constrained around the solar surface rather than originate from the inside.
3. Besides the magnetic fields in active regions and polar areas, other fields are encountered as network magnetic fields and intranetwork magnetic fields. Intranetwork magnetic fields are spatially the smallest magnetic features and only have 5 to 25 G measured flux densities (Livingston 1975; Wang et al. 1995). Only the flux density can be measured instead of field strength because the filling factors are unknown. Network magnetic fields are larger and stronger. Their strengths range from 20 to 200 G and can last more than a day (Keller et al. 1994).

Most of the solar dynamical phenomena are closely related to the presence and evolution of magnetic fields (Wang 2001). Particularly, solar flares are thought to be powered by the stored magnetic energy. Observations have shown that flares mainly occur in large

sunspot areas with highly complex magnetic configurations. Based on magnetic classification of sunspot groups by Künzel (1960),  $\delta$  spots produce more flares than others. The flare released free energy can be expressed as

$$\Delta E = E - E_0, \quad (1.11)$$

$$E = \frac{1}{8\pi} \int \int \int B^2 dv, \quad (1.12)$$

$$E_0 = \frac{1}{8\pi} \int \int \int B_p^2 dv. \quad (1.13)$$

where  $B$  is the actual magnetic field of the flaring area,  $B_p^2$  is the potential field, and  $v$  is the flaring area. Apparently, the nonpotentiality of magnetic field is proportion to the amount of energy released during a solar flare.

Magnetic shear is defined in terms of the angular difference between the azimuth of the potential transverse field and the observed field (Hagyard et al. 1984). It is closely related to the nonpotentiality. There are several ways to form a large magnetic shear (Wang 1997): (1) relative shear motion. (2) collision of opposite polarities. (3) new flux emergence. Harvey & Harvey (1976) first reported strong horizontal shear motions in chromospheric flare regions. More recently, Yang et al. (2004) found specific evidence of strong shear flows along the magnetic neutral lines, which are closely related to a X10 flare (see Figure 1.5). Deng et al. (2005b) extended Yang's work using a more comprehensive data set including white-light, near-infrared (NIR) and G-band observations covering the same event. The results show that the shear flows in the deep photosphere are much stronger than the flows in higher atmospheric layers, i.e., the shear flows most likely originate the photosphere or below.

Once free energy is built up, it can be triggered to release and then power the activity seen in the solar corona such as flares and CMEs (Metcalf et al. 2005). This release stage is believed to originate from magnetic reconnection, in which a large amount of magnetic free energy is released and a closed loop is formed (Ding 2003a). The most popular picture

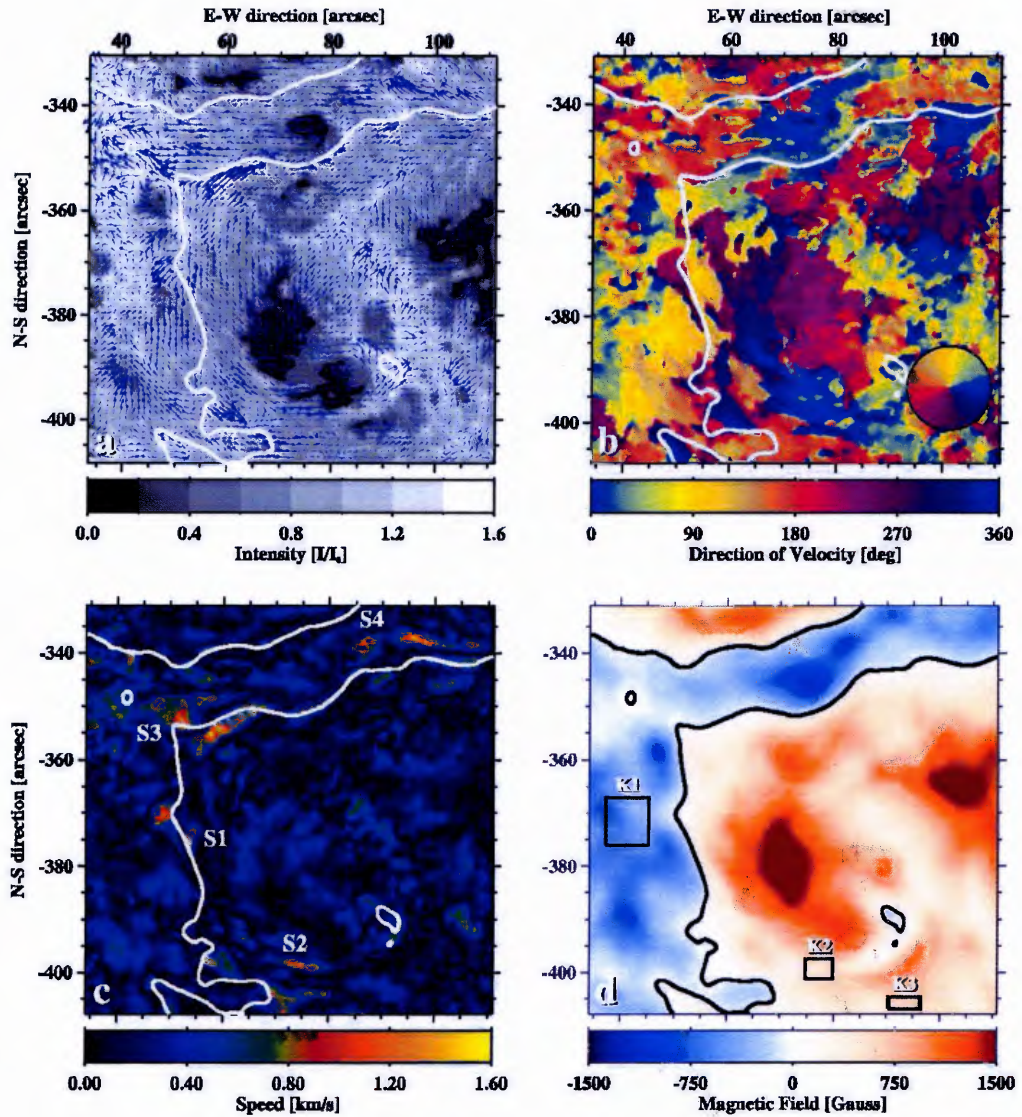


**Figure 1.5** Photospheric flows and magnetic field configuration of active region NOAA 10486 observed on 2003 October 29. To illustrate the high spatial resolution local correlation tracking results, we provide different views of (a) flow vectors, (b) azimuth angle of the velocity vectors, (c) magnitude of the velocity vectors, and (d) MDI magnetogram with superposed magnetic neutral lines. See Yang et al. (2004)

of the dynamics of solar flares is the two-ribbon configuration (Qiu et al. 2002). The two-ribbon configuration is characterized by a pair of long bright ribbons residing in opposite magnetic polarities along the neutral line and moving away from each other. According to the flare models, the ribbon expansion in  $H\alpha$  is the chromospheric signature of the progressive magnetic reconnection in the corona. The ribbon separation speed is related to the magnetic reconnection rate. Since the reconnection can not be observed directly, tracking the ribbon motion becomes important for understanding the energy release process.

A statistical study has shown that 95% of filament eruptions in active regions are associated with flares (Jing et al. 2004). Consequently, filament eruptions are believed to be an important trigger mechanism of magnetic reconnection. A detailed description can be found in the study by Hirayama (1974). The cartoon in Figure 1.6 (Lin et al. 2004) shows the basic idea of how eruptions drive magnetic reconnection and flares.

Rapid penumbral decay and umbral enhancement are other significant photospheric magnetic changes associated with solar flare. The rapid change is thought to reflect the variation of magnetic topology before and after a flare, and then to provide crucial information as to how the stored magnetic energy is released (Liu et al. 2005). High resolution and high cadence space observations have shown the existence of rapid magnetic evolution closely related to strong solar flares (Kosovichev & Zharkova 2001; Spirock et al. 2002; Wang et al. 2002a,b, 2004; Yurchyskyn et al. 2004; Deng et al. 2005b). A more comprehensive study by Liu et al. (2005) presented white-light observations by TRACE. Their sampling includes six X-class flares and one M-class flare. In all of the seven events, part of the penumbral area located around the sunspot decayed rapidly after the flare and simultaneously the center part of the umbra was enhanced. By comparing with vector magnetograms, the decay of the penumbra was characterized as the result of increasing vertical magnetic component and the darkening of the the umbra was due to the enhancement of both vertical and transverse components. Figure 1.7 shows the schematic diagram of the so-called “quadrupolar reconnection” model discussed above, which is one of the models trying to explain the per-

manent magnetic changes associated with solar flares.

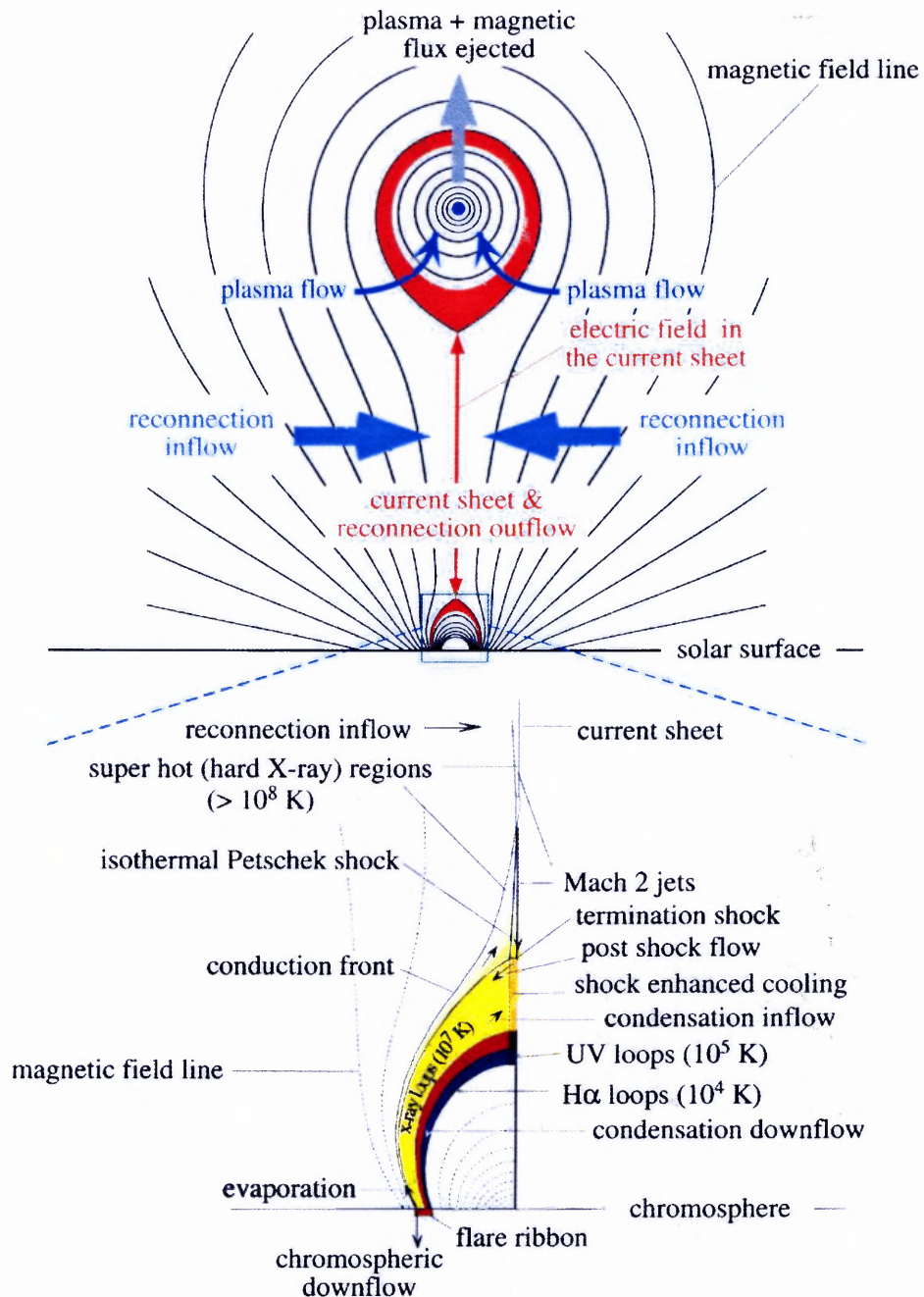
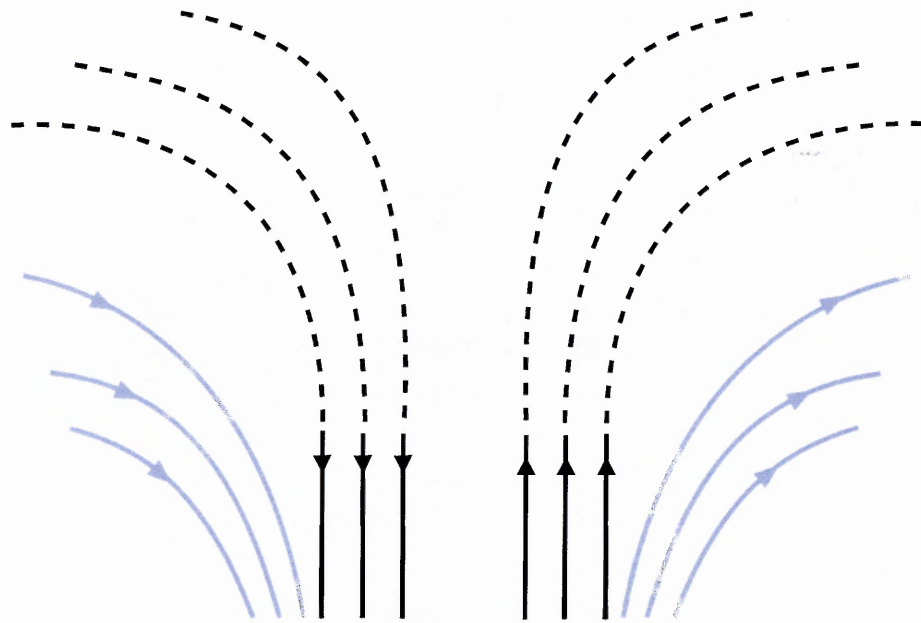
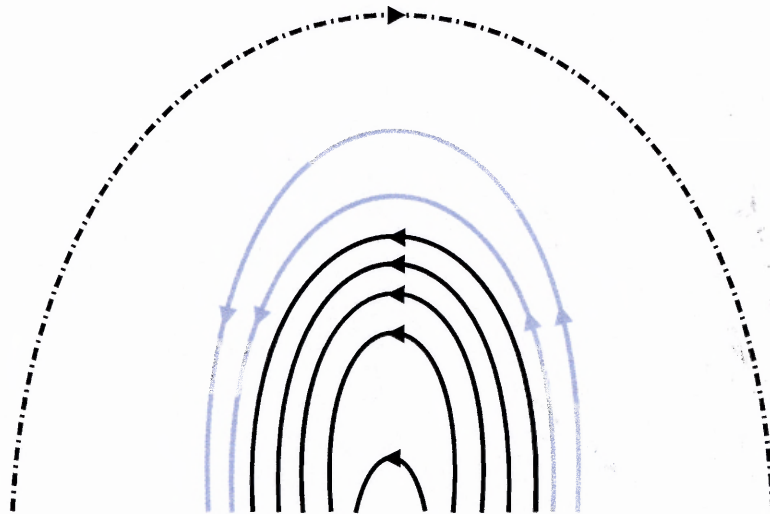


**Figure 1.6** Schematic diagram of a disrupted magnetic field that forms in an eruptive process. Colors are used to roughly denote the plasma layers in different temperatures. This diagram incorporates the two-ribbon flare configuration of Forbes & Acton (1996) and the CME configuration of Lin & Forbes (2000).



(a) before flare



(b) after flare

**Figure 1.7** Schematic reconnection to explain rapid magnetic field changes associated with solar flares. (a) Initial magnetic field configuration before the flare. Penumbral fields are in gray and umbral areas are in black. (b) Magnetic field configuration after the flare. Dashed-dotted line represents the connection of a dipolar area far away from the neutral line (Liu et al. 2005).

### 1.2.3 Particle Acceleration

Magnetic reconnection releases energy in the corona. A large amount of energy is transported and deposited in the lower atmosphere, such as the chromosphere and the photosphere through heat conduction, through radiation and by charged particles accelerated in the corona. These charged particles, basically protons and electrons, spiral downward along magnetic field lines and deposit their energy into the chromosphere, a much denser layer than the corona (Brown 1971). Now, the question is how the electrons and protons are accelerated. The magnetic field can change the direction of a charged particle. However, the energy of the charged particles will not be increased. Therefore, the energy required by the acceleration must come from either electric field or collision. According to the theoretic model of magnetohydrodynamics, an inductive electric field can be induced by moving plasma and then the charged particles can be accelerated by this electric field (Parker 1958; Sakurai 1974). The angle between the velocity vectors for the plasma and the particles is crucial to determining whether the acceleration will occur

$$\frac{d\varepsilon}{dt} = \frac{Ze}{c} u \cdot (v \times B) \quad (1.14)$$

where  $\varepsilon$  and  $v$  are respectively the kinetic energy and the speed of protons or electrons,  $t$  is the time,  $c$  is the speed of light,  $u$  is the plasma velocity, and  $B$  is the magnetic field strength. However, this mechanism may not be efficient and more study of the comparison with observations is needed. Another possibility is fast shock wave acceleration (Somov & Kosugi 1997; Thomas et al. 1990). However, the existence of fast shock waves was questioned by Miller et al. (1997); Forbes et al. (1989). More efficient ways to accelerate particles should be Super-Dreicer electric field (Holman 1985; Benka & Holman 1994) and Sub-Dreicer field (Litvinenko 1996; Litvinenko & Craig 2000). A Dreicer field is defined as

$$E_D = \frac{n_e e^3 \ln \Lambda}{2\pi \varepsilon_0^2 m_e v_T^2} \quad (1.15)$$

where  $n_e$  is the electron number density in the corona,  $\ln \Lambda = 12\pi n_e \left(\frac{\epsilon_0 T_e}{n_e e^2}\right)^{3/2}$ , is called the coulomb logarithm,  $\epsilon_0$  is the dielectric constant, and  $v_T$  is the thermal speed of coronal electrons. Within a Dreicer field, the energy loss due to the collision of an electron is equal to the energy received from the field. The electric fields induced from the magnetic reconnection are always larger than  $E_D$ . Therefore, some more recent models are paying attention to the Super-Dreicer fields. With a field strength of about  $10 \text{ V cm}^{-1}$ , the electrons and protons can be accelerated to very high energy quickly. Such high Dreicer fields have been observed by Qiu et al. (2002); Xu et al. (2004a, 2005a). In addition, a longitudinal magnetic field is required to keep the particles inside the electric field (Litvinenko & Somov 1993). After being accelerated, part of the particles will spiral along the magnetic field lines and produce radio bursts, HXR bursts and optical emission.

#### 1.2.4 Hard X-ray Emission

The processes which generate hard X-ray include bremsstrahlung, inverse Compton scattering and synchrotron radiation. In the case of a solar flare, the synchrotron radiation is not important because it requires very strong magnetic field of about  $10^4$  to  $10^5$  G in the corona and electrons with extreme energy of 1 to 10 GeV (Korchak 1971; Ramaty et al. 1975).

Theoretically, after Compton scattering, the energy of emergent photon is smaller than the energy of the incident photon. The emergent photon energy can be determined by

$$E_{\gamma'} = \frac{h\nu_0}{1 + (h\nu_0/m_0c^2)(1 - \cos \theta)}, \quad (1.16)$$

with a maximum value equal to the incident photon energy,  $h\nu_0$ . When the electron energy is much larger than the incident photon energy, the emergent photon energy will be larger than that of the incidence photons, i.e.,  $E_{\gamma'} \gg h\nu_0$ . This interaction is called inverse Compton scattering. Unfortunately, inverse Compton scattering is not an efficient

hard X-ray emission mechanism during solar flares. Its contribution is much smaller than bremsstrahlung unless an electron flux exists with a lower energy cut-off greater than 20 MeV (McClements & Brown 1986; Kaufmann et al. 1986).

Unlike the reactions discussed above, bremsstrahlung is an interaction between electrons and other charged particles. In the case of solar flares, the other charged particles are protons. As shown in Figure 1.8, an electron is accelerated during the swing-by around a proton or another ion. Consequently, electromagnetic radiation is emitted in the hard X-ray spectral range.

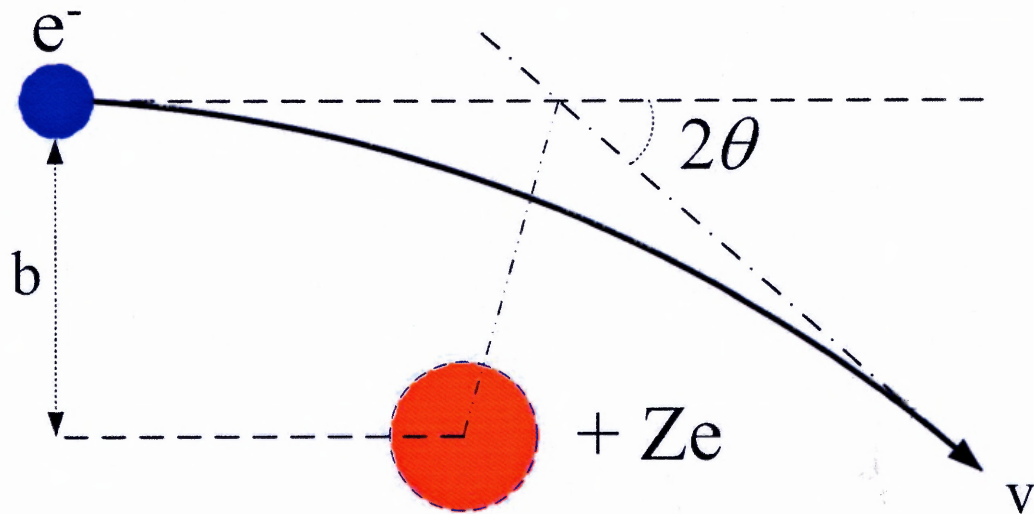


**Figure 1.8** Schematic diagram of an electron swing-by around a proton.

When the observations are carried out at the Earth's distance, the average bremsstrahlung photon count rate is given by Aschwanden (2002)

$$I(\varepsilon) = \frac{1}{4\pi R^2} n_p \int \chi(\varepsilon, E) v(E) N(E) dE, \quad (1.17)$$

where  $n_p$  is the number density of ambient protons,  $N(E)$  the number density of electrons,  $v(E)$  the velocity of an electron with kinetic energy  $E$ , and the cross-section differential  $\chi$

is defined as

$$\chi(\varepsilon, E) = \frac{8r_0^2 m_e c^2}{411\varepsilon E} \log \frac{1 + \sqrt{1 - \varepsilon/E}}{1 - \sqrt{1 + \varepsilon/E}} \quad (1.18)$$

where  $\varepsilon$  is the photon energy,  $m_e, r_0$  and  $E$  are the rest mass, radius, and kinetic energy of the electron, and  $c$  the speed of light. These equations can also be found in Jackson (1962). In the well accepted ‘‘thick target’’ model, the electrons lose most of their energy as a consequence of collisions in thick target regions, which are most likely located in the chromosphere. Hence, the spectrum of the injected electrons will change. Observations show that the spectrums of photons produced by bremsstrahlung are usually able to be expressed by a single power law function (Crosby et al. 1993, 1998; Bromund et al. 1995; Dennis 1985). Therefore, it is reasonable to assume that the incident electrons also have a power law distribution. Due to the energy loss, the power index of incident electrons is smaller than that of emergent photons (Brown 1971). A typical photon spectrum for a large flare also includes a thermal part in the lower energy range and a high-energy part which is known as  $\gamma$ -ray radiation. The thermal part is produced by electrons that satisfy the Maxwell distribution for velocity and energy

$$f(v) = 4\pi \left(\frac{m}{2\pi kT}\right)^{3/2} n_e v^2 \exp\left(\frac{-mv^2}{2kT}\right), \quad (1.19)$$

$$f_E(E) = f(v)dv/dE = \frac{2n_e}{\pi^{1/2}(kT)^{3/2}} E^{1/2} \exp(-E/kT). \quad (1.20)$$

where  $m, v$ , and  $n_e$  are the mass, velocity, the number density of electrons,  $k$  the Boltzmann constant. The  $\gamma$ -ray is basically thought to be generated by protons interacting with other charged particles.

### 1.3 Small-Scale Magnetic Features

Solar magnetic fields play an important role in solar physics (Zirin 1988). They are very complex and exist in all layers of the solar atmosphere from the photosphere to the corona.

The field strength varies from a few gauss to a few thousand gauss. The most important property of solar magnetic field is the “frozen effect” (Stix 2002), i.e., the magnetic flux is frozen in and transported along with the contiguous plasma. To understand this point, we need to start with the magnetohydrodynamical (MHD) induction equation (Zirin 1988)

$$\frac{\partial \mathbf{B}}{\partial t} = \nabla \times (\mathbf{v} \times \mathbf{B}) - \frac{1}{\mu\sigma} \nabla^2 \mathbf{B}. \quad (1.21)$$

This equation implies that the temporal variation of magnetic fields includes two parts, the effect from additional magnetic field induced by the induced electric field (the first term on the right-hand side, which can be simplified as  $\mathbf{v}B/l$ ) and the magnetic diffusion caused by the finite electric conductivity (the second term in the right-hand side of the above equation, which can be simplified as  $B/\mu\sigma l^2$ ). The ratio of these two terms is well known as the magnetic Reynolds number  $R_m$ , which is defined expressively as

$$R_m = \mu\sigma vl = \frac{\mu\sigma l^2}{l/v}, \quad (1.22)$$

where  $\mu$  is the magnetic permeability,  $\sigma$  is the electric conductivity,  $l$  is the scale of spatial field variation and  $v$  is the speed of material motion.  $R_m$  can also be understood as the ratio between the time scales of diffusion  $l/v$  and the condensation  $\mu\sigma l^2$ .  $R_m \ll 1$  represents the situation in which the magnetic diffusion is much faster than condensation, i.e., the magnetic flux is not concentrated together. However, due to the high electric conductivity  $\sigma$  and the large scale of features in the solar atmosphere,  $R_m$  is always  $\gg 1$ . In other words, the magnetic flux is frozen in the ambient plasma, and they move together.

### 1.3.1 Magnetic Flux Tubes

It is well known that solar magnetic fields are concentrated in flux tubes (Wang et al. 1998). They are observed in different scales as sunspots, pores and magnetic network flux ele-

ments. The existence of flux tubes has been proven theoretically by Kraichnan (1976); Peckover & Weiss (1978). As pointed out at the very beginning of this dissertation, the solar magnetic field originates most likely in the convection zone. In this layer, the thermal pressure is greater than the magnetic pressure inside the flux tubes. This acting together with the “frozen effect” causes the magnetic field lines to move along with the convecting materials.

Since magnetic pressure exists inside of the flux tubes, the thermal pressure inside must be smaller than outside in order to balance the pressure (Stix 2002)

$$P_{\text{inside}} = P_{\text{outside}} - \frac{B^2}{8\pi}. \quad (1.23)$$

In thermal equilibrium, the density of the flux tubes is lower than outside and the buoyancy force will cause the flux tubes to move upward and emerge into the photosphere. Due to the quick drop in densities and pressures in the photosphere, the flux tubes spread into the chromosphere and the corona. There they can be observed by the high resolution of the extreme ultraviolet (EUV) band and by coronal monochromatic images. The largest and easiest to observe magnetic flux tube features are sunspots. They are the essential component of a solar active region. Many different kinds of activity appear around sunspots, such as photospheric faculae, filigrees, and the chromospheric plages, filaments and the most exciting phenomena of solar flares. The typical structure of a sunspot is shown in Figure 1.9. A simple sunspot is shown on the top and a more complicated sunspot group is presented on the bottom. The dark center of a sunspot is called the “umbra”, which is associated with extreme strong magnetic field as high as a few thousand gauss. The less dark area surrounding the umbra is called the “penumbra” which is hotter than the umbral area and the field strength is weaker. A sunspot is not a single

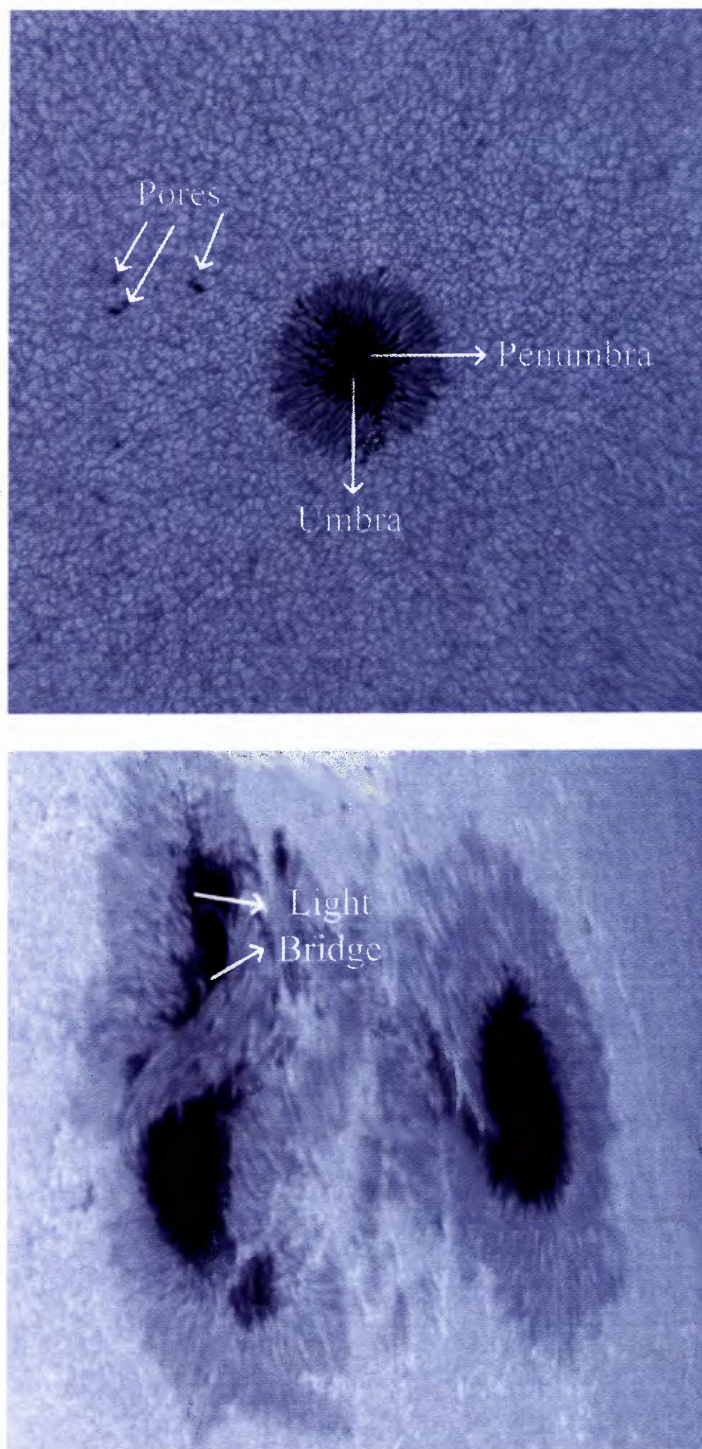


**Figure 1.9** Two sunspots are shown in this figure. They were observed at 18:52:48 UT (Top) and 18:44:54 UT (Bottom) on 2003 November 2. The lower one is much larger and more complex than the one at the top.

seismology to produce a three-dimensional map of a region extending some 10,000 miles below the sunspot (Zhao et al. 2001; Zhao & Kosovichev 2003, 2004a). Figure 1.10 and Figure 1.11 show the sunspot models and related phenomena. At this moment, their data from SoHO/MDI have a cadence of one minute, but their method requires eight hours for constructing one map, hence their study is limited to only larger scale magnetic structures that have longer lifetime.

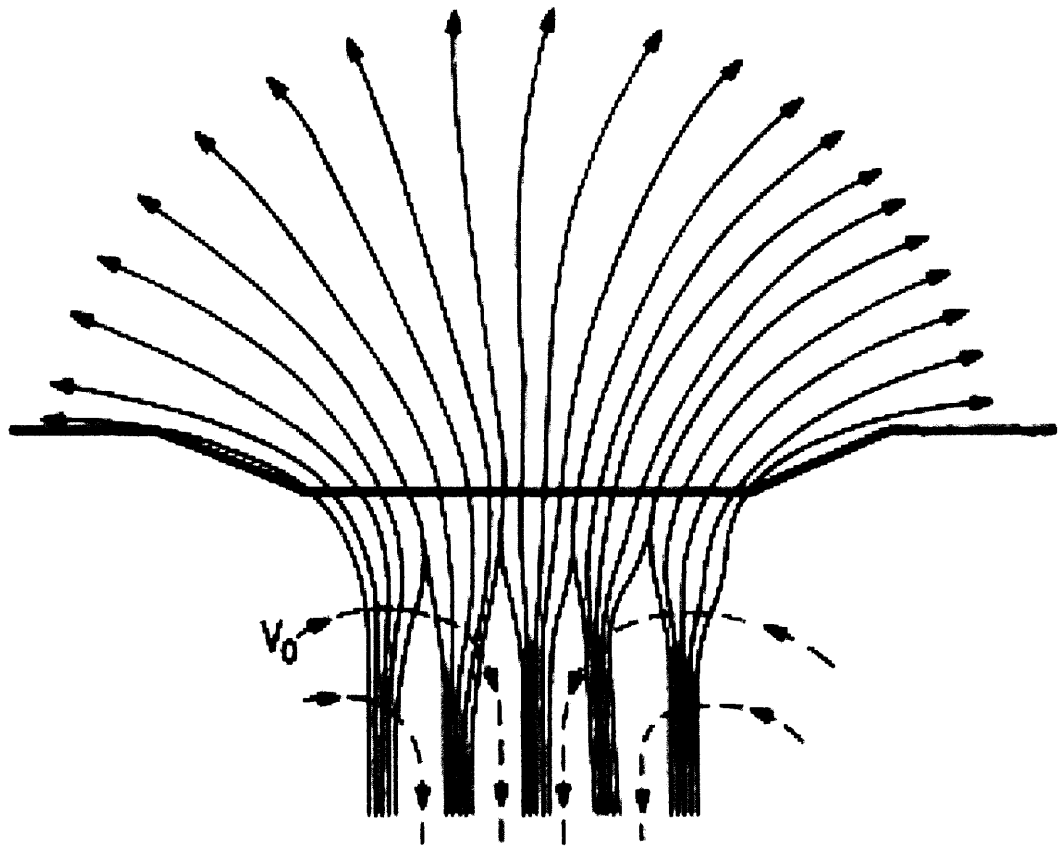


**Figure 1.10** The cluster model of a sunspot proposed by Parker (1979).

In addition, near the photosphere, all of the flux tubes are perpendicular to the solar surface (Spruit & van Ballegoijen 1982). Horizontal magnetic flux tubes may exist only for a very short period because they are not stable in such a configuration. Figure 1.12

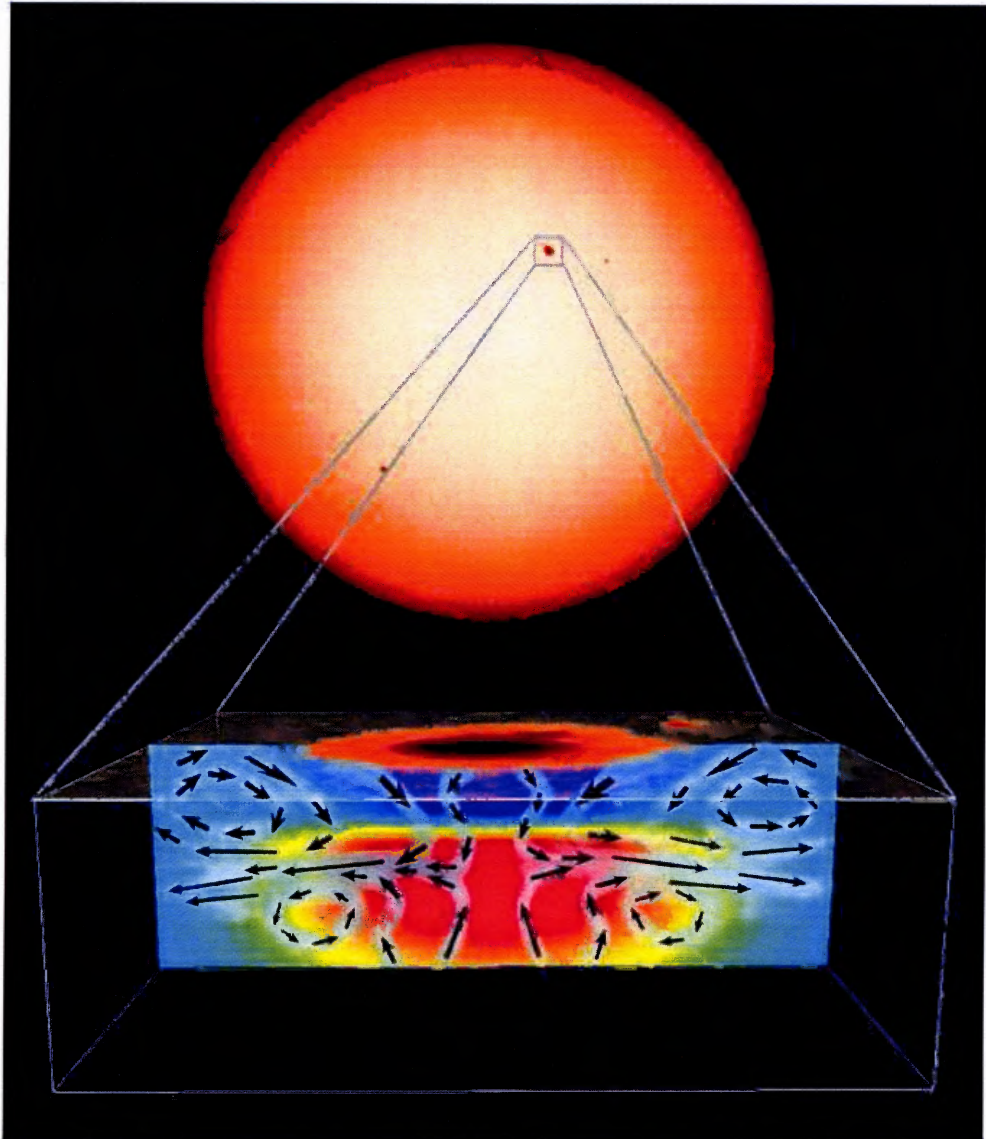


**Figure 1.11** A cartoon showing both the sound-speed variations and the subsurface flow patterns of a sunspot (Courtesy: SoHO/MDI). Adapted from Zhao (2004b)

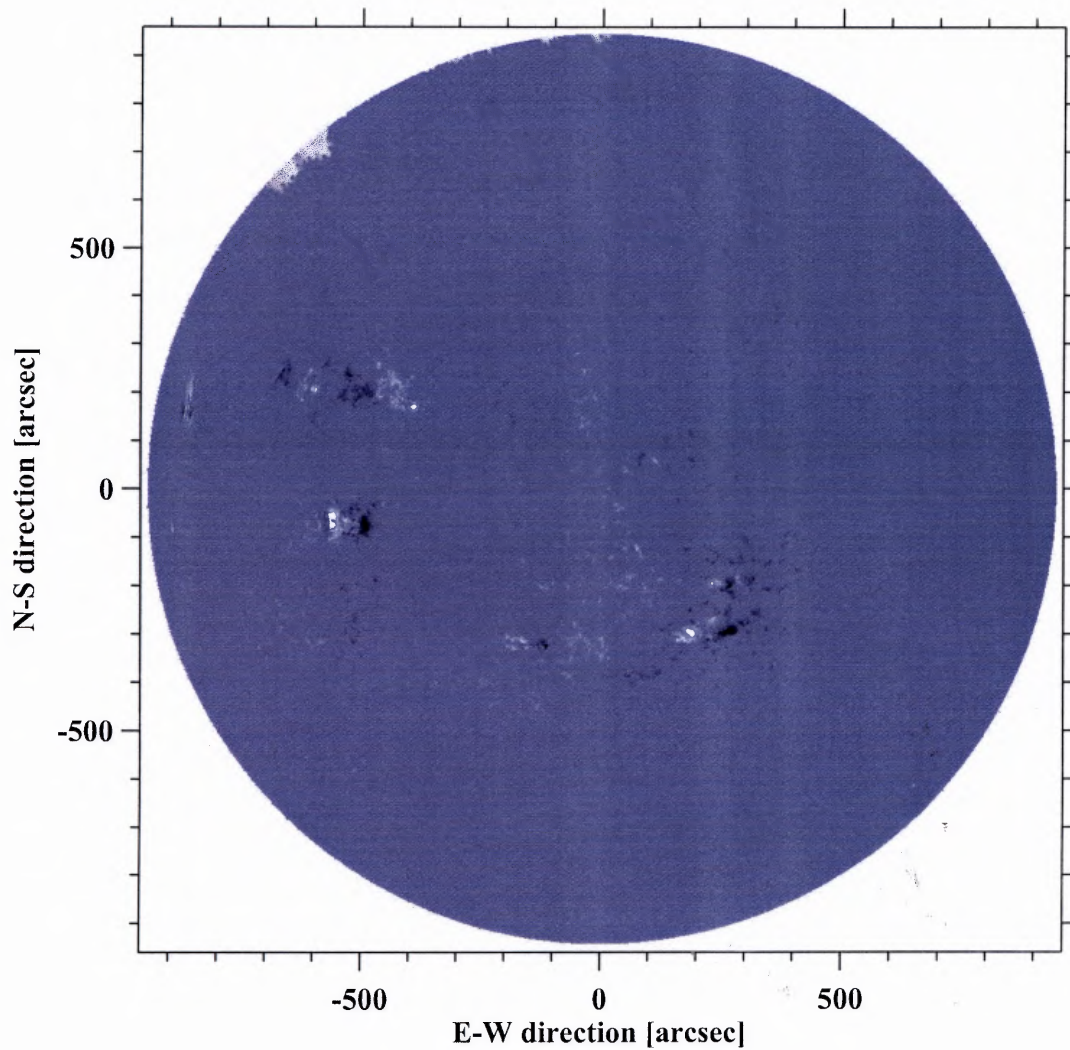


**Figure 1.12** This figure shows the full disk line-of-sight magnetogram from SoHO/MDI obtained at 17:00:02 UT on 2005 July 1.

shows a full-disk magnetogram from SoHO/MDI. Large concentrations of both polarities (black and white refer to negative and positive polarities, respectively) are found in the active regions. Figure 1.13 gives the basic idea of the magnetic concentration due to the convection and the vertical configuration of magnetic flux tubes. Since the density and pressure in the solar atmosphere are much weaker than in the convection zone, the flux tube spreads out significantly after emerging from the photosphere (see Figure 1.13).

Due to the limit of spatial resolution, it is difficult to measure the field strength in filtergrams. In this case, the magnetic flux density is used instead of field strength because the filling factor is unknown. Spectroscopy is able to solve this problem, but it loses temporal resolution, which is very important for the study of the small magnetic structures due to their fast evolution compared to larger features, such as sunspots. This is one reason why solar physicists are motivated to build a fast mode spectropolarimeter based on the filtergraph, such as the Infrared Imaging Magnetogram (IRIM) of BBSO (Denker et al. 2003; Cao et al. 2005a,b,c) or a spectrograph using fiber optic techniques (e.g., Fiber Optics Image Slicer (FOIS) project, by Dr. Lin in Mees Solar Observatory). In this dissertation, I use data from an existing filtergrams. Therefore, only magnetic flux density is measured and discussed.

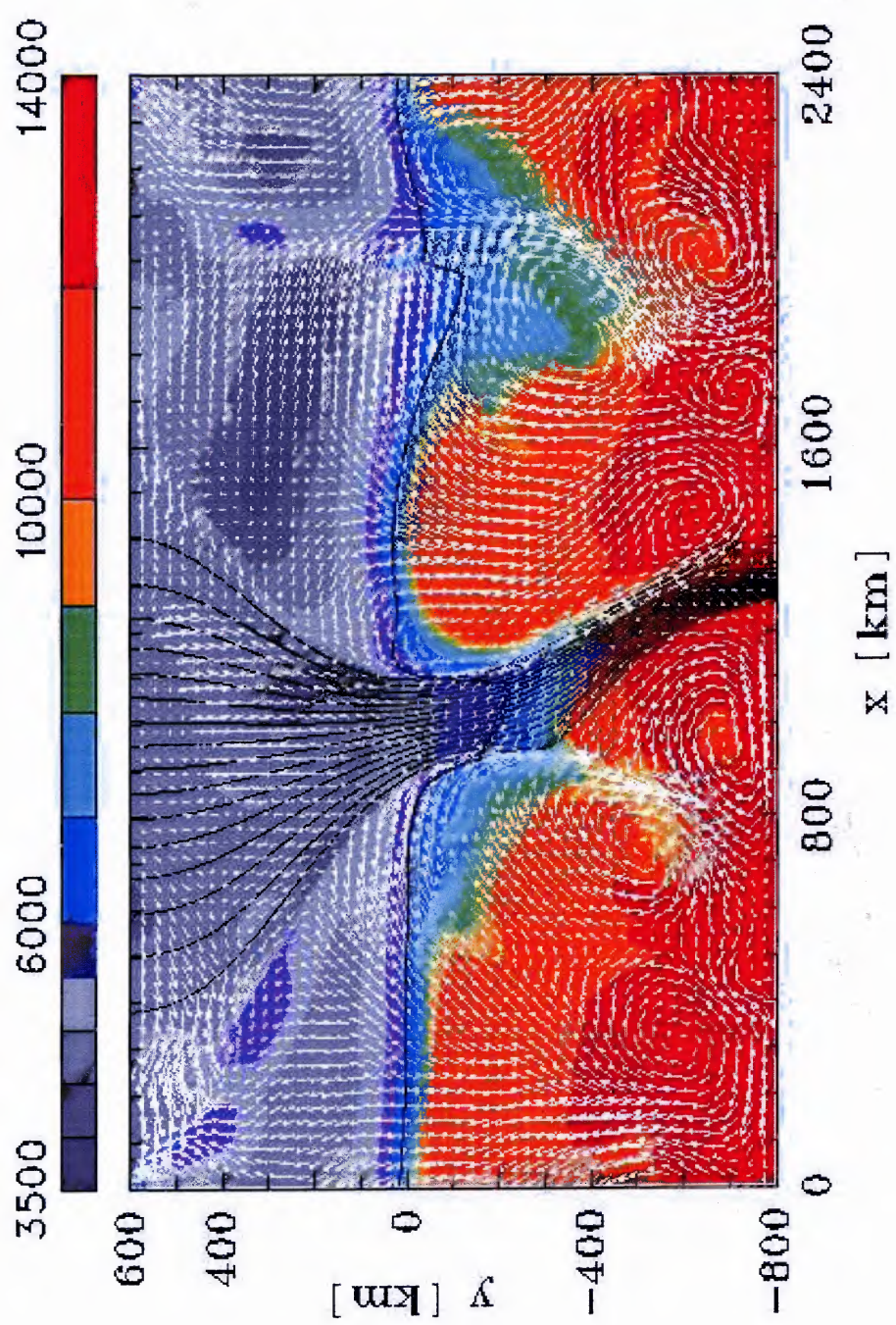


**Figure 1.13** Vertical cut of a magnetic flux tube. The thick curve at  $z = 0$  denotes the optical depth in the photosphere where  $\tau_{5000} = 1$ . See Steiner et al. (2001).

### 1.3.2 Bright Points

Pores are small magnetic flux tubes. They are the first stages of forming sunspots (Sobotka et al. 1999). Figure 1.14 shows this kind of evolution. When the flux tubes become even smaller, they no longer appear as dark features. Instead, they appear to be brighter than the quiet Sun background. For this reason, they are called “bright points”. More than 90% of the magnetic flux outside of sunspots is in small tubes (Frazier & Stenflo 1972). The diameter of one of these tiny elements is about a few hundred kilometers, which corresponds to less than 1'' on the solar disk (Berger & Title 2001). However, the associated magnetic fields are strong. There are numerous names for phenomena related to bright points, such as faculae, filigrees, G-band bright points, and plages. Originally, the bright points observed close to the disk center in the photosphere were called filigrees (Dunn & Zirker 1973; Muller & Roudier 1984). Later on, these bright points and others at all locations became known as faculae. Figure 1.15 shows the faculae or bright points in a close-up view. Bright points and white-light faculae can be found in the enlarged sub-field-of-view (FOV). The G-band images have the highest contrast ratio for observing the bright points. The enhanced contrast in the G-band is due to the fact that the radiation of CH molecules, which is much more sensitive to the temperature gradient than other optical wavelengths (Steiner et al. 2001). In order to avoid confusion, the term “faculae” is used to refer to all of the names of bright points including faculae, filigrees, and G-band brightenings in the rest parts of this dissertation.

The bright points reveal the essential details that help people to understand solar magnetic phenomena. The relationship between sunspots and faculae is an essential question (Chapman et al. 1997). Although faculae are very small spatially, their huge number makes them comparable with larger structures. It is now clear that in term of solar irradiance contribution changes in facular area, contrast, and distribution can compensate or even exceed the deficits caused by sunspots and pores over the 11 year solar cycle (Foukal & Lean 1988; Schatten 1988; Kuhn et al. 1988; Foukal et al. 2004). Solar cycle refers to

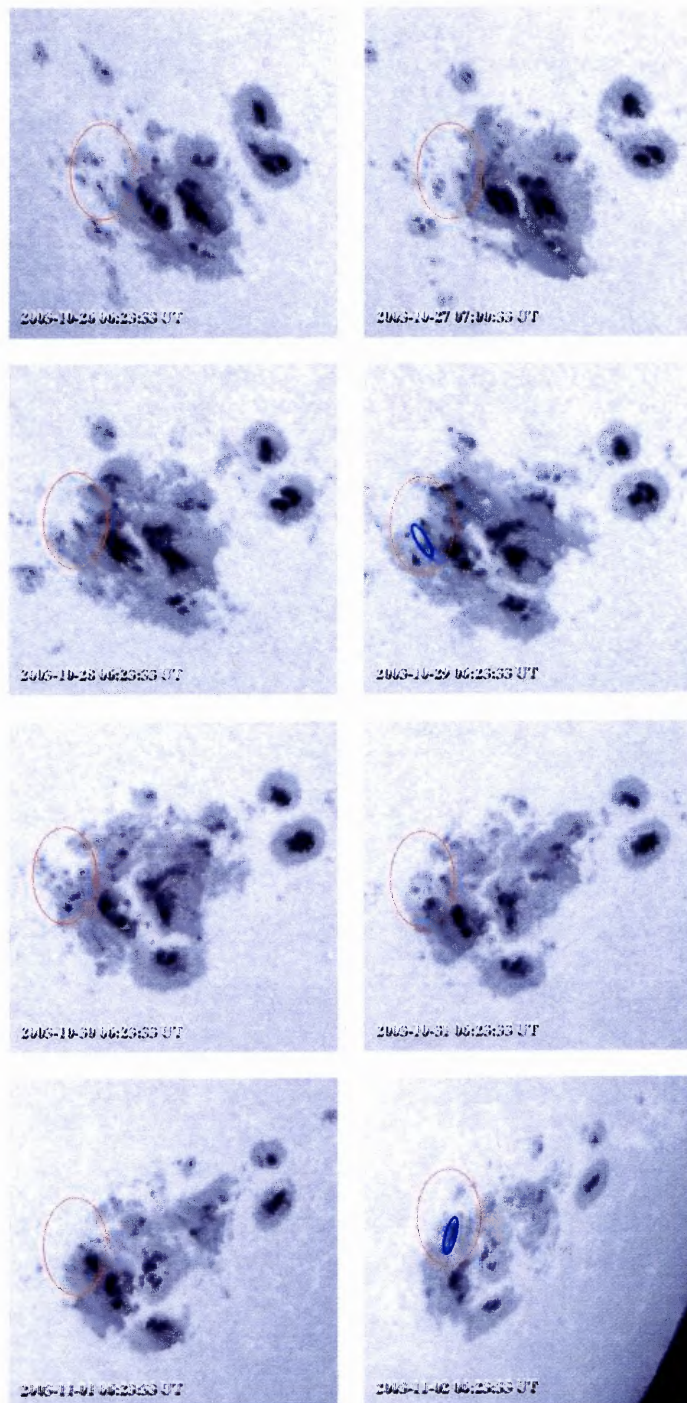


**Figure 1.14** This figure shows MDI magnetograms obtained from 2003 October 26 to 2003 November 2. The areas marked with red circles indicate the formation of a sunspot from several small spots. The two blue ellipses refer to the flare areas on 2003 October 29 and November 2.

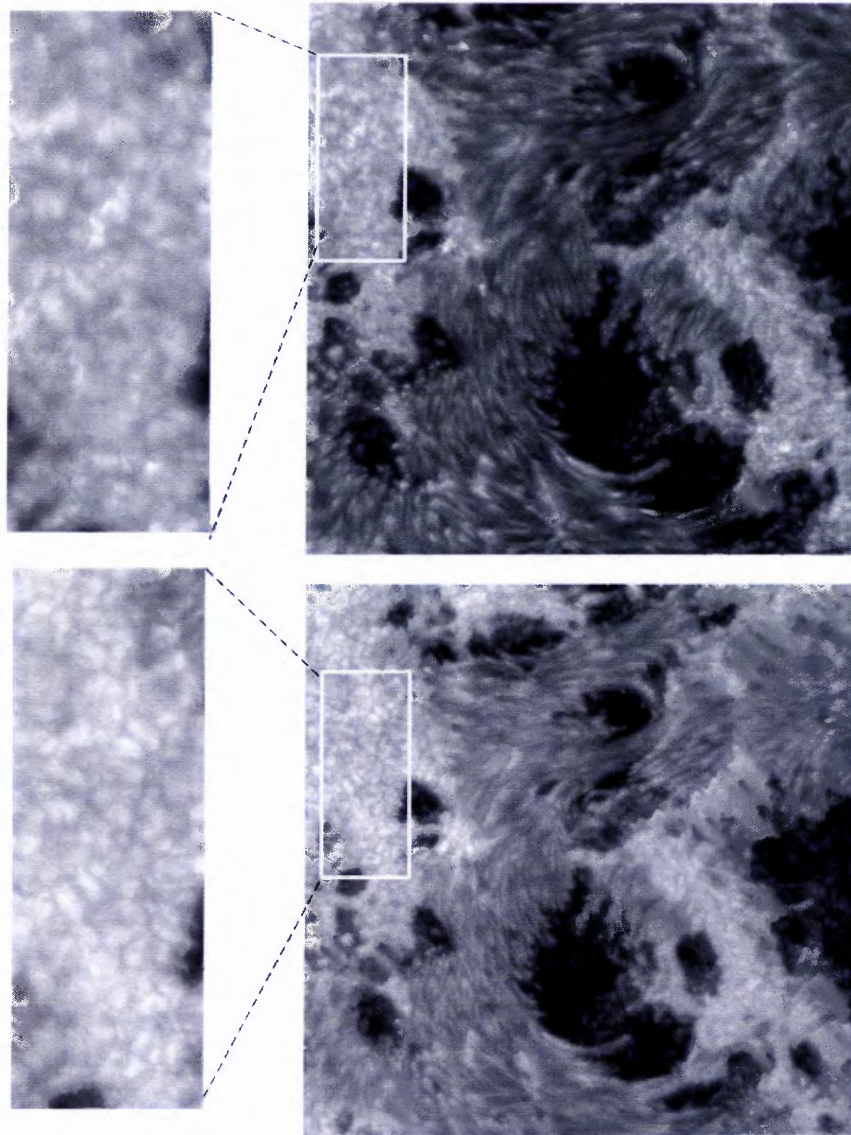


**Figure 1.15** Images of Active Region NOAA 10486 obtained at 20:33:28 UT in the G-band (Top) and 20:34:19 UT in the visible continuum (Bottom) on 2003 October 29. Two small images show the sub-areas marked with white boxes in the larger images, which contain bright facular points.

the periodic variation in the number of sunspots. Observational evidence shows that total solar irradiance and solar activities vary along with the change of sunspots. During the solar maximum, both the total solar irradiance and the level of solar activity reach a peak.

Furthermore, faculae are not only related to the photosphere. They are believed to be responsible for part of the coronal heating. From UV and X-ray coronal observations, the coronal structure is sensitive to the magnetic fields. Therefore, some type of a MHD process is regarded as the coronal heating mechanism. Faculae are the foot points of coronal magnetic field lines. The motion of faculae will cause heating of the upper atmosphere either by MHD waves (Hollweg 1984) including Alfvén waves and magnetoacoustic waves, or by topological dissipation and nano-flares (Parker 1972, 1983). Other mechanisms may also contribute to the heating.

Although the first study of faculae was done a few decades ago, faculae are usually too small to be fully resolved even with meter-class ground-based telescopes. Fortunately, the recently developed High-Order Adaptive Optics system (HOAO) and more sensitive detectors, enable images with better signal-to-noise ratio with the diffraction limit resolution to be obtained. More advanced studies can be carried out using the state-of-the-art data.

#### **1.4 Observations in the Near-Infrared Spectral Range**

Residing between the visible and radio wavelengths, the infrared covers a wide range from 0.75 to 30  $\mu\text{m}$ , which corresponds to 0.00124 to 0.0495 eV in the energy domain. The solar radiation follows approximately a black-body spectrum. Over 99% of the radiation is emitted between 0.2 and 10  $\mu\text{m}$ . Particularly, 53% of the photons are radiated in the infrared region. Therefore, infrared observations of the Sun are really important. In addition, infrared observations around 1.56  $\mu\text{m}$  have several special advantages compared to visible light observations.

### 1.4.1 Better Seeing Conditions

Seeing is a very serious limitation for ground-based solar observations. It is affected by the Earth's atmospheric turbulence, which results from either large scale or small scale convection. Seeing is defined as the degradation of image quality by fluctuation of the refractive index in the light path (Stix 2002). The Earth's atmospheric turbulence is driven by the Sun itself. Therefore, solar observations can not avoid this problem as for example in the case of a general astronomical problem in the night-time observations. Solar radiation heats the ground and thus initiates local convection. Even inside the dome, localized turbulence can be generated. The temperature gradient affects the refractive index and hence distorts the wave-front. Bad seeing conditions lead to three different aspects of image degradation. First, blurring is a de-focussing effect similar to the smooth function in image processing. Second, image motion causes the rapid shifting of images. Third, image distortion is the differential shifting of different parts of images. There are a few options we can choose from to correct these effects, such as Active Optics, Adaptive Optics, speckle mask reconstruction, phase diversity, etc. The first two solutions use hardware correction. The other two rely on software and are called after-the-effect corrections.

The seeing is not uniform in the whole electromagnetic range, i.e., it varies with wavelengths. The Fried-parameter describes this relation (Stix 2002)

$$\begin{aligned} r_0(\lambda) &= (0.423 k^2 \int_0^\infty C_n^2(Z) dz)^{-3/5}, \\ &= 0.185 \lambda^{6/5} (\int_0^\infty C_n^2(Z) dz)^{-3/5}. \end{aligned} \tag{1.24}$$

The atmospheric turbulence of a given layer is characterized by  $C_n^2 \Delta h$  for a refractive index. When the turbulence extends across the whole height,  $C_n^2 \Delta h$  becomes  $\int_0^\infty C_n^2(Z) dz$ , where  $k$  is the wave number. Therefore, the Fried parameter is proportional to  $\lambda^{6/5}$ , i.e., the seeing conditions at longer wavelengths are better than at shorter wavelengths. The observations presented in this dissertation are good illustrations of this point.

Seeing conditions can also be improved by choosing a proper site for the placement of a telescope, such as in the middle of a lake (Huairou Observatory, China), at high altitude (Mouna kea Observatories, Hawaii, and the National Solar Observatory/Sacramento Peak (NSO/SP), New Mexico.) or both (Big Bear Solar Observatory (BBSO), California). BBSO exploits the excellent climatic conditions of Big Bear Lake. The primary target of our observatory is the Sun, as well as the Moon is being observed during the night. The observatory is located in the middle of Big Bear Lake, which is located at an elevation of about 2,000 meters (6,750 feet), in order to reduce the seeing effect. The huge thermal capability of the lake itself also contributes to the absorption of solar heating and hence reduces the turbulence near the ground. These conditions provide a stable seeing condition and make the BBSO a premier site for solar observations. The observatory was built by the California Institute of Technology in 1969 and was transferred to the New Jersey Institute of Technology on July 1, 1997. Figure 1.16 shows the dome and the causeway at Big Bear Lake.

One reflecting telescope with diameter of 65 cm and three refracting telescope (15 cm, 20 cm, and 25 cm) are integrated together on a single fork mount on the top floor of the dome (see Figure 1.17). Both routine and specialized observations are carried out with the telescopes with highly specialized filters and cameras. The observed spectrum ranges from the NIR and visible to the ultraviolet.



**Figure 1.16** Picture of the dome and the causeway at the Big Bear Lake. This figure is from <http://bbso.njit.edu>, 2005 August 1.

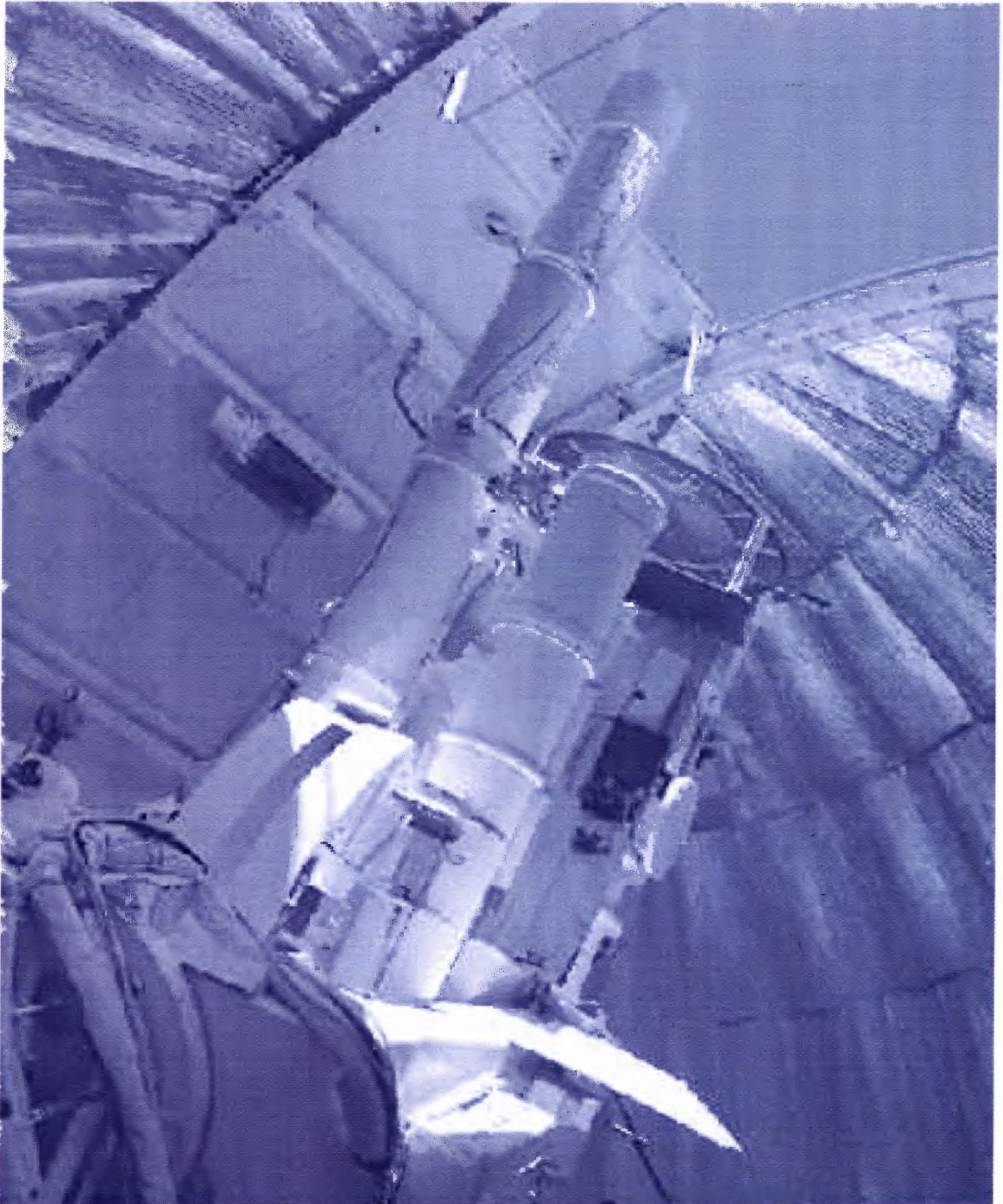
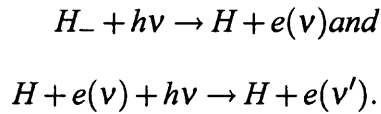


**Figure 1.17** The BBSO 65 cm reflecting telescope and three refracting telescopes (15 cm, 20 cm, and 25 cm). (From <http://bbso.njit.edu>, 2005 August 1.)

### 1.4.2 Opacity Minimum

In 1939, Wild proposed an absorption model to solve the problem of the Balmer jump variation observed in the spectrum of A0 stars. In this model, the absorption is due mainly to  $H^-$ , which is the combination of a Hydrogen atom and an electron. Since a Hydrogen atom has only one electron, the electric field of its nuclear can not be fully shielded. When an electron passing by, it will fall into the residual electric field and forms an  $H^-$  ion. The ionization potential of an  $H^-$  ion is only 0.75 eV and the corresponding absorption wavelength is about 1.6  $\mu\text{m}$ . Thus, photons with energies higher than 0.75 eV are able to ionize  $H^-$  and generate bound-free and free-free absorption



By solving the Boltzmann (Equation 1.25) and Saha (Equation 1.26) Equations

$$\frac{N_{r,k}}{N_{r,i}} = \frac{g_{r,k}}{g_{r,i}} e^{-\frac{\epsilon_{r,k} - \epsilon_{r,i}}{kT}}, \quad (1.25)$$

$$\frac{N_{r+1}}{N_r} N_e kT = \frac{2u_{r+1}(T)}{u_r(T)} \frac{(2\pi m_e)^{3/2} (kT)^{5/2}}{h^3} e^{-\frac{\chi_r}{kT}} \quad (1.26)$$

in the visible and NIR region, the  $H^-$  bound-free and free-free transitions are the principle absorption sources. The values of  $u_r(T)$  and  $\chi_r$  can be found in existing tables (Cox 2000). The calculations done by Chandrasekhar et al. (1946) show that the bound-free absorption reaches its maximum at 0.87  $\mu\text{m}$  and has the same value as free-free absorption at 1.6  $\mu\text{m}$ . The total absorption by  $H^-$  is shown in Figure 1.18 (see Doughty & Fraser (1966a); Doughty et al. (1966b); Stix (2002); Unsold & Baschek (1999) for additional details). The NIR region around 1.6  $\mu\text{m}$  reflects the opacity minimum. Therefore, observing in the NIR around 1.6  $\mu\text{m}$  allows us to probe the deepest layer of the photosphere. That is one of the motivations to investigate solar activity using NIR observations at 1.6  $\mu\text{m}$ .

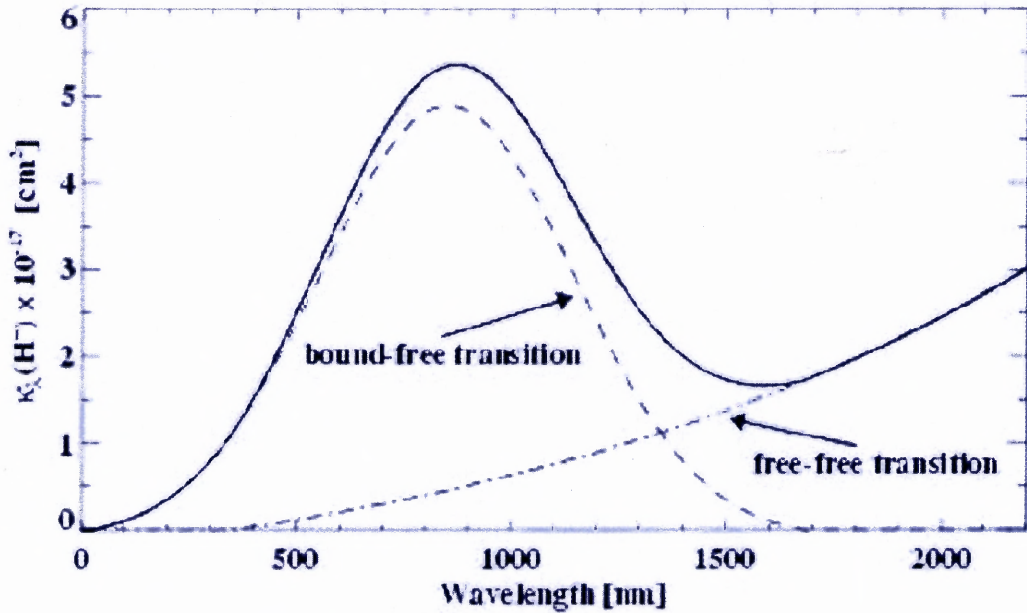


**Figure 1.18** This plot shows the total opacity at the photospheric level due to  $H^-$  absorption including bound-free transition (dotted-dashed line) and free-free transition (dashed line). (Adapted from the class notes of Dr. Sitko in the Department of Physics, University of Cincinnati, more details can be found in Doughty & Fraser (1966a); Doughty et al. (1966b).)

### 1.4.3 Less Requirements for Adaptive Optics System

The purpose of Adaptive Optics (AO) systems is to flatten the distorted wavefronts. The two major steps involved in an AO system are measuring and correcting the wave-front distortion. The distortion is detected by a Shack-Hartman (Hartkorn 2003; L'ena et al. 1998) wavefront sensor and then sent to a computer, where the measurements are converted to drive-signals for the second step, which is correction by a deformable mirror. The diagram of the AO system at NSO/SP is shown in Figure 1.19. The degree of the AO correction depends on the sensor and the number of the wavefront sensor and the number of actuators,  $N$ .  $N$  is proportional to the diameter of the telescope  $D$  and the Fried-parameter  $r_0$ . For a given telescope with a constant diameter,  $r_0$  is a function of  $\lambda$ . Therefore,

$$N \approx (D/r_0(\lambda))^2 \propto \lambda^{-12/5}. \quad (1.27)$$

Apparently, the larger the wavelength  $\lambda$ , the fewer the actuators are required. An AO system is easier to control with fewer actuators in the NIR band.

#### 1.4.4 Less Scattered Light

It is important to consider two kinds of scattered light. One is due to the Earth's atmosphere and the other is caused by the instruments themselves. In the first case, both Rayleigh and Mie scatter are proportional to  $\lambda^{-n}$ . Therefore, this scatter light is weaker in the NIR band than in the shorter wavelengths of the visible. Similar to atmospheric turbulence, instrumental scatter light is proportion to  $\lambda^{-2}$  (Elson et al. 1979).

#### 1.4.5 Larger Zeeman Splitting

Infrared observations provide a powerful tool for investigating solar magnetism. Line splitting due to the Zeeman effect is

$$\Delta\lambda_B = \frac{e\lambda^2 gB}{4\pi m_e c^2} = 4.67 \times 10^{-13} \lambda^2 gB \quad (1.28)$$

and remains the theoretical bedrock for the solar magnetic field measurements. In the NIR band, the Zeeman splitting for a certain field strength is larger than in the visible band resulting in a more sensitive measurement in the NIR.

#### 1.4.6 Other Advantages and Some Issues of the NIR Observation

NIR observations are good for the study of solar macroscopic electric fields (Foukal 1996), coronal magnetic fields, filament magnetic fields, etc. Particularly, in this dissertation, NIR observations are used to study flare emission.

On the other hand, there are some difficulties and disadvantages associated with ground-based NIR observations. Firstly, it requires larger telescopes to resolve the same

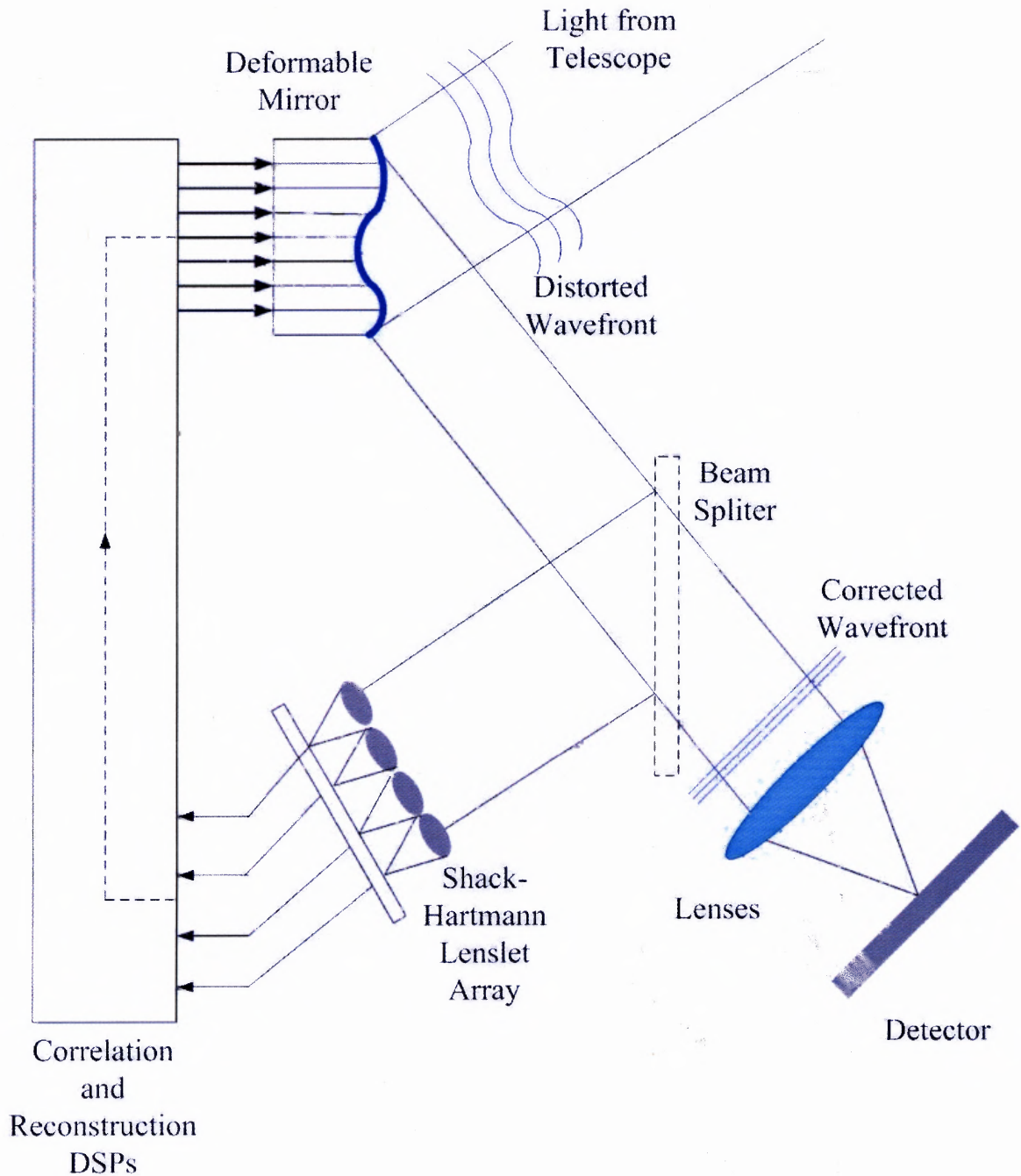


**Figure 1.19** The basic setup showing the working-principle of the Adaptive Optics System at NSO/SP. For a detailed description of the AO system, see Hartkorn (2003); L'ena et al. (1998).

structure resolved in the visible, i.e., for a given telescope, the spatial resolution for NIR is not as high as for visible since the resolution is defined as

$$\delta = 1.22 \frac{\lambda}{D}. \quad (1.29)$$

Secondly, the Earth's atmosphere is not totally transparent in the infrared. From Figure 1.2, we can see that only part of infrared light can pass through the atmosphere and reach the ground. These bandpasses can be separated into a few windows, namely J (1.2  $\mu\text{m}$ ), H (1.6  $\mu\text{m}$ ), K (2.2  $\mu\text{m}$ ), L (3.4  $\mu\text{m}$ ), M (5  $\mu\text{m}$ ), N (10  $\mu\text{m}$ ) and Q (22  $\mu\text{m}$ ). The H window is the window we observed. Thirdly, the strong thermal background can causes problems, especially towards the middle and far infrared wavelengths.

## 1.5 Outline of this Dissertation

The physical aspects addressed in this dissertation are solar white-light flares and small scale magnetic structures. The principle investigative tools are the NIR imaging system and the HOAO system. White-light flares are among the most energetic solar events. Previous observations have shown that white-light emission is always associated with strong flares in an X-ray classification greater than M5 (Rust 1986). Therefore, the study of solar flares, particularly white-light flares, provides us with a great opportunity to learn more about the physical processes behind high energy phenomena. In addition, the study of small-scale magnetic features, which are thought to contribute to the variation of solar irradiance is equally important because the effects of solar radiation are closely related to the Earth's environment.

This dissertation includes an introduction and two chapters which address different scientific topics, plus a final summary and discussion. The four chapters are:

Chapter 1: *Introduction.*

In this chapter, relevant scientific topics are reviewed. It starts with basic knowledge

of the Sun, from the innermost core to the outermost corona (Section 1.1). In Section 1.2, solar flares are introduced. The overall picture of a solar flare follows three steps: magnetic energy buildup, trigger, and energy release. For each step, there are several possible models which attempt to explain the physics involved. In Section 1.3, the fundamental magnetic elements are discussed. Flux tubes appear visible as both dark sunspots and pores and as bright faculae. In Section 1.4, observation in the NIR spectral range is discussed. NIR observation provides many advantages to the study of the Sun. The most important observations discussed in this dissertation were made in the NIR at  $1.56 \mu\text{m}$ . Most of the topics in this chapter are relevant to detailed research topics, which are presented in the following two chapters.

#### Chapter 2: *White-Light Flares Observed in the Near-Infrared.*

This chapter includes studies of two white-light flares observed in the NIR, visible continua and G-band. After a detailed introduction to white-light flares (Section 2.2), the specifics of the observation process are presented, and the new instruments are discussed. The very first NIR observations of white-light flares are studied including the contrast enhancement of flare ribbons, the comparison of light-curves in HXR with different energy ranges and NIR, the ribbon separation speed, the inferred electric field in the reconnection region, and the comparison of NIR, visible white-light and G-band images. Several models that are candidates to explain the significant NIR and other optical emission are discussed.

Preliminary results have been published in the *Astrophysical Journal Letters*, 2004, v. 607, p. 131. More comprehensive results were submitted to the *Astrophysical Journal* for publishing.

#### Chapter 3: *Properties of Fine Magnetic Structures.*

This chapter can be separated into three parts. In Section 3.2, small-scale structures are introduced in detail. In Section 3.3, I present an account of our first approach

to searching for “dark faculae” and related phenomena, such as the relationship between the intensities and magnetic flux densities. In the third part (Section 3.3), improved observations and results are discussed. With the newly developed NIR Lyot filter, the first “line-free” continuum images in the NIR were obtained with the HOAO system. My study shows the non-existence of “dark faculae”.

My results have been published in the *Astrophysical Journal Letters*, 2005, v. 628, p. 167, and in the *Chinese Journal of Astronomy and Astrophysics*, 2004, v. 4, p. 481.

At the end, I summarize my work in Chapter 4.

Chapter 4: *Summary*.

In this Chapter, I summarize my work.

## CHAPTER 2

### WHITE-LIGHT FLARES OBSERVED IN THE NEAR-INFRARED

#### 2.1 Abstract

In this chapter, I present high resolution observations of an X10 and an X8 white-light flares in solar active region NOAA 10486 obtained with the Dunn Solar Telescope (DST) at the National Solar Observatory/Sacramento Peak (NSO/SP) on 2003 October 29 ( $\sim 20:40$  UT) and November 2 ( $\sim 17:16$  UT), respectively. The investigation pays much attention to flare dynamics as observed in the near-infrared (NIR) continuum at  $1.56 \mu\text{m}$ . This is the very first report of white-light flares observed at the opacity minimum. The spatial resolution was close to the diffraction limit of the 76 cm aperture DST and the temporal resolution was as high as 2 seconds. The data benefited from a newly developed high-order adaptive optics (HOAO) system and a state-of-the-art NIR complex metal oxide semiconductor (CMOS) focal plane array (FPA). Detailed study is presented in this chapter comparing photospheric continuum observations during two events with corresponding line-of-sight magnetograms of the Michelson Doppler Imager (MDI) and hard X-ray (HXR) data of the Ramaty High Energy Solar Spectroscopic Imager (*RHESSI*). Based on the observational results, several models that provide possible mechanisms to explain these continuum enhancements, especially in the NIR, are discussed.

#### 2.2 Introduction

##### 2.2.1 White-Light Flares

As introduced in chapter 1, flares are generally regarded as a result of sudden magnetic energy release in the reconnection current sheet in solar corona. Charged particles like electrons and protons are accelerated. A large number of accelerated particles can precipitate along the magnetic field lines and lose their energy in the lower atmosphere (for in-

stance, chromosphere). During the course, microwave radiation is generated due to a gyro-synchrotron process, and hard X-rays (HXRs) are emitted through thick-target bremsstrahlung process (Brown 1971; Emslie 1978). Among all flares, the most energetic flares are white-light flares or “photospheric flares” (Najita & Orrall 1970). They are defined as those flares with emissions in the visible continuum or integrated light (Neidig 1989). They always require a larger high-energy particle flux and less relaxation time than ordinary flares (Neidig 1989). Observations of white-light flares in the visible continuum have been reported by a number of authors (e.g., Canfield et al. 1984; Canfield & Gayley 1987; Hawley & Fisher 1994). They may be associated with the most energetic particles, which play a crucial role in the energy transport of flares (Neidig et al. 1993b). Substantial amount of work has been undertaken trying to understand the following two fundamental problems: (1) Where does this kind of visible and NIR emission originate? (2) What is the energy source? The answers of these question are intertwined. In the following section, three flare models are introduced attempting to answer these questions.

### 2.2.2 The Flare Emission Models

#### *Direct heating by non-thermal electrons and protons*

The initial theory describing WLFs was based on observations that white-light flare emission was always associated with HXR emission. Therefore, non-thermal electrons or protons accelerated in the corona are thought to be the energy carrier (Lee et al. 1996; Rust & Hegwer 1975; Hudson 1972). They deposit most of their energy in the lower atmosphere, even near the  $\tau_{5000} = 1$  level (Najita & Orrall 1970). Under this hypothesis, the white-light emission is caused by non-thermal electrons and protons precipitating to chromosphere and photosphere. The high energy particles are thermalized by collisions and can create ionization, which enhances the bound-free and free-free continuum emission (Ding 2003a; Ding et al. 2003b; Hudson 1972; Najita & Orrall 1970). The relation between the column density

$N$  of a certain layer and the initial energy of electron beam is given by Emslie (1978)

$$E_N = \left[ \left( 2 + \frac{\bar{\beta}}{2} \right) \frac{\bar{\gamma} \kappa N}{\mu_0} \right]^{1/2}, \quad (2.1)$$

where  $\mu_0$  is the cosine of the angle between the initial velocity vector and the direction perpendicular to solar surface.  $\kappa = 2\pi e^4$ ,  $\bar{\beta}$  and  $\bar{\gamma}$  are the mean values along the electron trajectory of  $\beta$  and  $\gamma$ , which were defined in Emslie's paper as

$$\beta_e = \frac{2x\Lambda + (1-x)(\Lambda'' - \Lambda')}{\Lambda' + x(\Lambda - \Lambda')}, \quad (2.2)$$

and

$$\gamma = x\Lambda + (1-x)\Lambda', \quad (2.3)$$

where  $x$  is the ionization rate of a certain layer of solar atmosphere and  $\Lambda$  is the Coulomb logarithm. Simplified by Machado et al. (1989) under the hypothesis of fully ionized plasma, the minimum energy of electrons to penetrate to a given atmospheric height, i.e., a mass column density  $m_0$  is given by

$$E_{min,e}^2 = \frac{6\pi e^4 \Lambda m_0}{m_H}, \quad (2.4)$$

where  $e$  is the electronic charge (e.s.u.),  $m_H$  the hydrogen mass, and  $m_0$  the mass-column. Therefore, only electrons with an extremely high initial energy of around 1000 keV (Neidig 1989) or protons with an energy higher than 20 MeV can penetrate to  $\tau_{5000} = 1$  level.

### *Chromospheric back-warming*

Many observations have shown that a flare-associated temperature enhancement can occur in the lower atmosphere around the temperature minimum region (TMR) and photosphere (Machado et al. 1978; Cook 1979; Mauas et al. 1990; Metcalf et al. 1990a; Liu et al. 2001).

However, it was hard to find sufficient electron flux to directly heat the photosphere, especially for relatively weak WFLs (Ding et al. 2003b; Metcalf et al. 1990b). Then, the chromospheric back-warming model was proposed to explain the photospheric heating. According to the spectroscopy observations, white-light flares are always characterized as type I and type II flares (Machado et al. 1986). Most observed white-light flares belong to type I flares, usually corresponding to the brightest events (Gan et al. 1992). The Type I continuum spectrum shows a significant Balmer and sometimes a Paschen jump. Therefore, the major energy source of type I white-light flares is thought to be chromospheric back-warming by recombination emission in Balmer and Paschen range (Chen & Ding 2005; Ding et al. 1999; Liu et al. 2001; Hudson 1972; Metcalf et al. 1990b). In this model, the electrons do not need to penetrate to deeper layers, most of them with a moderate energy greater than 20 keV stop at the upper chromosphere. They produce continuum emission by ionization and recombination. The emission will be re-radiated to lower layers and induce secondary ionization (photon ionization). Therefore, continuum emission is generated from deeper layers (Abouadarham & Hènoux 1986; Hudson 1972; Metcalf et al. 1990b). Therefore, two kinds of continuum emissions from both photosphere and chromosphere are mixed together and contribute to the observed WFLs. Neidig et al. (1993a) reported that flare kernels consist of a bright inner core, which corresponds to the direct heating in the chromosphere, and a weaker outer region, which corresponds to the back-warming emission. Therefore, there is a delay of few seconds in the 5000 Å continuum relative to HXR.

### *H<sup>-</sup> emission*

In some cases, the recombination continuum emission, which is the response to the photospheric heating in the back-warming model, could not be observed or was not significant. These flares are named as type II flares. Consequently, H<sup>-</sup> emission in the upper photosphere was proposed to explain the heating in the lower atmosphere (Metcalf et al. 1990b,

2003; Mauas et al. 1990; Machado et al. 1989; Ding et al. 1994, 2003b). The continuum emission is then mainly due to  $H^-$  emission in the upper photosphere and not related to a Balmer or Paschen jump. According to Aboudarham & Hènoux (1987), the non-thermal hydrogen ionization and excitation reach their maximum around the TMR. There, the electron number density is strongly increased during the flare and this leads in turn to an increase of the  $H^-$  population. Then, the  $H^-$  population enhancement can produce an increase of the absorption of continuum radiation of both photospheric and chromospheric origins. Eventually, the upper photosphere and below is heated by  $H^-$  continuum emission. Therefore, the observed emission is not only determined by precipitating electron beams but is also affected by local sources, i.e., the enhanced absorption of photospheric or chromospheric radiation. In some extreme case, upper atmosphere may even not be perturbed. Li et al. (1997) proposed a reconnection model in lower atmosphere of chromosphere rather than in the highly ionized corona.

#### *Other Models*

Aboudarham & Hènoux (1986, 1987) combined the back-warming model and  $H^-$  emission model. They showed that all layers from chromosphere to photosphere contribute to the white-light emission process. In particular, they concluded that even the TMR heating could be fully attributed to non-thermal electrons, and subsequently the photosphere is heated via radiative back heating. Recently, Ding (2003a) proposed a model of non-thermal electron beam heating plus  $H^-$  emission to explain the continuum enhancement near  $\text{Ca II } \lambda 8542$ , which is formed mostly in the photosphere. For a review of other mechanisms, such as heating by dissipation of electric currents, non-thermal proton beams, soft X-ray radiation, UV radiation and dissipation of Alfvén waves, see Metcalf et al. (1990b). Neidig et al. (1993a) compared the observed center-to-limb variation of 86 WLFs. They concluded that the observed center-to-limb variation of white-light emissions is most likely compatible with a source in the middle photosphere, or with a source in the middle photosphere

combined with one at higher altitude.

All the models and theories discussed above are in agreement with a hypothesis that the heating of chromosphere is fully caused by energetic electrons. But heating of the photosphere is still an open question.

### 2.2.3 Our New Observations

Xu et al. (2004a) reported the first observations of flare continuum emission in the NIR at  $1.56 \mu\text{m}$ . In the undisturbed atmosphere,  $1.56 \mu\text{m}$  is considered as the opacity minimum, i.e., it corresponds to the deepest layer in the solar atmosphere which is about 50 km lower than the  $\tau_{5000} = 1$  level (Wang et al. 1998). Therefore, the NIR observations provide additional boundary conditions for the theoretical modelling and numerical simulations. “The similarity between NIR and optical wavelengths also makes the NIR observations as a powerful tool for the further understanding of visible observations” (Ohki & Hudson 1975). In following section, I present a comprehensive study of two X-class WLFs observed in visible continuum at  $5200 \text{ \AA}$  NIR at  $1.56 \mu\text{m}$  and G-band around  $4308 \text{ \AA}$ . The data sets have the highest cadence and spatial resolution among all the existing filtergrams of flare studies. In addition, the seeing condition in the NIR is very stable. The result of auto-correlation for granulation areas of all the image sequences did show that the NIR image quality was much more stable than those in visible continuum and G-band. The rms contrast variation in the NIR is about 6.5% and in other two wavelengths are over 10%. Apparently, the NIR observations are the most reliable data sets for studying the flare morphology and dynamics. The objective of this study is to compare observations with the theoretical models discussed above and motivation for the future research of WLFs.

## 2.3 Observation and Data Reduction

As mentioned before, white-light emissions are very difficult to be detected in a typical flare. During some limb events, only 1% contrast enhancement can be generated and is too weak to be observed. That is the reason why the white-light flares were thought to be rare. Retrospect to the first white-light flare observed by Carrington and Hodgson in 1859 September 1, only about 60 flares were identified as white-light flares until the end of 1983 (Neidig & Cliver 1983). Started from 1980's, NSO/SP and BBSO carried out continuous survey of white-light flares. Instead of spectrographs, the multi-wavelength broad band filtergrams were obtained. Therefore broke the limitation of field-of-view (FOV) in spectrographs. Consequently, the sensitivity raised and more white-light flares were observed. As advertised above, besides the broad band in the visible light, NIR observations were carried out as well.

### 2.3.1 The New Near-Infrared Camera

The special designed TCM 8600 NIR camera is manufactured by Rockwell Scientific Imaging company. This is a Mercury-cadmium-tellurium type detector. For this kind of material, the spectral response is from 0.9 to 2.5 micron, covering J, H, K atmospheric NIR windows (Cao et al. 2005a; Denker et al. 2005; Xu et al. 2004a). It is based on a liquid nitrogen cooled Hg Cd Te/Al<sub>2</sub> O<sub>3</sub> focal plane array (FPA) with 1024 × 1024 pixels and 14-bit digitization depth. The quantum efficiency is better than 60% with a dynamic range better than 70 dB. The maximum frame rate can reach up to 30 frames per second. It uses the cam-link interface for communication between the host PC and camera electronics. Both the high speed image data, and low speed bi-directional communication are handled via this interface. Table 2.1 lists its performance specifications provided by Rockwell Scientific Imaging and a photo of the packed system is shown in Figure 2.1.

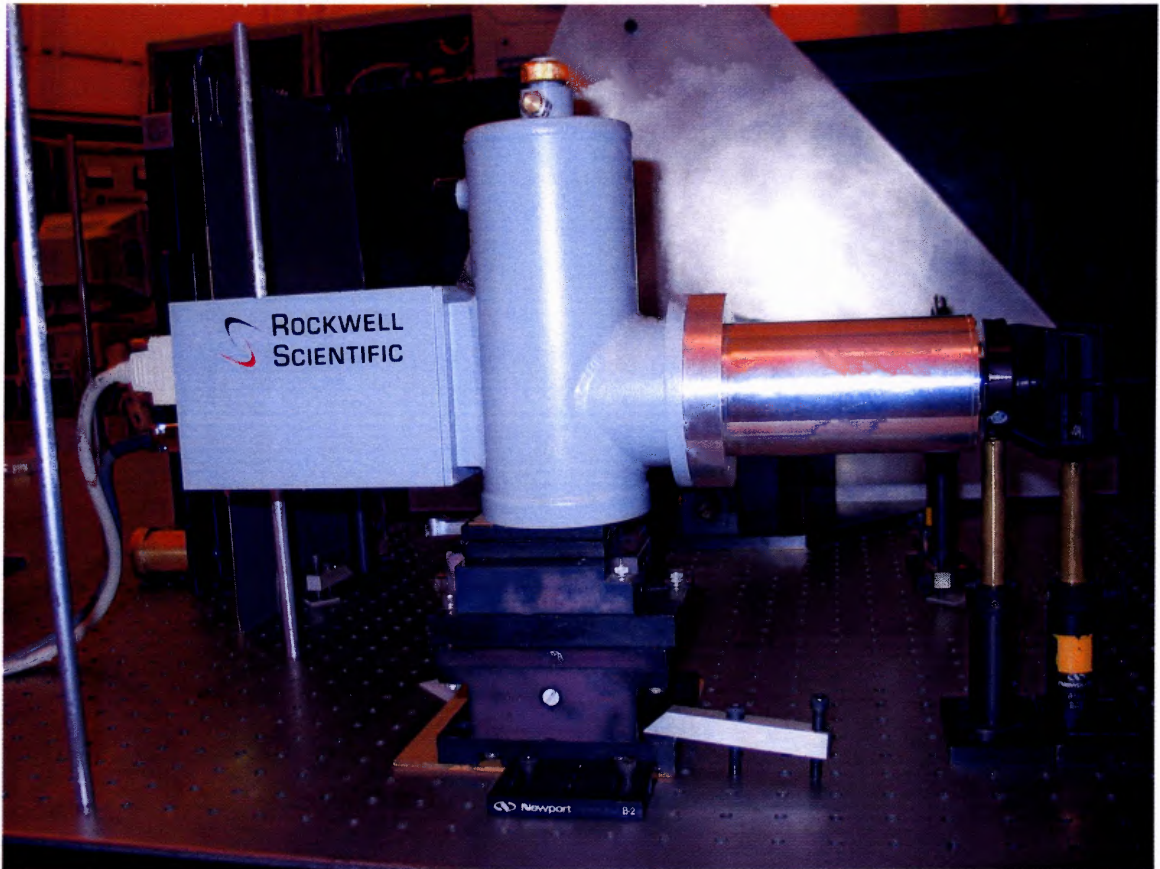


**Figure 2.1** The rockwell NIR camera, mounted in the optical table behind the interference filter and NDs.

**Table 2.1:** Specifications of the Rockwell Infrared Camera.

Material	HgCdTe ( MCT)
Wavelength	$1 \sim 2.5\mu\text{ m}$
Format	$1024 \times 1024$
Pitch	$18\mu\text{ m}$
Frame Rate	30 Hz
Well Capacity	400,000 carriers
Window	CaF1
Camera Output	14 bit
Data Acquisition	PCI Based Matrox Meteor Camera Link II
Camera Sync	Frame, Line, Pixel, Trigger
Readout	Ripple
Operation Temp	$\sim 80\text{ K}$ with $LN_2$

The BBSO NIR imaging system, basically including the Rockwell camera, a interference filter bought from Barr company and the controlling computer, was temporarily moved from BBSO, CA to NSO/SPK, NM. As well as a visible system including the Dalsa 1M15 digital camera and its computer system moved together.

### 2.3.2 The Telescope

The Dunn Solar Telescope (DST) is operated by NSO/SP, located in the Lincoln National Forest, Sunspot, New Mexico. It was built in 1973. The altitude of the mountains is above 9000 feet. The tower of the telescope rises 136 feet (or 41.5 m) above the ground level of one top of the mountains and has an approximately 220 feet (or 67 m) underground extension. Its optical system is very simple. The major reflection mirror has a diameter of 64 inch (or 1.6 m) combining with the 30 inch (or 76 cm) entrance window. Therefore, the effective diameter of the DST is 76 cm. Once the incoming light is focused by the primary mirror, the light will be sent to the HOAO system with 76 subapertures in the correcting deformable mirror. And then goes to a customized light path for certain purpose.

### 2.3.3 The Setup and Data Reduction

A diagram of the whole setup for the NIR, visible and G-band can be found in Figure 2.2. And a real time picture in Figure 2.3 gives the overhead view of the setup.

In the NIR channel, the field-of-view (FOV) was  $91'' \times 91''$  resulting in an image scale of  $0.089''$  per pixel. The diffraction limit at  $\lambda = 1.56 \mu\text{m}$  is  $\theta = \lambda/D = 0.42''$ , where  $D$  is the telescope aperture. Therefore, our data is over-sampled about 2.3 times providing more reliable information at high spacial frequencies. The exposure time was 13 ms, which is sufficiently short to freeze the atmosphere wavefront aberrations in the NIR. The bandpass was restricted to 5 nm by an interference filter. There are a few Fraunhofer lines within this 5 nm range, but they contribute less than 3% of all the radiation passing the

filter. Therefore, the continuum contamination is negligible.

Optics Setup @ NSO/SPK, Oct. 28 ~ Nov. 02, 2003

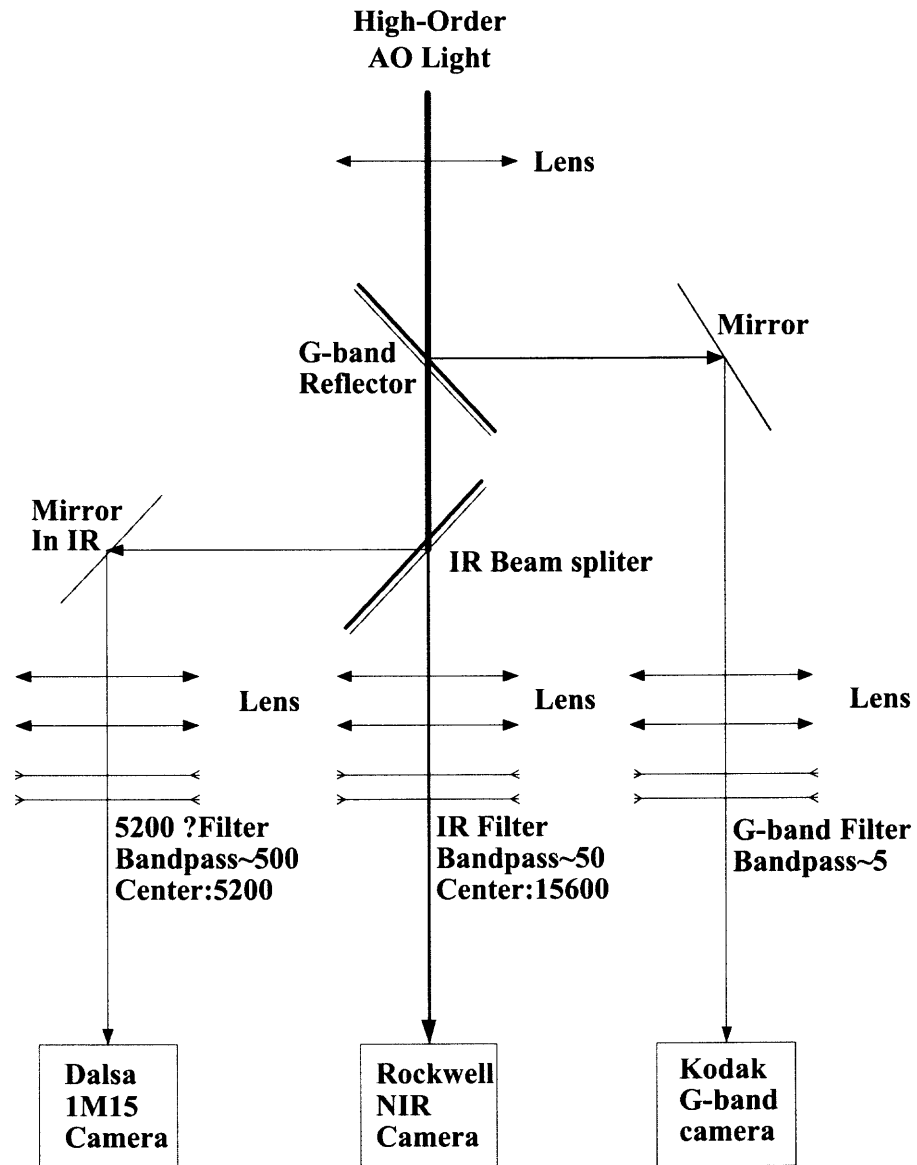
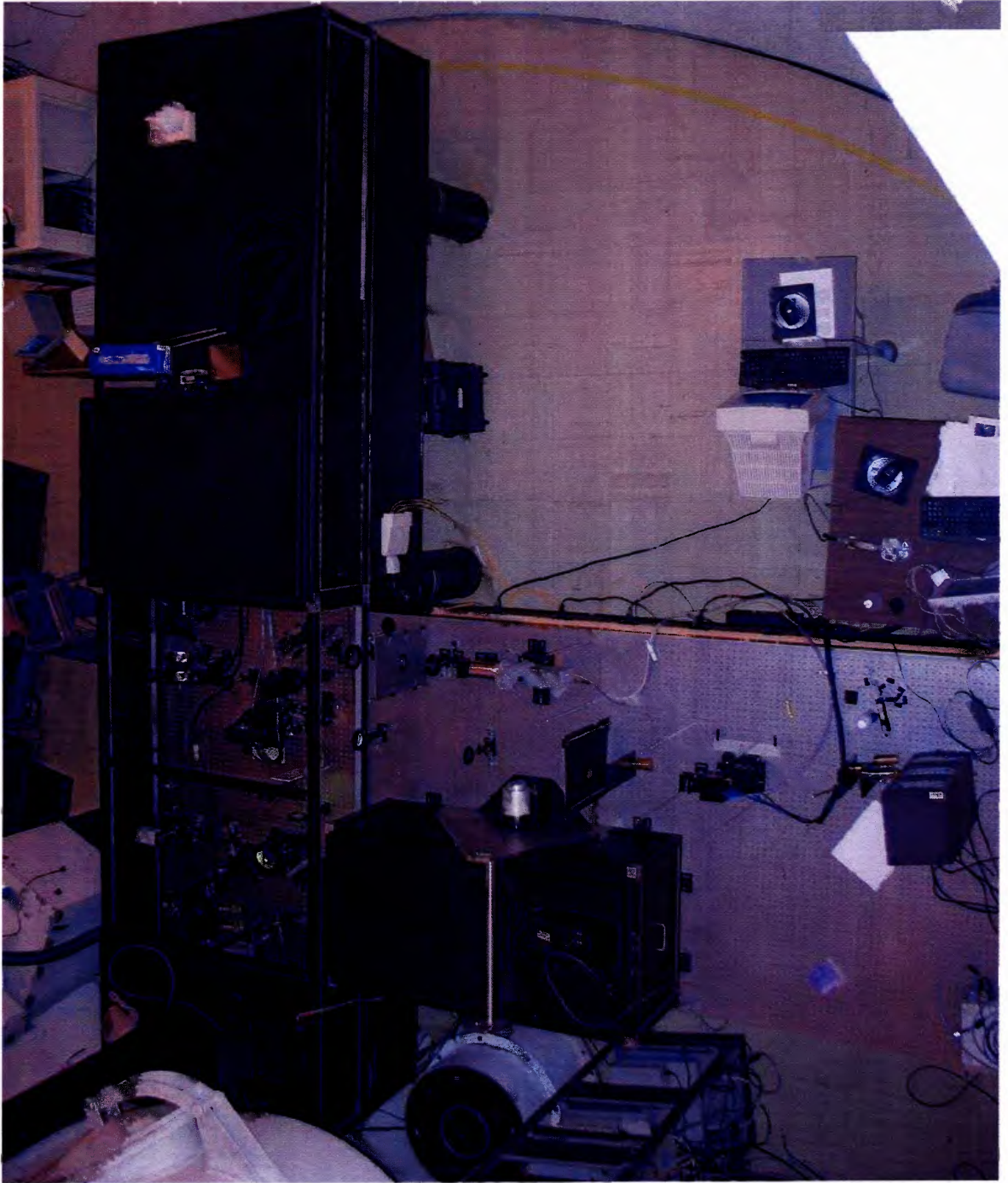


Figure 2.2 Setup diagram of the October-November observing run in 2003.



**Figure 2.3** A picture showing the real setup of Figure 2.2.

In addition, AO corrected data were simultaneously acquired in the visible-light channel and for speckle interferometric observations. The observations were taken in the green continuum centered at 520 nm with a bandpass of 52 nm by a  $1024 \times 1024$  pixels, 12-bit Dalsa 1M15 CCD camera. The exposure time was 4 ms and 100 frames were selected from 200 frames every minute. The FOV was  $81'' \times 81''$ . Details of speckle reconstruction procedure can be found in (Denker et al. 2005). Figure 2.4 shows a speckle reconstructed visible-light image taken at 16:48 UT and a high quality NIR image with flare kernels taken at 20:42 UT. The spatial resolution in both images approaches the diffraction limit of the DST. Furthermore, G-band observation in channel 3 was obtained simultaneously. The FOV was  $76'' \times 76''$  with the same chip size of  $1032 \times 1032$  pixel detector resulting the finest image scale of  $0.074''$  per pixel. Table 2.2 gives the overall details of the setup.

At the end of the first flare (October 29, 2003), the flare ribbons moved outside our FOV although they were very weak at that time. By noticing that and in order to cover more of the flaring area, we enlarged the FOV of the NIR observations on 2003 November 2 to  $122.2'' \times 122.2''$  resulting an image scale of  $0.119''$  per pixel. Although we lost the some of the ability to resolve small elements as we could in the first event, more information of the flare dynamics and longer time duration of the second flare were collected. The FOV was not changed for the other two wavelengths. The cadence was one minute for the 520 nm continuum and for the NIR continuum of the first event. All other data was observed with a cadence of two seconds.

**Table 2.2** Setup Details of the October-November Observing Run, 2003.

	NIR	Visible	G-band
Wavelength	$1560 \pm 2.5 \text{ nm}$	$520 \pm 26 \text{ nm}$	$430.5 \pm 0.5 \text{ nm}$
FOV	$91.2'' \times 91.2''$ (Oct.29) $122.2'' \times 122.2''$ (Nov.02)	$81'' \times 81''$	$72'' \times 72''$
Exposure	13 ms	4 ms	2 ms
Cadence	1 minute (Oct.29) 2 seconds (Nov.02)	1 minute	2 seconds

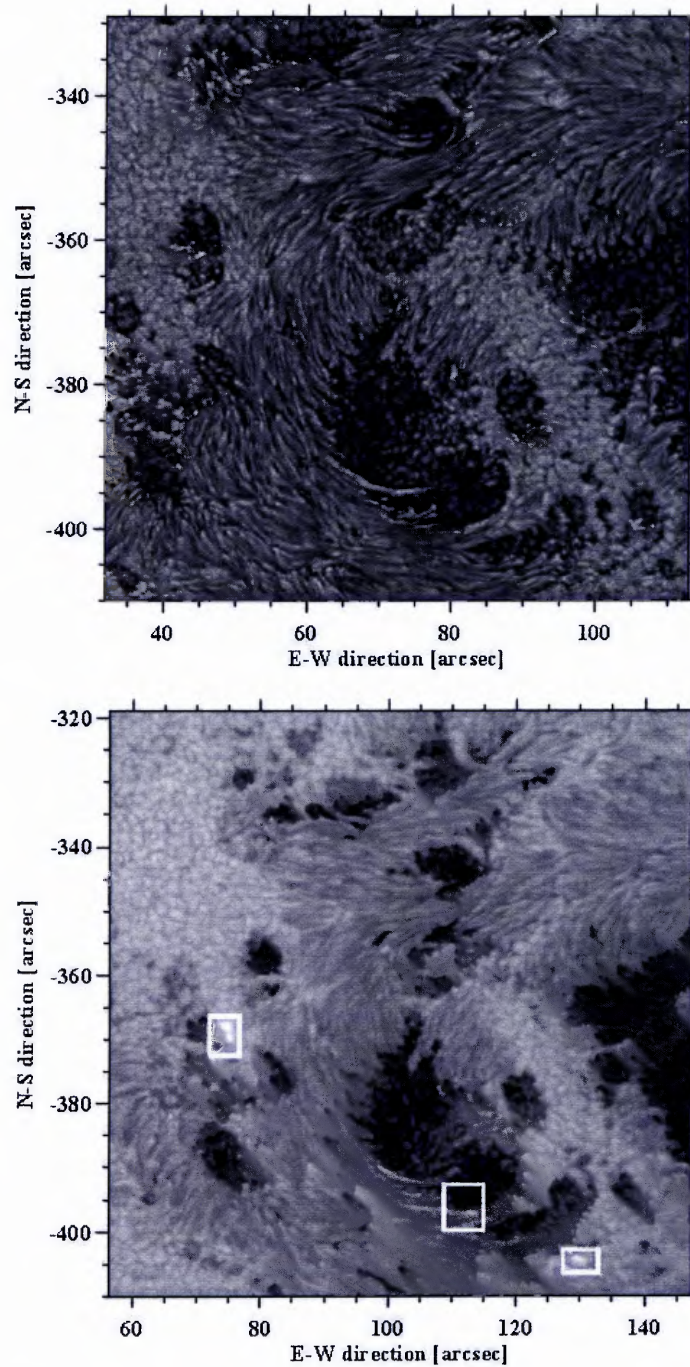


**Figure 2.4** Upper Panel: Speckle reconstructed image of active region NOAA 10486 obtained with frame selection and high-order AO system at 16:48 UT on 2003 October 29. The annotation of the axes refers to heliographic coordinates corresponding to a FOV of  $81 \times 81''$ . Lower Panel: NIR image of the same active region during the flare taken on 20:42 UT with a FOV of  $91 \times 91''$ . The bright patches marked by white boxes are NIR flare kernels.

All the images are dark and flat field corrected. For the first event, one best NIR frame with the highest granular rms-contrast was selected out of a total of 50 frames in each minute. And then image motion and differential image motion were removed from the final 1-minute cadence time sequence using the local correlation tracking method. Selection and reduction processes for other two wavelengths were similar to the NIR. The only difference is the cadences were not same. In order to study the dynamics, MPEG movies of the full resolution NIR time sequence were created. They clearly show the flare evolution and proper motion of the flare ribbons. Before generated the movie, all image sequences in the three bands were normalized with their best frames right before the occurrence of flares, respectively.

In order to see the ribbons more clearly, contrast enhanced difference maps were generated. The first step to enhance the contrast of NIR flare ribbons is to subtract each frame of the well aligned image sequence from a reference frame which was obtained right before the flare occurred. Then, we applied a high-pass filter to eliminate the background.

The last step is to register the optical images to the maps observed in the space, i.e., with SoHO/MDI and RHESSI. Since the images are aligned with one standard frame of each bandpass, only one image in each wavelength need to be registered. This step was done based on the feature recognition technic.

## **2.4 Results**

### **2.4.1 Overview of the Flares**

The X10 flare and the X8 flare observed in solar active region NOAA 10486 on 2003 October 29 and 2003 November 2. They were occurred exactly in the same area of the active region. The whole group of the sunspots was rotating and evolving as it moving across the solar disk. NOAA 10486 was one of the surprises during the declining phase of solar cycle No. 23 and produced several major flares including an X17.2 flare the previous

day and an X28 flare on 2003 November 4, which was the largest X-ray flare in the recorded history.

The flares are typical two ribbon flares, which are characterized by two separating ribbon like patches along the magnetic neutral line. Comparing to the compact flares that do not have moving ribbons, the two ribbon flares tend to be more energetic and always associated with erupting features, such as filament eruptions and CMEs.

The flare contrast enhancement is defined as usual (Neidig 1989; Neidig et al. 1993b; Ding 2003a):

$$C = \frac{I_f - I_b}{I_0}, \quad (2.5)$$

where  $I_f$  is the intensity of the flaring area,  $I_b$  is the intensity in the same area right before the flare and  $I_0$  is the undisturbed quiet sun background. Since each image sequences were normalized, the contrast enhancements are comparable with the change of time in each image sequence. The basic measurements of NIR and visible continuum emission during the two events are listed in Table 2.3. The maximum NIR continuum contrast enhancements were about 25% and 66% for two events, respectively. The visible emissions were stronger than the NIR, i.e., 45% and 76%, respectively. For the second event, when the NIR emission reached its peak, the visible emission also reached its maximum. However the visible images are more blurred than the NIR images. The G-band results are also included in Table 1. Although the CCD camera was saturated, the lower limit of G-band emission during the flares are 75% and 230% which represent the lower limits of contrast enhancements.

The NIR intensity enhancement of the flare ribbons is in the range of 18% and 25% compared to quiet sun background. The corresponding intensity enhancement from the visible continuum is 28% to 45%. We did not use the speckle reconstructed visible data to measure the contrast, only frame selection and a destretch procedure were applied. If we use the “canonical” flare model, the temperature raise can be calculated according to the intensity enhancement of a flare. Since it is approximately the black-body radiation.

**Table 2.3:** Basic Measurements of Two WLFs.

Event	October 29	November 2
Disk location	S17W10	S17W63
GOES X-ray class	X10	X8
Start time	20:39 UT	17:15 UT
Peak time	20:42 UT	17:17 UT
Contrast <sub>m</sub> <sup>NIR</sup>	25%	66%
Contrast <sub>m</sub> <sup>visible</sup>	45%	76%
Contrast <sub>m</sub> <sup>G-band</sup>	75%	230%
A <sub>total</sub> <sup>NIR</sup> (10 <sup>19</sup> /cm <sup>2</sup> )	1.69	1.13
V <sub>avg</sub> <sup>NIR</sup> (km/s)	29	24
E <sub>avg</sub> (V/cm)	23	22

According to Wang et al. (1998), the relation is given by

$$\frac{\Delta I}{I} = \frac{B(T_0 + \Delta T, \lambda) - B(T_0, \lambda)}{B(T_0, \lambda)}, \quad (2.6)$$

where the temperature perturbation is  $\Delta T_{NIR} \approx 1000$  K and  $\Delta T_{visible} \approx 500$  K during the emission maximum, and  $T_0$  is the photospheric temperature, which equals to 7600 K at 1.56  $\mu\text{m}$  and 6000 K at 0.52  $\mu\text{m}$  (Vernazza et al. 1981; Mauas et al. 1990), and  $B$  is the Planck function. The flare radiative loss is

$$\Delta L = 4\sigma T^3 \Delta T \quad (2.7)$$

(Najita & Orrall 1970). If we include the measured ribbon areas, we obtain an estimate of the energy release from 20:40 UT to 20:47 UT that is close to  $10^{24}$  J. For a typical flare, the flux of electrons with initial energy higher than 350 keV can not release such a huge amount of radiative energy within 8 minutes. In this case, the back-warming mechanism or the  $\text{H}^-$  emission give a more reasonable interpretation. Back-warming in combination with electron heating can explain NIR flare as mentioned by Ding et al. (2003b).

Similar G-band observations have been carried out by Hudson et al. (1992) with a bandpass of 3 nm. Although the origin of G-band radiation is still not clear (Rutten et al.

2001; Steiner et al. 2001), it does show a strong ribbon-like emission similar to that of the continuum.

## 2.4.2 Comparison of NIR with HXR

### *Morphology Comparison*

Figure 2.5 shows a time sequence of NIR images with superimposed RHESSI HXR contours. In order to align the NIR images with RHESSI HXR maps, TRACE white-light data were used as reference. Apparently, the flare emission in the NIR is well correlated with HXR both spatially and temporally. It does consist with the previously observed relationship between visible continuum and HXR emission. Therefore, the NIR emission is linked with HXR tightly.

### *Light Curves*

The NIR contrast enhancements as a function of time are plotted as light-curves in Figure 2.6. Because the NIR is less subject to seeing variation and it has higher temporal resolution, only the NIR light-curves are plotted for comparison with HXR light-curves in different energy channels. Two kinds of NIR light-curves are plotted. The one in red shows the total flux across the whole FOV as a function of time, defined as average light-curve (ALC). In order to eliminate the noise, a contrast threshold of 1% was used. For the second event, both ribbons were inside the umbral regions. A contrast threshold of 7% was used to exclude bright patches, which were not related to the flare. The black curve shows the average contrasts of the brightest pixels (90th percentile) as a function of time, defined as maximum light-curve (MLC), meaning only the brightest inner core was contributing to this light-curve.

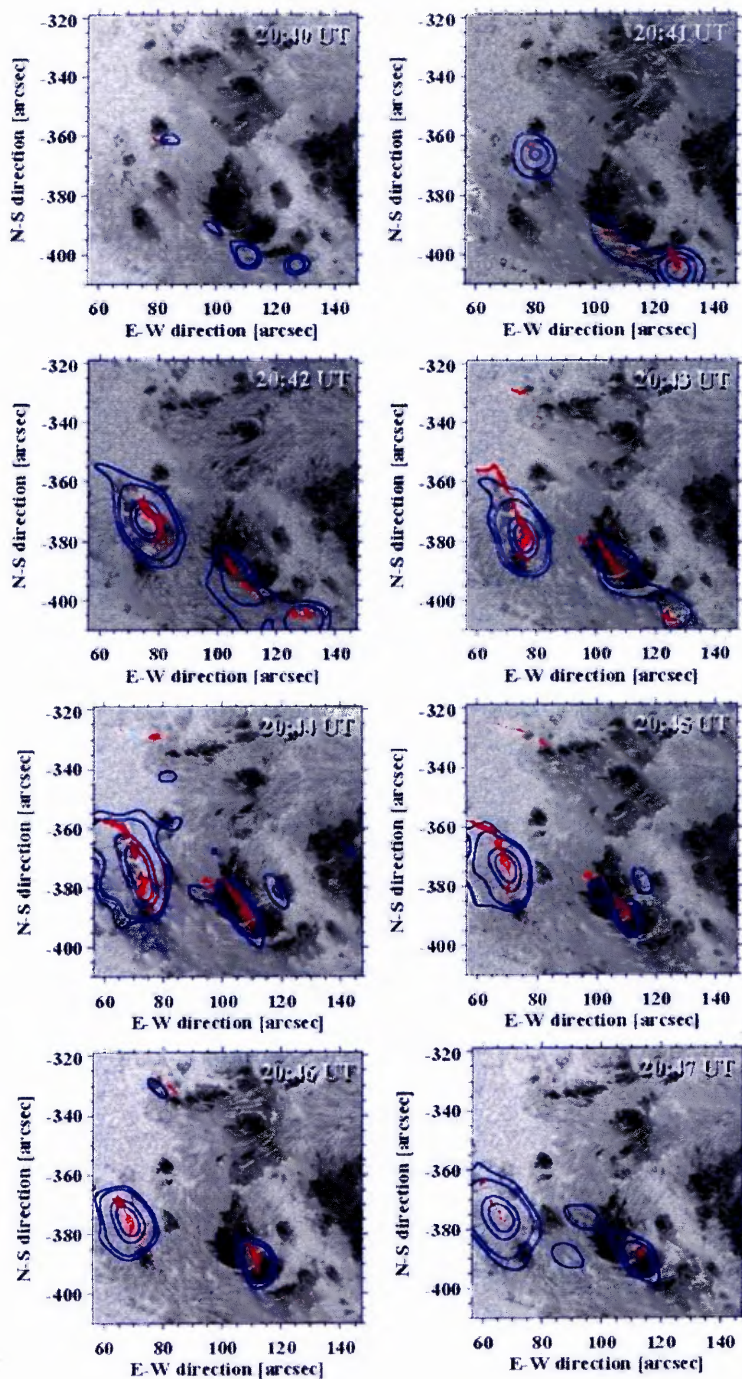


**Figure 2.5** NIR time sequence of the X10 flare from 20:40 UT to 20:47 UT on 2003 October 29. RHESSI HXR contours (blue) correspond to the 50 - 100 keV channel with 60 integration. The local NIR intensity maxima are shown in red. Two flare ribbons are correlated with strong HXR kernels. HXR contour levels are drawn at 0.17, 0.25, 0.60, and 0.80 of the maximum intensity, except for the first two frames, where they correspond to 0.7 and 0.8 for the first frame and 0.4, 0.6, and 0.8 for the second, when the HXR kernels were weaker.

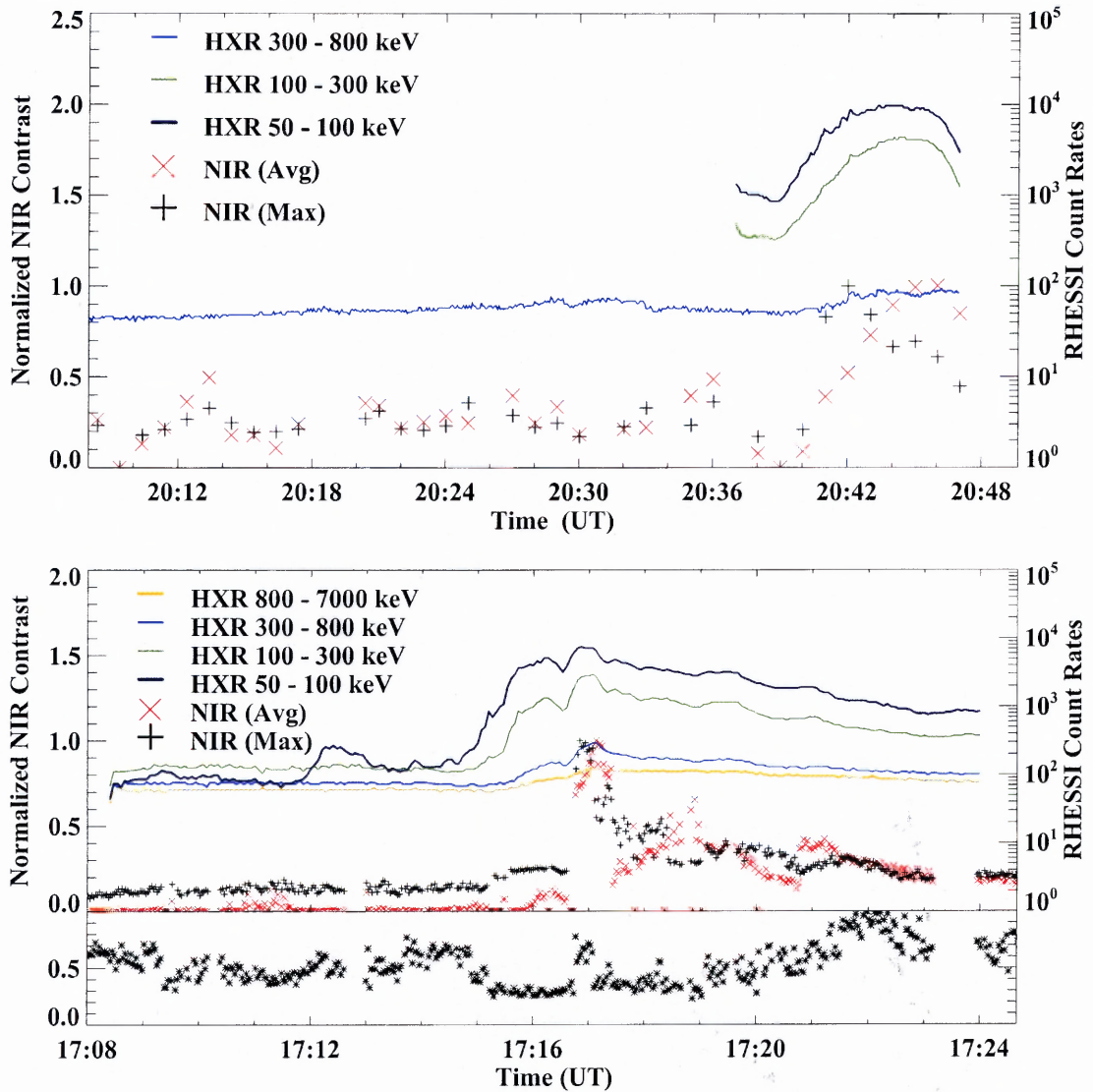


**Figure 2.6** Light-curves of the contrasts for the NIR and HXR flux in the X10 flare on October 29, 2003 (upper panel), and X8 flare on November 2, 2003 (lower panel). The lowest plot in lower panel shows the seeing variation in the second event. In the lower panel, the error for NIR ALC (red) is  $\pm 0.02$ , for NIR MLC (black) is  $\pm 0.031$ .

*ALC vs. MLC*

The two light-curves of the peak emission and integrated emission behave similarly but the MLC reached its peak about two minutes earlier than the ALC for the first event and about 20 s earlier for the second. Note that the cadence was one minute for the first event and two seconds for the second event, i.e., the time difference shown in the second flare is more significant. Overall, both of the NIR light-curves show the same variation tendency as the HXR with energy range from 50 keV to 300 keV in the first event and up to 800 to 7000 keV in the second event. We realize that the seeing conditions were less stable during the second event, especially during the period from 17:15:21 UT to 17:16:51 UT, as plotted in the lower panel of Figure 2.6. The effect of mediocre seeing leads to the intensity measurements much lower than their real value. However, this will not affect the distinct peak between 17:16 UT and 17:17 UT, when the seeing was improving.

*ALC vs. HXR*

According to Hénoux et al. (1990), Liu et al. (2001) and Neidig et al. (1993a), there is a time lag of less than one minute in the visible continuum and the continuum near Ca II  $\lambda$  8542 compared to HXR. This delay is due to heating processes of the photosphere and TMR via chromospheric recombination. In the first plot of Figure 2.6 for the first event, the HXR peaks around 20:43 UT and NIR ALC reaches its peak about 30 s later. This delay is shorter than the cadence of one minute. In the plot of the second event, the delay is about 20 s, which is 10 times the cadence. Therefore, it is much more significant.

*MLC vs. HXR*

On the other hand, if we use the inner core instead of the whole flare ribbon area, the NIR light-curve for the first event shows a peak at 20:42 when HXR also shows a relative small but very impulsive spike. In addition, this HXR spike is more obvious in the 300 to

800 keV range. This may be evidence of non-thermal heating of the inner core due to more energetic electrons.

### *HXR in Different Energy Ranges*

To explore the non-thermal properties of these two events, we also fit their X-ray photon spectra near the flare peak time observed by *RHESSI* using the Spectral Analysis Executive (SPEX) software package in Figure 2.7. The spectral fitting is conducted in the energy range of 10 to 400 keV and 10 to 500 keV for two flares, respectively. For both events, data of one orbit after the flare (the duration of a *RHESSI* orbit is about 96 minutes 40 seconds) is used for background subtraction for analysis within SPEX. The photon spectrum can be fitted with a thermal component and a non-thermal broken power-law component that has a power-law distribution of  $I(\epsilon) \propto \epsilon^{-\gamma}$ . For the first event, the power-law index  $\gamma$  of the photon spectrum is 3.6 and 4.2 with a spectral break at 127 keV. For the second event,  $\gamma$  is 2.8 and 3.6 with a spectral break at 109 keV. It is obvious that the second event is harder than the first one, meaning that there are more accelerated high energy electrons at  $\sim 50$  keV and above. The spectral fitting results are preliminary, since the pile-up correction is likely not very accurate for these extremely large events. However, we believe that this will not affect our conclusion. Note that, in the second event, the HXR with energy up to 800 to 7000 keV is also correlated with the NIR continuum and the correlation of other three energy ranges are much better than for the first event. In addition, the peak in 300 to 800 keV channel was much more obvious than in the first event. As shown in Figure 2.7, the power index  $\gamma$  in the second event is smaller, i.e., the second event has a harder electron distribution. Therefore, we can anticipate a relatively larger non-thermal electron flux with higher energy in the second event than in the first event.

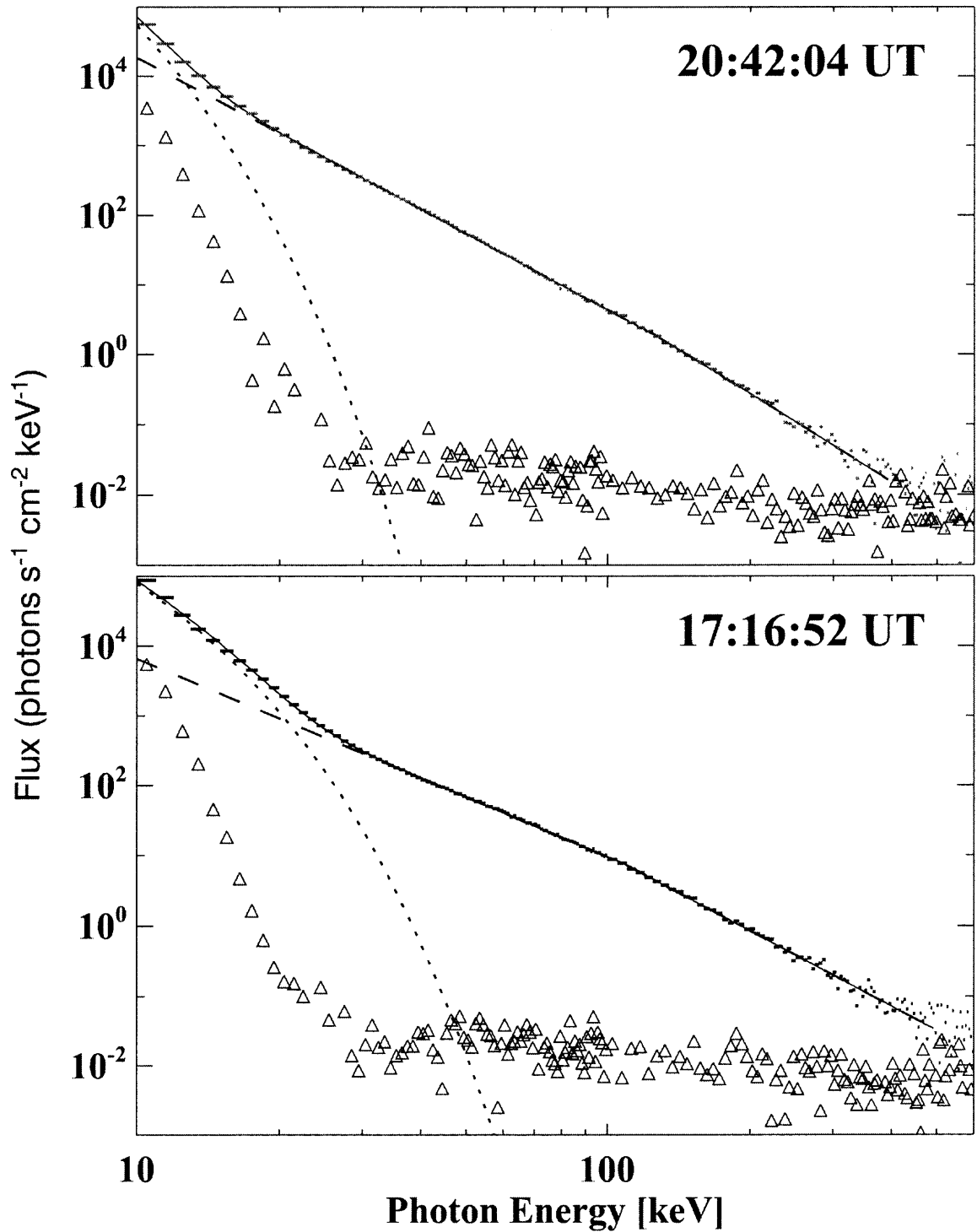
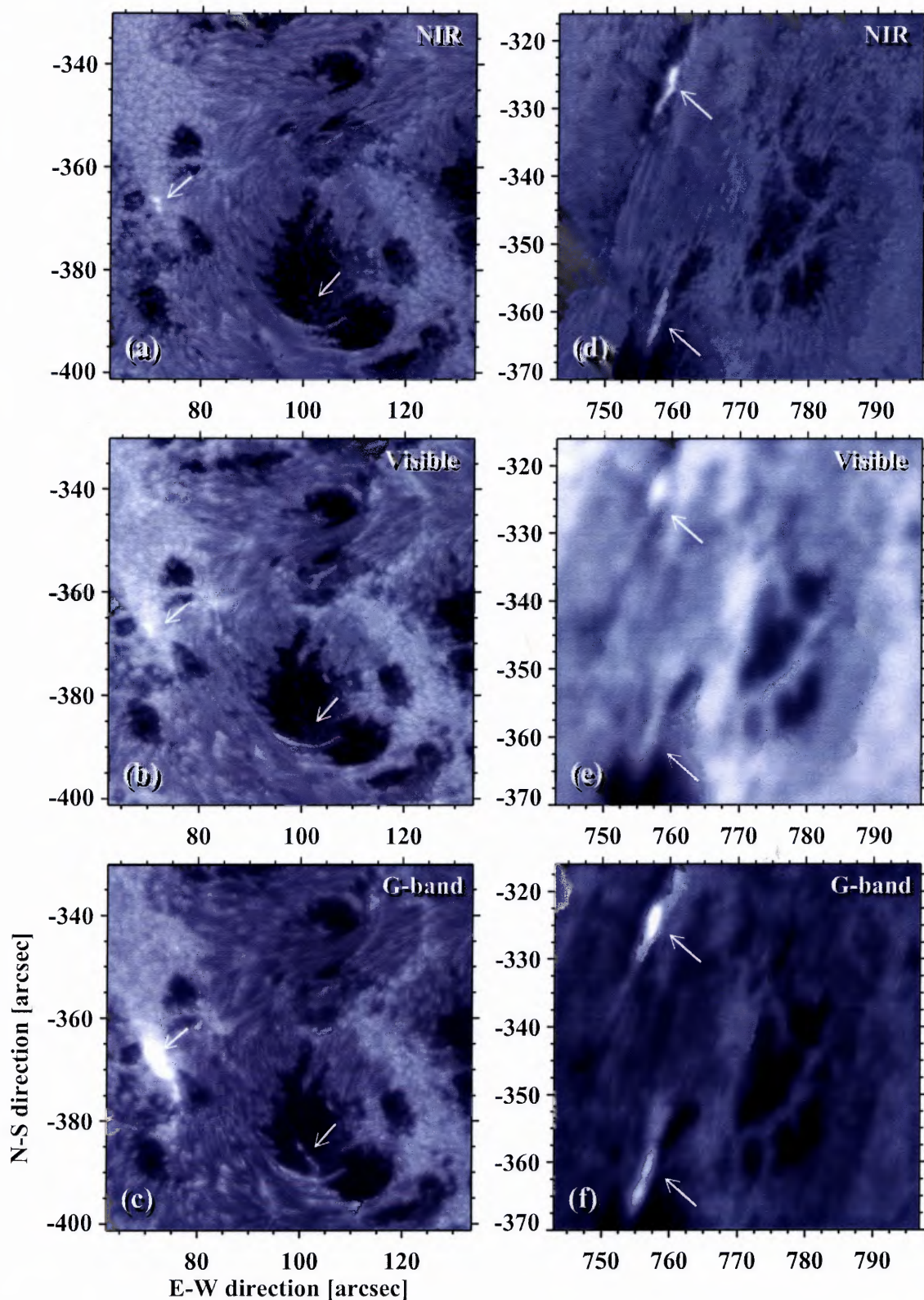


**Figure 2.7** Light-curves of the contrasts for the NIR and HXR flux in the X10 flare on October 29, 2003 (upper panel), and X8 flare on November 2, 2003 (lower panel). The lowest plot in lower panel shows the seeing variation in the second event. In the lower panel, the error for NIR ALC (red) is  $\pm 0.02$ , for NIR MLC (black) is  $\pm 0.031$ .

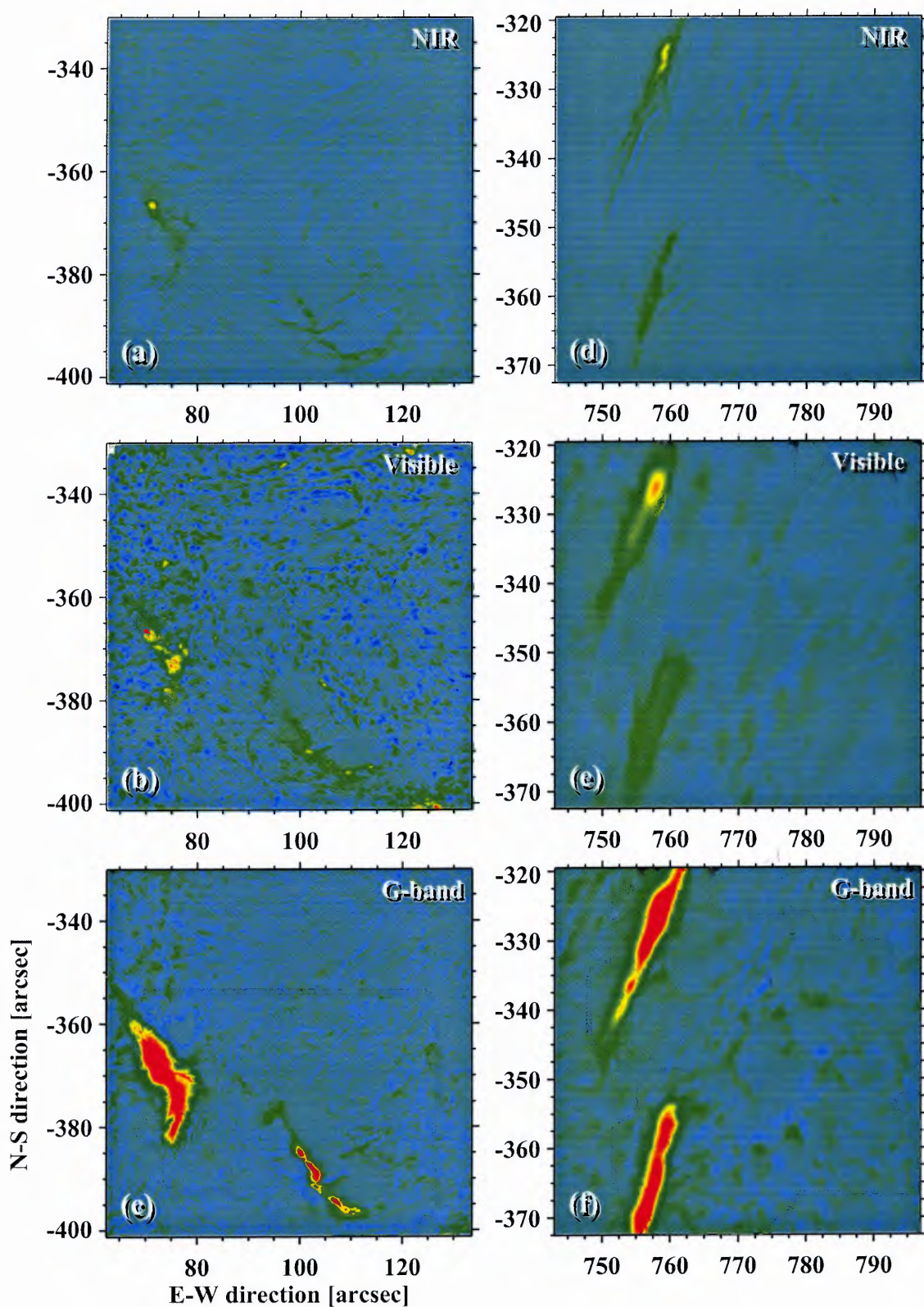
### 2.4.3 Comparison of NIR, Visible and G-band

Figure 2.8 shows the images during the flare peaks in three different wavelengths. The corresponding contrasted enhanced difference maps are presented in Figure 2.9. As discussed in chapter 1, the NIR light is coming from the deepest layer of photosphere. Visible continuum is emitted about 50 km higher than the NIR layer. Although people still do not know from where exactly does the G-band is being radiated, the radiation should be roughly emitted higher than the photosphere and has some chromosphere components because too many absorption lines are included. Nevertheless, the pictures in Figure 2.8 and Figure 2.9 provide a basic three dimension structure of the flare foot points. As we can see that the flaring area is getting smaller in the deeper layer. An X13 white-light flare was observed by Neidig et al. (1994). They found a similar variation of flare ribbons in a multi-wavelength observation. That observation was carried out in 3610 Å, 4275 Å and 6203 Å. The steep brightening change toward shorter wavelengths are thought to be common and an evidence of the Balmer jump. If this conclusion can be extended to our course, the flares presented in this dissertation should be able to classified as type I white-light flares.

An X1.8 white-light flare was observed on 1989 March 7 (Neidig et al. 1993a). At the flare peak, one of the flare ribbon in 5000 Å was separated into two parts, the bright core and a faint surrounding halo structure. Their explanation was that “these are adopted as the respective areas of the white-light flare emission for the two components of the kernel and the further assumed to be identical to the respective electron beam cross sections, in subsequent discussions of chromospheric heating via nonthermal electrons.” By adapting the idea from them, similar core-halo structures are able to be identified from the difference maps shown in Figure 2.9. With the sub-arcsecond resolution, the quantitative measurement is figured out. The smallest area ratio between the core and its halo is in the NIR band. Much larger core comparing with the halo structure is found in the visible continuum emission. In the G-band, it is hard to distinguish the two components, because the core is too strong and the center part of the flare kernel was saturated.



**Figure 2.8** Short-exposure images of active region NOAA 10486 obtained with frame selection and HOAO system at 20:42 UT on 2003 October 29 (left) and at 17:17 UT on 2003 November 2 (right). October 29. (top) NIR, (middle) visible (bottom) G-band. In each column (event), the FOVs are the same for all three wavelengths.



**Figure 2.9** Background-subtracted difference images in the NIR (top), visible (middle) and G-band (bottom) on 2003 October 29 (left) and 2003 November 2 (right). Images in the left column (first event) are scaled between  $\pm 0.35$ , images in right column (second event) are scaled  $\pm 1.0$ .

#### 2.4.4 Flare Dynamics and Electric Field in the Reconnection Region

Analyzing the NIR time sequence, we find very fast moving flare ribbons. The October 29 event is well studied, since the ribbons are thin and have almost no overlap among them, we can use difference images to illustrate the evolution of the flare emission more clearly (see Figure 2.10). After careful measurements, we found that the average speed of the two ribbons is around 38 km/s within regions of weak magnetic field and decreases to 19 km/s in regions with enhanced magnetic fields. These are typical values encountered in two-ribbon flares (e.g., Kitahara & Kurokawa 1990; Wang et al. 2003, 2004).

The separation motion of flare ribbons that sweep through the magnetic field lines correspond to the rate of magnetic reconnection in the corona, where the reconnecting current sheet is generated (Forbes & Priest 1984; Forbes & Lin 2000). Therefore, in a two dimensional configuration, the product of motion speed  $v$  and the normal component of the magnetic field  $B_n$  is just a measurement of the local reconnection rate. The reconnection rates in opposite polarities should be equal to each other. As showed in Figure 2.10, the NIR flare ribbons are located in opposite polarity areas. The speed of the ribbons travelling in weak magnetic fields is faster than in region where stronger magnetic fields are encountered. The relationship between the electric field strength  $E_c$  along the current sheet and two observables  $v_t$  and  $B_n$  were derived and simplified by Forbes & Priest (1984) and Forbes & Lin (2000),

$$E_c = v_t B_n \quad . \quad (2.8)$$

Since the active region is close to disk center on October 29 at  $\mu = \cos \theta \approx 0.9$ , the MDI longitudinal magnetic field  $B_{\parallel}$  can be used to measure the magnetic field  $B_n$ . The magnetic field strength is about 700 G in the weak region and 1400 G in the stronger region considering the measured velocities, the maximum electric field  $E_c$  is about  $45 \text{ V cm}^{-1}$  during the peak of HXR and NIR white-light emission.

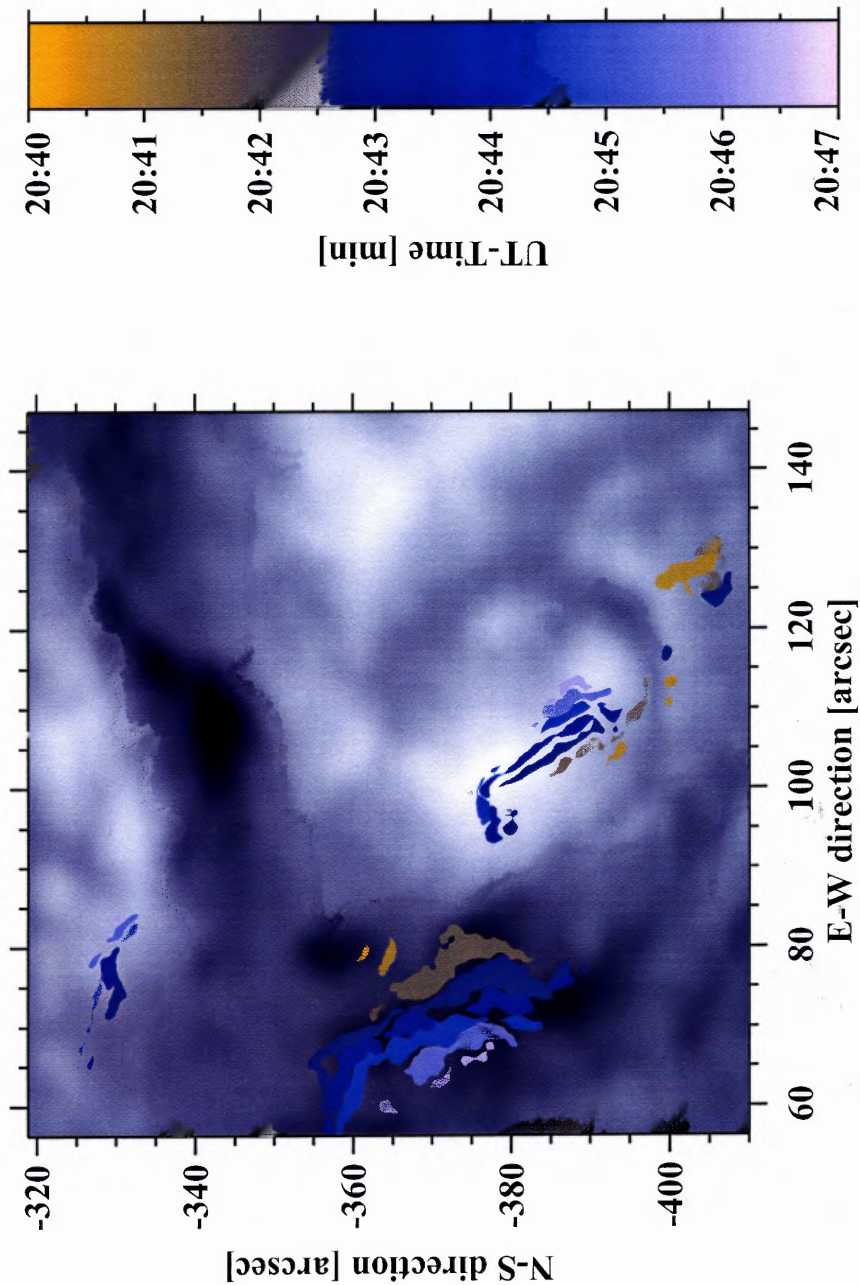


**Figure 2.10** Color-encoded NIR difference images showing the temporal evolution of the flare ribbons from 20:40 UT to 20:47 UT. The background is an MDI line-of-sight magnetogram. .

During the second event, the magnetogram had some temporary saturation effects as both of the ribbons swept through sunspot umbra. Therefore, the actual magnetic field should be stronger than its measured value, and the derived electric fields list in the table are smaller than the actual values. In Table 2.3,  $A_{\text{total}}^{\text{NIR}}$  is the average total area with flare emissions.  $V_{\text{avg}}^{\text{NIR}}$  is the average speed of ribbon separation after correction of geometric foreshortening.  $E_{\text{avg}}$  is the average electric field in the reconnection region. The values are 23 and 22  $\text{V cm}^{-1}$  in each event. They are the largest electric fields that have been reported using this method so far. Based on statistical results (Poletto & Kopp 1986; Qiu et al. 2002, 2004; Wang et al. 2003, 2004; Cheng et al. 2003; Jing et al. 2005), larger electric fields should be corresponding to larger numbers of energetic particles being accelerated during the events.

#### 2.4.5 Cooling Time

According to Najita & Orrall (1970), the atmosphere relaxes primarily by radiation after being heated by a flare. A certain relaxation time or cooling time is associated with each height in the atmosphere. In the photosphere, the cooling time is in the order of a few seconds (Mein 1966), while it increases to the order of 100 seconds in the chromosphere. With our high cadence and high resolution data, it is possible to measure the cooling time. We plot the average intensity of small areas with  $3 \times 5$  pixels covering the brightest kernel as function of time for the flares in Figure 2.11. Plots A1 to A4 are NIR light-curves in the first event of four different areas, which have a maximum contrast enhancement. C2 to C4 are for the G-band in the same event and the last four plots are for NIR light-curves in the second event. All the light-curves show two kind of relaxation profiles, a rapid plus a gradual cooling. A similar profile was found by Hudson et al. (1992). Since the size of selected flare areas are much smaller than the width of flare ribbons, this cooling profile is affected by the halo structures surrounding the flare cores. Therefore, measurements of the cooling time using the fast component represents the relaxation profile of the core structure.

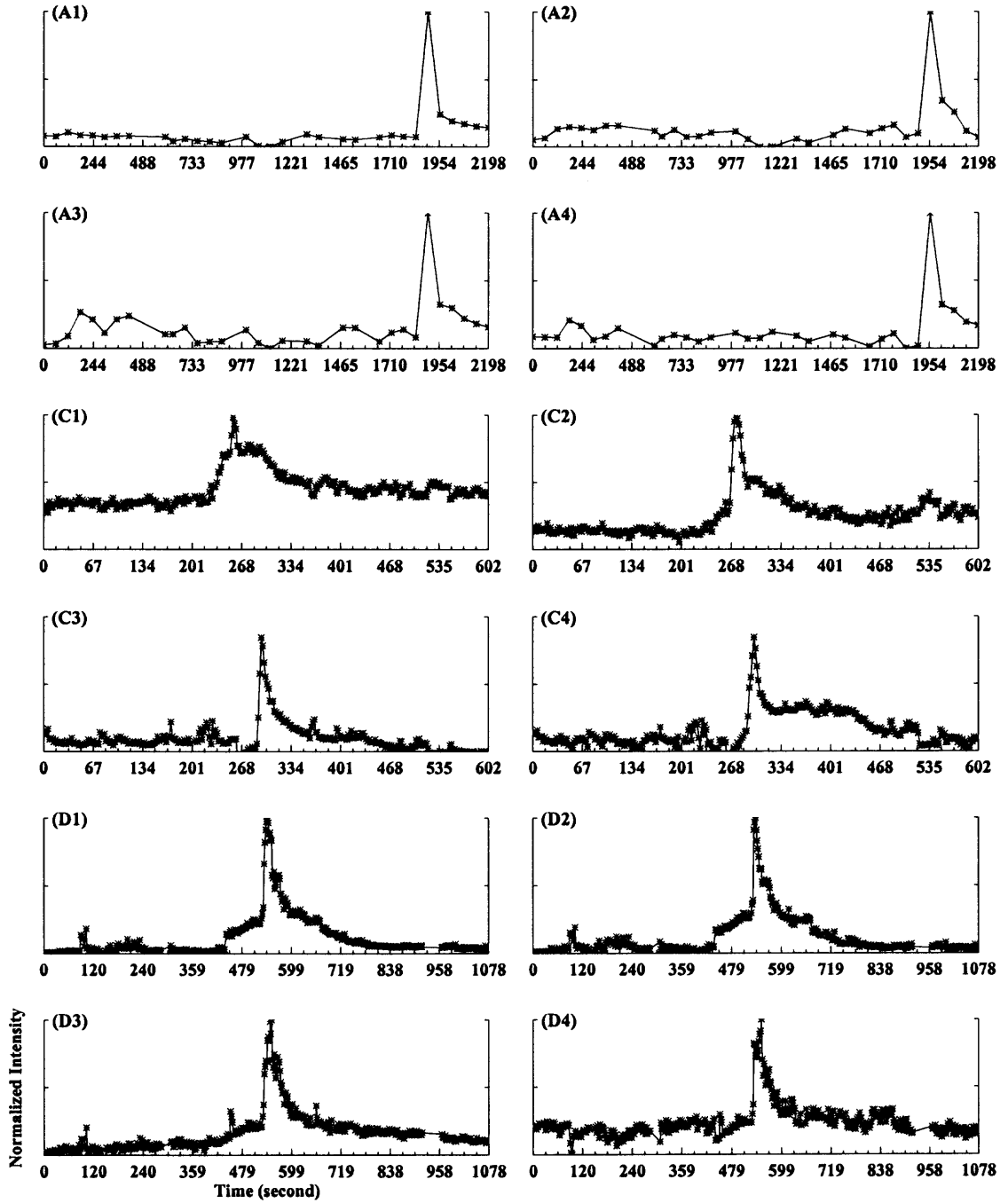


**Figure 2.11** NIR and G-band light-curves of selected regions during flare peaks. (A1) to (A4) shows NIR cooling patterns during the first event, (C1) to (C4) are corresponding G-band curves during the first event and (D1) to (D4) are corresponding NIR in the second event.

The cooling time of the G-band is about 20 s. In the first event, close to the image cadence, the measured NIR cooling time is about two minutes. Therefore, the real value may be less than two minutes. The derived cooling time for the second event is more meaningful due to high cadence. The cooling time is about 30 s. Under the hypothesis that the core emission is coming from a rather deep layer, i.e., the photosphere, this 30 s cooling time is consistent with the value previously calculated by Mein (1966).

## 2.5 Summary and Discussion

In this chapter, multi-wavelength observations of two X-class WLFs are presented. This is the first time NIR continuum contrast were measured, providing new and important clues for understanding flare energetics.

According to standard solar atmospheric models, the opacity minimum is at about  $1.6 \mu\text{m}$ . Therefore, the NIR continuum should originate from the deepest layers in the quiet atmosphere, which is about 50 km deeper than the visible continuum (Vernazza et al. 1976; Wang et al. 1998). Based on our observations, the energy budget can not be balanced if only the direct heating model is taken into account (Xu et al. 2004a). The effects of the other two mechanisms, chromospheric back-warming and  $\text{H}^-$  emission, are necessary to explain the NIR and visible continuum emissions. Since ionization and recombination can occur very quickly, we can not distinguish the heating components caused by different mechanisms by studying the morphology of flares alone. On the other hand, chromospheric back-warming and  $\text{H}^-$  emission models were used to explain relatively weak flares (Abouadarham & Hènoux 1986, 1987, 1989; Ding 2003a; Ding et al. 2003b; Machado et al. 1989; Metcalf et al. 1990b) with contrast enhancements similar to the halo structures in our observations. Note that the light-curve of the total NIR emission reached its peak later than the light-curves of core areas and HXR, indicating two components of the flare heating. In addition, according to Hènoux et al. (1990); Liu et al. (2001); and Neidig et al. (1993a), the delay is caused by a heating process of the photosphere and TMR via chromospheric recombination. In this

case, the direct heating for the core areas is more reasonable. We conclude this because in these two events, (1) the HXR with energies up to 800 keV were correlated with NIR and visible continua, (2) the core areas were much smaller than halo areas and (3) the duration was less than two minutes from the MLC in Figure 2.6. Therefore, if the direct heating only responds to the cores, the input energy by electrons with extreme high energy may have had a chance to balance the output of NIR core emission. In addition, by comparing the HXR in two events, it is reasonable to anticipate higher electron flux with higher energy in the second event compared to the first one. Apparently, the larger the electron flux, the brighter the flare and the shorter the delay.

On the other hand, the opacity during the flare must have changed due to the increasing electron population. Therefore, the NIR emission originated higher than the photosphere or in the chromosphere as Ohki & Hudson (1975) predicted. However, it is beyond the scope of the paper to derive the opacity change during these two flares.

As discussed above, it is reasonable to expect that all three mechanisms, including chromosphere back-warming,  $H^-$  emission and electron heating are contributing to the white-light emissions. For the weakest WLF, the major part of the electron flux can only reach the chromosphere. Then, the chromospheric components (back warming) will dominate the white-light emission and the contrast enhancement in photosphere is not significant. If an event is stronger, more energetic electrons are accelerated. Thus,  $H^-$  emission and electron heating of the photosphere will be the main source of the continuum enhancement. In an extreme energetic event, the photosphere can even be efficiently heated by electron beams directly. Therefore, the core-halo structure would exhibit more distinct character in extreme energetic events. NIR observations of weaker flares which may only have "halo" structures would establish a lower limit for photosphere heating and are consequently a good test to validate our predictions.

## CHAPTER 3

### PROPERTIES OF FINE MAGNETIC STRUCTURES

#### 3.1 Abstract

In this chapter, the physics scope has been changed from solar flares to the investigations of the smallest magnetic structures on the solar disk. Several observations have been carried out regarding this aspect. The data collection still focuses on the photospheric emission in the NIR at  $1.56 \mu m$  and visible light.

In the year of 1999, active region NOAA 8515 was followed from April 19 to 27, as it crossed the solar disk. The NIR continuum images at  $1.6 \mu m$  were obtained at BBSO with an Indium Gallium Arsenide (In Ga As) NIR digital camera. The high-resolution longitudinal magnetograms and visible light filtergrams at  $6103 \text{ \AA}$  with the specially designed Digital Vector Magnetograph (DVMG) were collected simultaneously. No so-called “dark faculae” was identified from this observation. In addition, a threshold magnetic flux density that separates the dark pores from bright faculae was determined.

With the recent great improvement of instruments and observing technique, high quality data with diffraction limit resolution and “seeing-free” is able to be obtained. High-resolution images in the visible and in the NIR continuum around  $1560 \text{ nm}$  were obtained of solar active regions NOAA 10707 and 10486 with the DST at NSO/SP on 2004 December 1, 2 and 2003 October 29. The images were taken with the HOAO System and the spatial resolution was close to the diffraction limit of the  $76 \text{ cm}$  aperture DST in both wavelengths. For the 2004 December run, the NIR observations were made with a newly developed Lyot filter system, which was designed at the Center for Solar-Terrestrial Research (CSTR)/New Jersey Institute of Technology (NJIT). The filter has a bandpass of  $2.5 \text{ \AA}$  which allows us to observe the pure NIR continuum at the opacity minimum. Our data shows that all dark features in the NIR are also dark in the visible light. There is no evidence showing the

existence of so-called dark “faculae”, i.e., faculae that have negative contrasts in the NIR but positive contrasts in the visible. This result is consistent with the previous study. The negative peak contrast of these small pores are about 50% in the visible and 25% in the NIR, and their dimensions are in the range of 1'' to 4''.

### 3.2 Introduction

Faculae are small-scale brightenings in the photosphere of the Sun, which are usually associated with chromospheric plages. It is generally believed that these photospheric bright points are related to small-scale magnetic features and more than 90% of the magnetic flux outside sunspots is concentrated in small tubes (Keller 1992; Zhang et al. 1998). Although faculae are much smaller than dark magnetic structures, such as sunspots and pores, their brightness excess and large population can compensate the dimming of sunspots and pores during solar maximum. Therefore, faculae contribute to the observed variation in the solar irradiance over the 11-year cycle (Schatten 1988; Kuhn et al. 1988; Walton et al. 2003). They are also related to variations on shorter time scales (Fligge et al. 2000).

It is important to understand the physical reason why faculae appear brighter than the quiet sun background. Much work has been done both in observations and theory, to determine the contribution of facular points to solar irradiance variation. Several competing flux-tube models try to explain the structure of faculae. The “hot wall” model (Spruit 1976) considers faculae as small flux-tubes with diameters of about 100 km. When observed near the center of the solar disk, one can see deep into the photosphere due to the low opacity of the photospheric material inside the flux-tube. The vertical, hot, bright walls are not visible. Therefore, the contrast of the faculae will be very low when observed at this location. When observed at moderate heliocentric angles ( $> 60^\circ$ ) the hot wall of the faculae, which is brighter than the average photosphere near the faculae, becomes visible and the contrast increases. When observed at extreme heliocentric angles ( $> 80^\circ$ ), the side of the flux-tube that is closer to the center of the solar disk blocks the visible hot wall and the contrast

decreases. The second model, which attempts to explain faculae is the “hot cloud” model (Chapman 1979). This model assumes that faculae are formed by magnetic heating. The contrast of the faculae would monotonously increase as the faculae moves from disk center to the solar limb and the apparent thickness of the hot cloud increases due to the apparent geometry change. The third model is the “hillock ” model (Schatten et al. 1986), which is very similar to the hot cloud model, where faculae are hot plasma emitted by flux-tubes around sunspots. Observation in the near-infrared (NIR) can provide additional clues about the structure of faculae, because the opacity minimum of the solar atmosphere is at  $1.6 \mu\text{m}$ . Several authors have already studied the characteristics of faculae with NIR observations (Foukal et al. 1989, 1990; Moran et al. 1992; Foukal & Moran 1994; Wang & Zirin 1987; Wang et al. 1998). Thus far, most observations favor the hot wall model. Recently, Keller et al. (2004) presented their numerical MHD simulations of facular points close to the limb. They showed that the facular brightenings were caused by viewing perspective along the edges of granules. Their simulations support the “hot wall ” model too.

NIR observations provide crucial information for the diagnosis of faculae because the opacity reaches its minimum at around  $1.6 \mu\text{m}$  due to  $\text{H}^-$  absorption. We are able to probe the deepest layer of solar atmosphere and therefore have additional constraints for the faculae models. The first NIR observations of faculae were obtained by Worden (1975). Since then, a great number of observations have been carried out (Elste 1985; Foukal et al. 1989, 1990; Moran et al. 1992; Wang et al. 1998; Sobotka et al. 2000; Xu et al. 2004b). Foukal et al. (1989) first announced their discovery that faculae are dark in the NIR but bright at  $\text{Ca K} + 0.38 \text{ \AA}$  and slightly brighter in white-light around disk center ( $\mu \geq 0.75$ ). When facular points are observed close the limb, their contrasts in the NIR becomes positive. Subsequently, Foukal et al. published several papers discussing their observations of dark faculae (Foukal et al. 1989, 1990). They argue that a layer of hot plasma above those small flux tubes is optically thick in the visible but optically thin in the NIR (see Figure 3.1. This is the reason why “dark faculae” have positive contrasts in the

visible and negative contrasts in the NIR around disk center. Their results support the “hot wall ” model, where the magnetic field inhibits the convection. On the other hand, their explanation of facular brightness near the disk center is closer to the “hot cloud” model. Faculae images in the NIR with spatial resolution as high as  $0.6''$  were obtained by Wang et al. (1998). Within these images, only four pairs of elements out of 150 showed opposite contrasts in the NIR and visible. Their results also favor the “hot wall ” model except that the dark features in the NIR can be classified as small pores, thus the “hot cloud” model can not be fully ruled out.

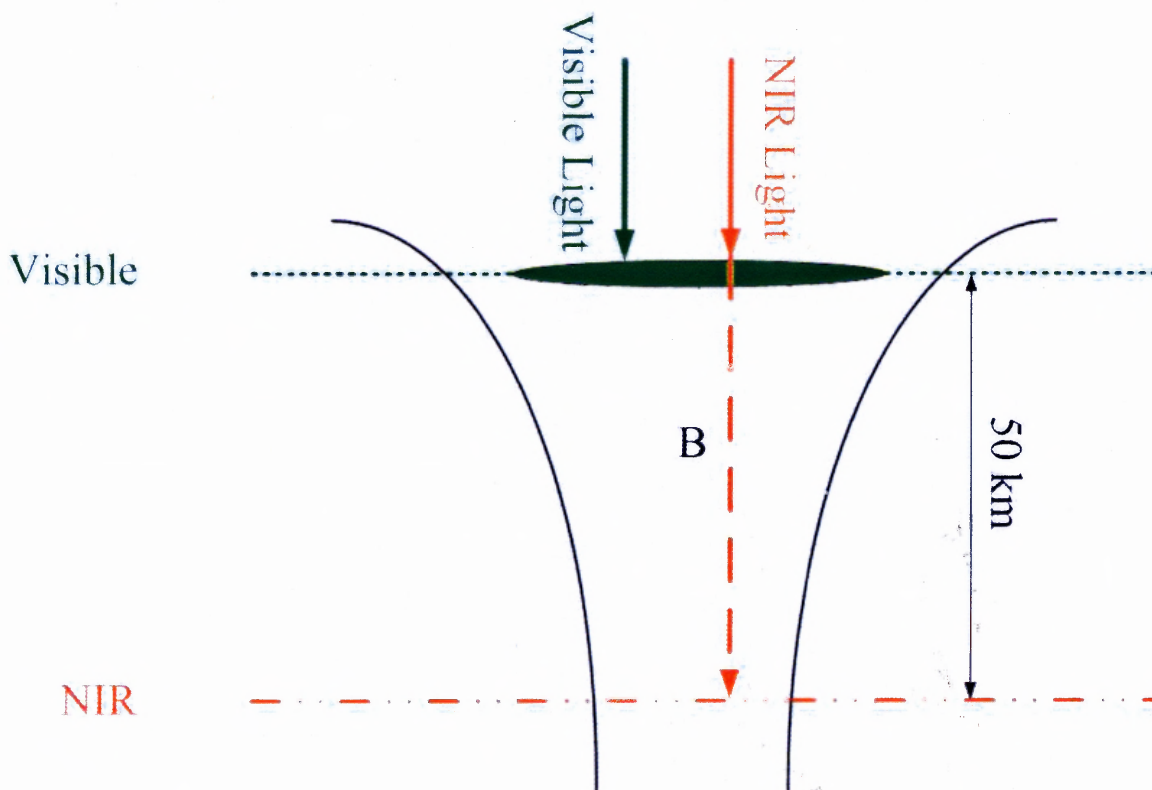


**Figure 3.1** Diagram shows the physics why dark faculae are dark.

### 3.3 First Approach of Searching Dark Faculae

#### 3.3.1 Observation

We observed active region NOAA 8518 at BBSO as it crossed the solar disk from April 19 to 27, 1999. It was a simple, decaying  $\alpha$ -sunspot without much activity. The NIR image series are shown in Figure 3.2. We can see some basic properties of this active region in these pictures: the pores in east of the sunspots gradually disappear. The images taken on April 20 and 21 are closer to the disk center than others. Figure 3.3 shows the continuous MDI magnetograms of the active region from April 19 to 27, 1999. A compiled movie shows that many small flux-tubes of opposite polarity are cancelling each other locally.

Two types of time sequences were obtained during the observation. The DVMG system at the 25 cm vacuum refractor obtained longitudinal magnetograms and intensity maps while the In Ga As camera obtained NIR filtergrams at the 65 cm vacuum reflector. The DVMG system uses two nematic liquid crystal variable retarders and the retardance can be changed by means of an applied voltage to select the desired polarization state. A ferroelectric liquid crystal is used as a  $1/2 \lambda$  plate and its fast axis can be rotated by means of an applied voltage. The ferroelectric crystal is used along with a fixed linear polarizer to select either the Stokes-(I+V) or Stokes-(I-V) component of the magnetic field. The observations are performed in the wing of the magnetically sensitive Ca I absorption line at 610.3 nm with a 0.025 nm bandwidth Zeiss filter. A  $1024 \times 1024$  pixel CCD camera manufactured Silicon Mountain Design is used in the  $2 \times 2$  binning mode, which yields an image scale of  $0.6'' \text{ pixel}^{-1}$ . For this study, only longitudinal magnetograms were obtained (Stokes-V/I). We used Kitt Peak full disk magnetogram to determine the calibration function  $C(\rho)$ , which converts the degree of polarization  $\rho$  into magnetic flux measured in Gauss. The calibration procedure is given in Table 3.1. The result is 1% polarization  $\approx 230$  Gauss. for each degree of polarization. An example of a magnetogram is shown in Figure 3.5 c. A frame selected, short-exposure image in the line wing of the Ca I 610.3 nm absorption line is defined as the “white-light” image. Since the Ca I line is rather weak, we

use this line wing image as a proxy of the continuum (higher origin in the photosphere). An example of the white light image is shown in Figure 3.5 b. The NIR SU320-1.7RT In Ga As camera (see Figure 3.4) was bought from Sensors unlimited, INC in 1997. The dark current is controlled low enough to take photos at the room temperature without any additional cooling system. It has a sensitivity range from  $0.9 \mu\text{m}$  to  $1.7 \mu\text{m}$  with a quantum efficiency greater than 75% from  $1.0 \mu\text{m}$  to  $1.6 \mu\text{m}$ . The detector has a  $320 \times 240$  pixel FPA containing an In Ga As photodiode array integrated to a silicon readout multiplexer using indium bump-bonding technique. Detailed sensor specifications are listed in Table 3.2. The optics were set up to produce an image scale of  $0.3'' \text{ pixel}^{-1}$  (see Figure 3.6 for the detailed setup information.). A custom made interference filter centered at  $1.56 \mu\text{m}$  with a pass band of 4 nm, was used to select the wavelength range. The exposure time was 0.1 ms. Image (a) in Figure 3.5 shows an example of an NIR image after dark and flat field frame correction.

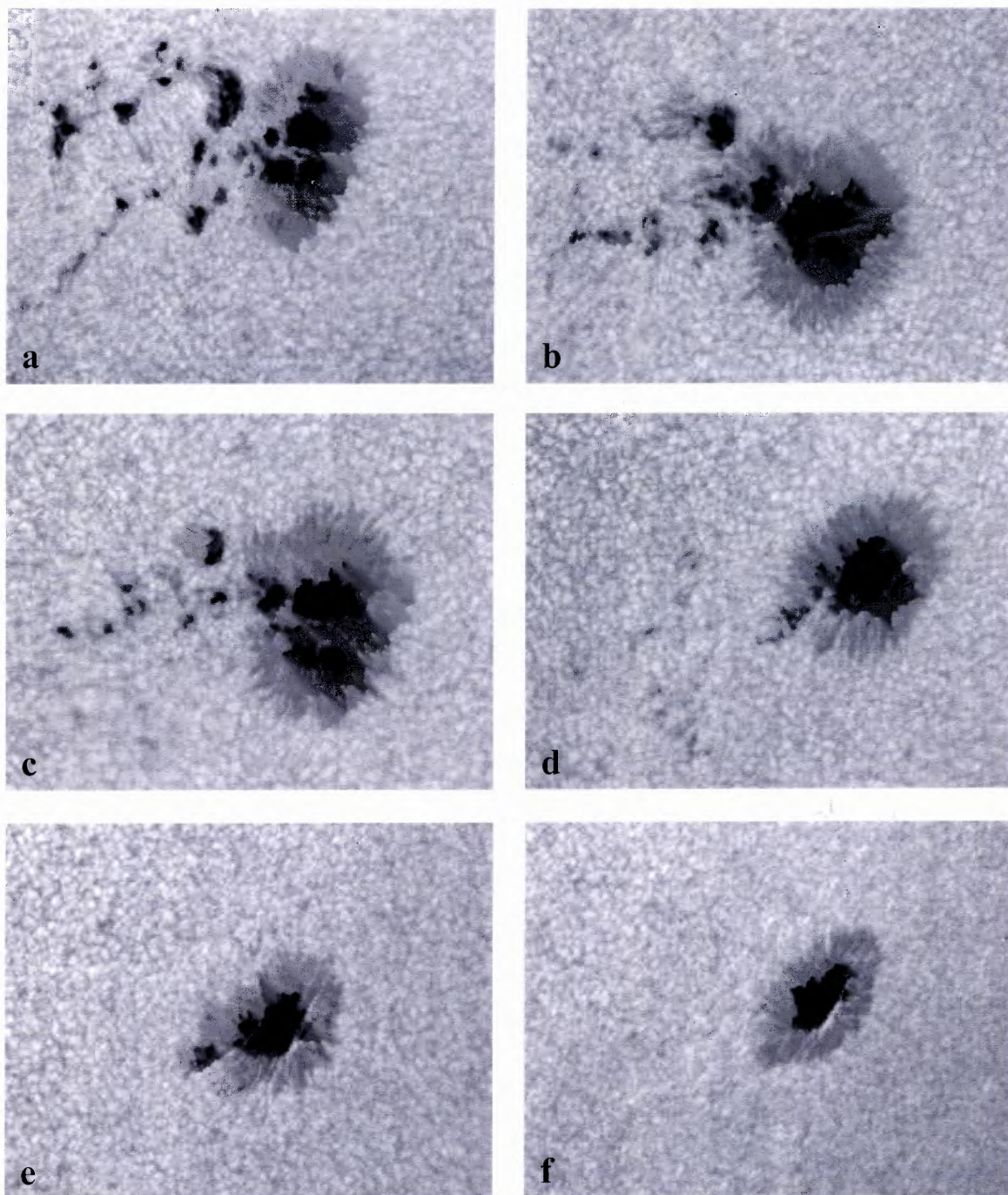


**Figure 3.2** NIR images of active region NOAA 8518 observed on April, 1999. (a) April 19, (b) April 20, (c) April 21, (d) April 25, (e) April 26, and (f) April 27.

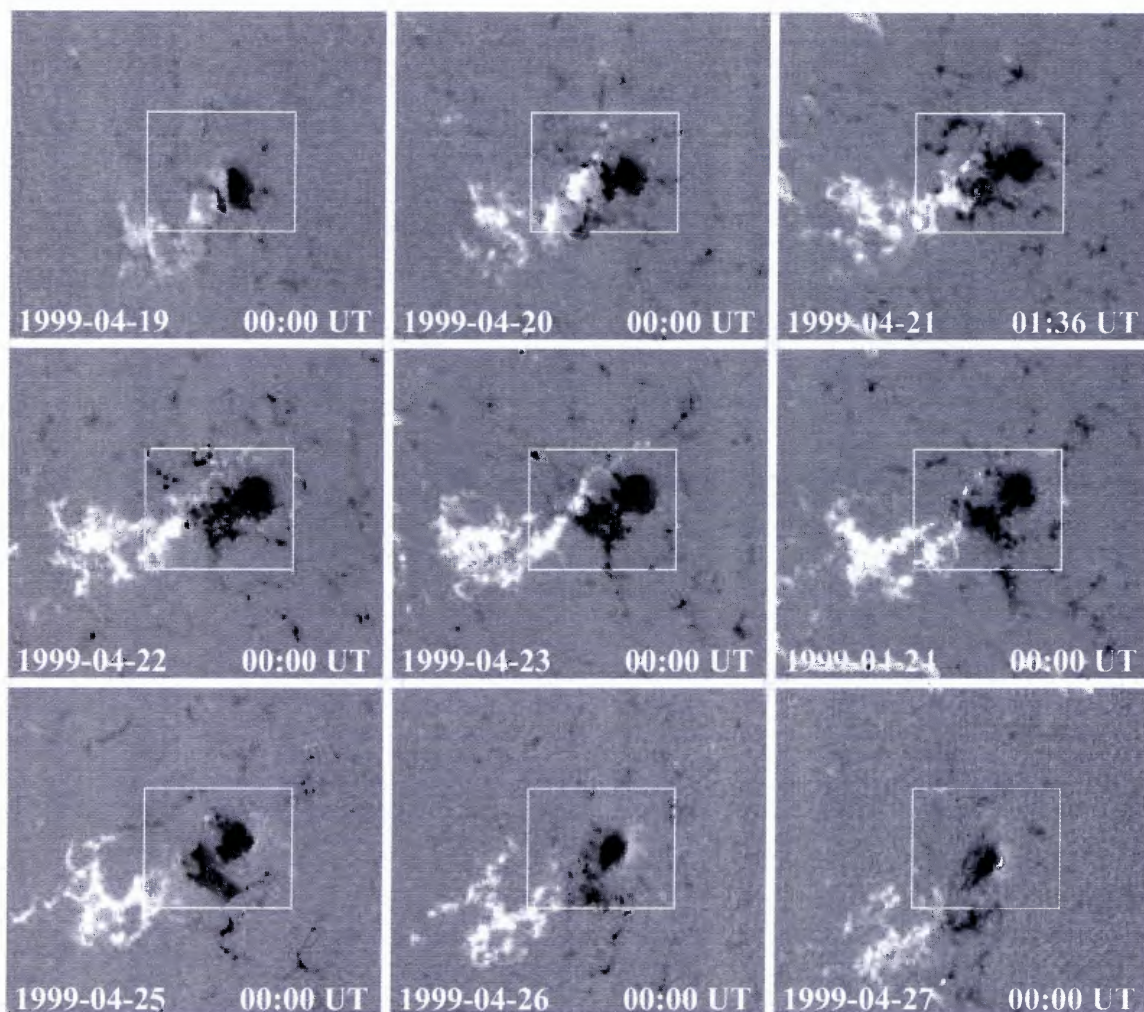


**Figure 3.3** MDI magnetograms taken from April 19 to 27, 1999. The white box shows the similar FOV of IR images in Figure 3.3. The magnetograms were scaled between  $-400$  G and  $+250$  G.



**Figure 3.4** The NIR In Ga As camera. (From the web site of Sensors unlimited, INC)

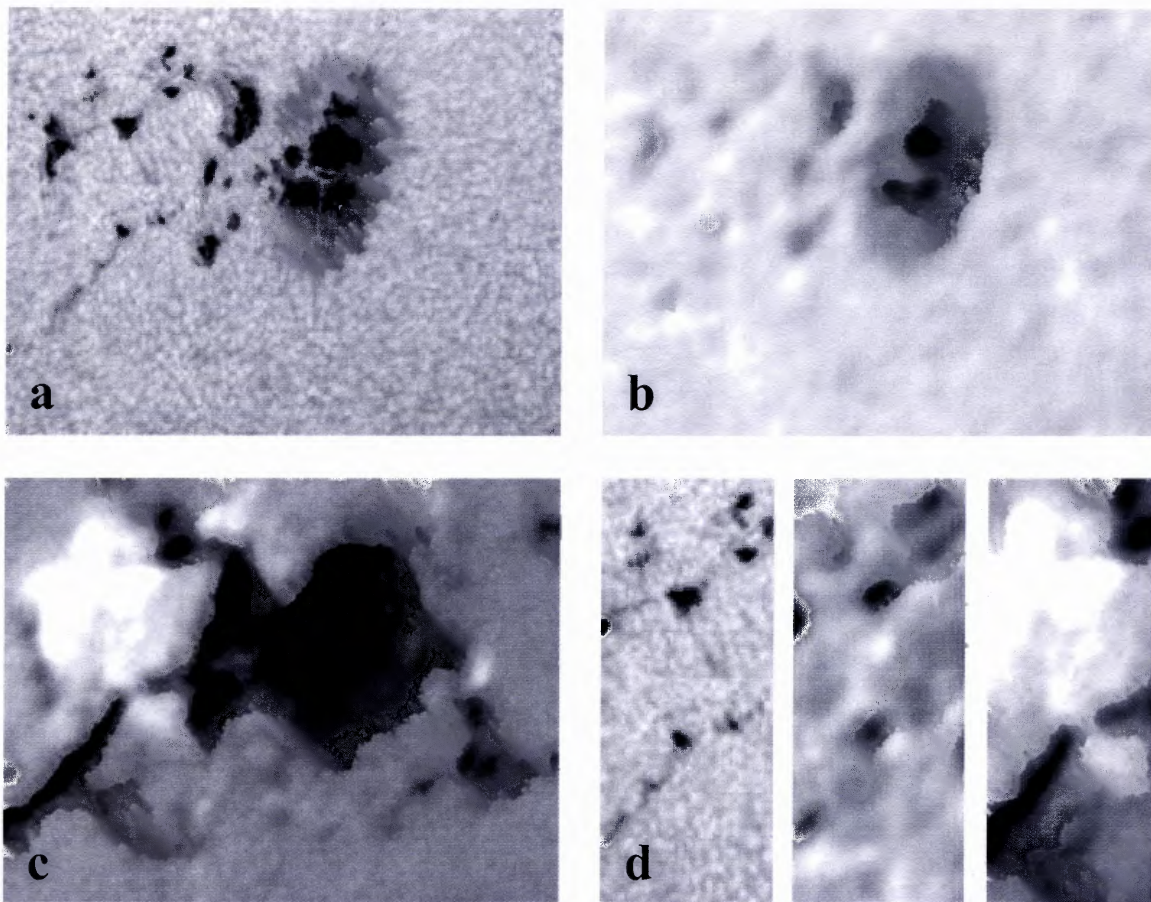


**Figure 3.5** Images of active region NOAA 8518 at different wavelengths observed on April 19, 1999. (a) NIR filtergram, (b) visible light filtergram, (c) magnetogram, and (d) sub-frames from (a), (b), and (c) depicting the region of interest. The magnetograms were scaled between  $-400$  G and  $+250$  G.

### 3.3.2 Data Analysis and Result

In this analysis, we present data from April 19, 20, and 25, 1999, which were obtained during best seeing conditions among all observing days. Due to the fact that the FOV of the NIR camera was much smaller than that of the visible-light camera, we needed to align the images and restrict the data analysis to the common FOV. In addition, the image scales had to be matched by re-sampling the “low resolution” magnetogram and white-light data to the image scale of the NIR observations. The NIR filtergram, white light image, and magnetogram of this region can be seen in Figure 3.5d. We selected this particular region

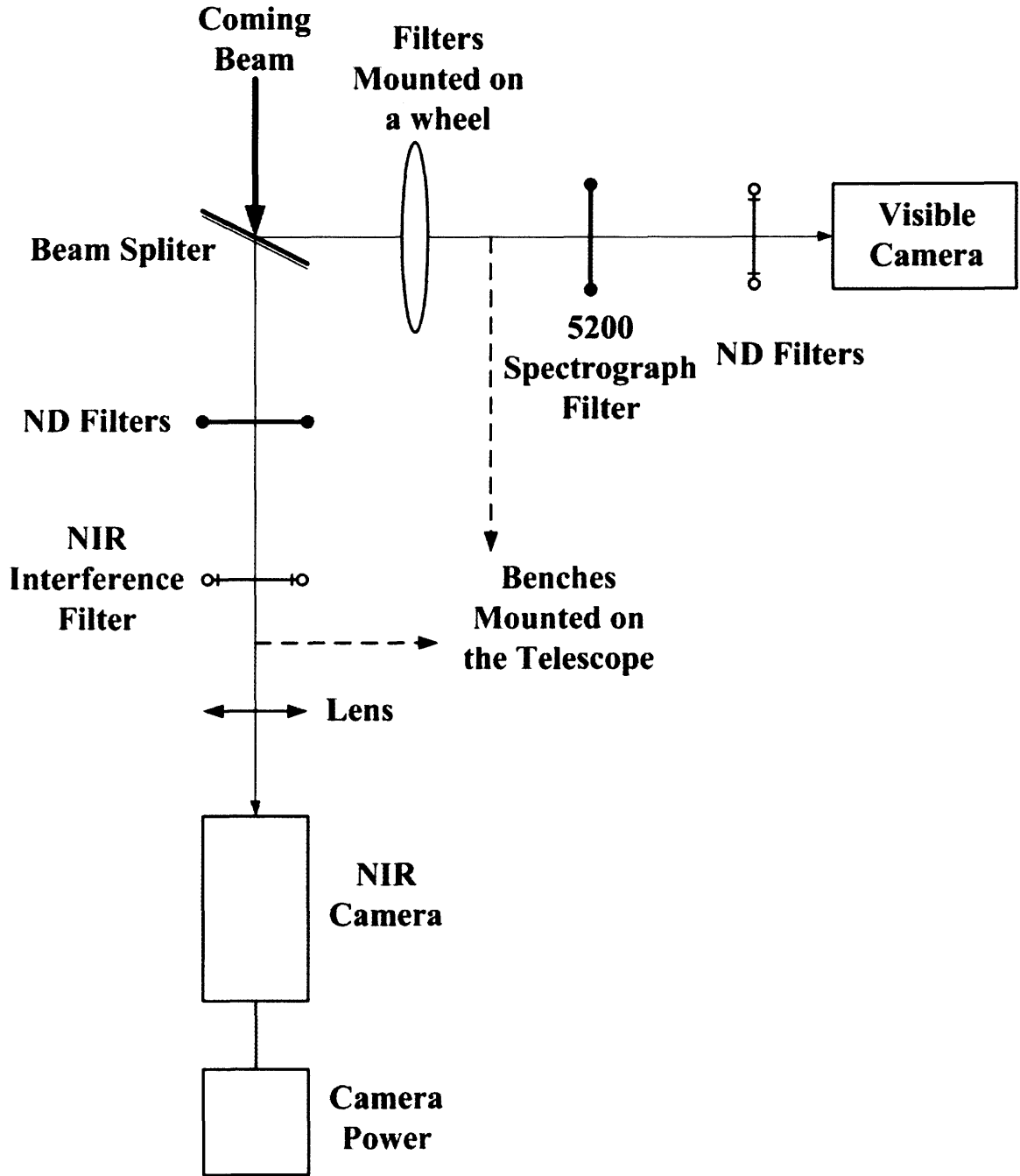


Figure 3.6 Diagram of the setup for the April, 1999 observing run at BBSO.

**Table 3.1:** Calibration Coefficients.

Date	Kitt Peak Time (UT)	BBSO Time (UT)	Calibration Function
April 18, 1999	15:09:14	17:18:35	$C = 19800 \times \rho$
April 20, 1999	16:29:14	16:29:05	$C = 22200 \times \rho$
April 25, 1999	16:28:35	16:28:43	$C = 27200 \times \rho$
April 26, 1999	18:38:27	18:41:20	$C = 22000 \times \rho$
April 27, 1999	14:59:53	15:15:14	$C = 25400 \times \rho$

**Table 3.2:** Sensor Specifications of the NIR SU320-1.7RT In Ga As Camera.

Format		320 × 240
Pitch		40 μm
Optical Fill Factor		100%
Spectral Response		0.9 μm to 1.7 μm
Exposure Mode		ripple
Quantum Efficiency		> 65% over 1.0 μm to 1.7 μm
Mean Detectivity, $D^*(\lambda_{pk})^1$		$10^{12} \text{ cm} \cdot \sqrt{\text{Hz}/\text{W}}$
Uniformity		> 98%
Full Well Capacity		> 10 million electrons
Digitization		12 bit
Electronic Readout Noise		2000 equivalent photoelectrons
Pixel Rate		6.1 MHz
FPA Temperature		18°C
Lens Mount		U- and C-mount
Exposure Times		127 μsec to 16.3 msec in 8 steps
Frame Rate		60 Hz
Image Display	Frame Grabber Board and Video Monitor	

Note. — The information is provided by Sensors unlimited, INC.

because it avoids the main sunspot but still contains strong plage features.

### *Visible Contrast as a Function of NIR Contrast*

To measure the contrast of faculae in the visible as a function of that in the NIR, we considered an area near NOAA 8518 as shown in Figure 3.5d. We plotted the contrast of the

visible as a function of the contrast in the NIR as scatter plots shown in Figures 3.7a, c, and e for April 19, 20, and 25, 1999, respectively. A positive contrast value means that the object in question is brighter than the mean photospheric intensity in that region while a negative contrast value indicates that the object is darker than the mean photospheric intensity in that region. The correlation between the contrast in the visible and the contrast in the NIR can be seen more clearly in the averaged plots in Figures 3.7b, d, and f. For these plots, we plot the averages of the columns in Figures 3.7a, c, and e. The vertical lines at each point indicate the standard deviation. These plots of the contrast in the visible as a function of contrast in the NIR indicate that if a particular area is dark in the visible, then it is also dark in the NIR. We find no evidence for faculae that are bright in the visible but dark in the NIR at the same time.

In addition, we did the similar analysis as (Sobotka et al. 2000; Cuberes et al. 2002). The difference is that we use the images at  $0.61 \mu\text{m}$  instead of  $0.8 \mu\text{m}$ . Our difference images also show some dark features. But we would like to mention two points. First, under the new definition, if a feature has positive contrast both at  $1.55 \mu\text{m}$  and  $0.61 \mu\text{m}$ , it may be regarded as a dark facular since it would have negative sign in the difference image if the feature in  $1.55 \mu\text{m}$  has a lower contrast than at  $0.6 \mu\text{m}$ . Second, our results show that most of the dark faculae defined by the new method are around pores. This result agrees with (Sobotka et al. 2000) and (Cuberes et al. 2002). But this dark ring can be caused by artifacts, such as the miss-alignment or mis-scaling of images at two wavelengths.

### *Threshold of Magnetic Flux*

We also studied the magnetic properties of NIR features by aligning the visible-light images, NIR filtergrams and Ca I magnetograms, using the same process as for aligning the visible-light images and NIR filtergrams. Due to the limited resolution of the magnetograms, we can only measure the mean magnetic flux density rather than the actual field strength.

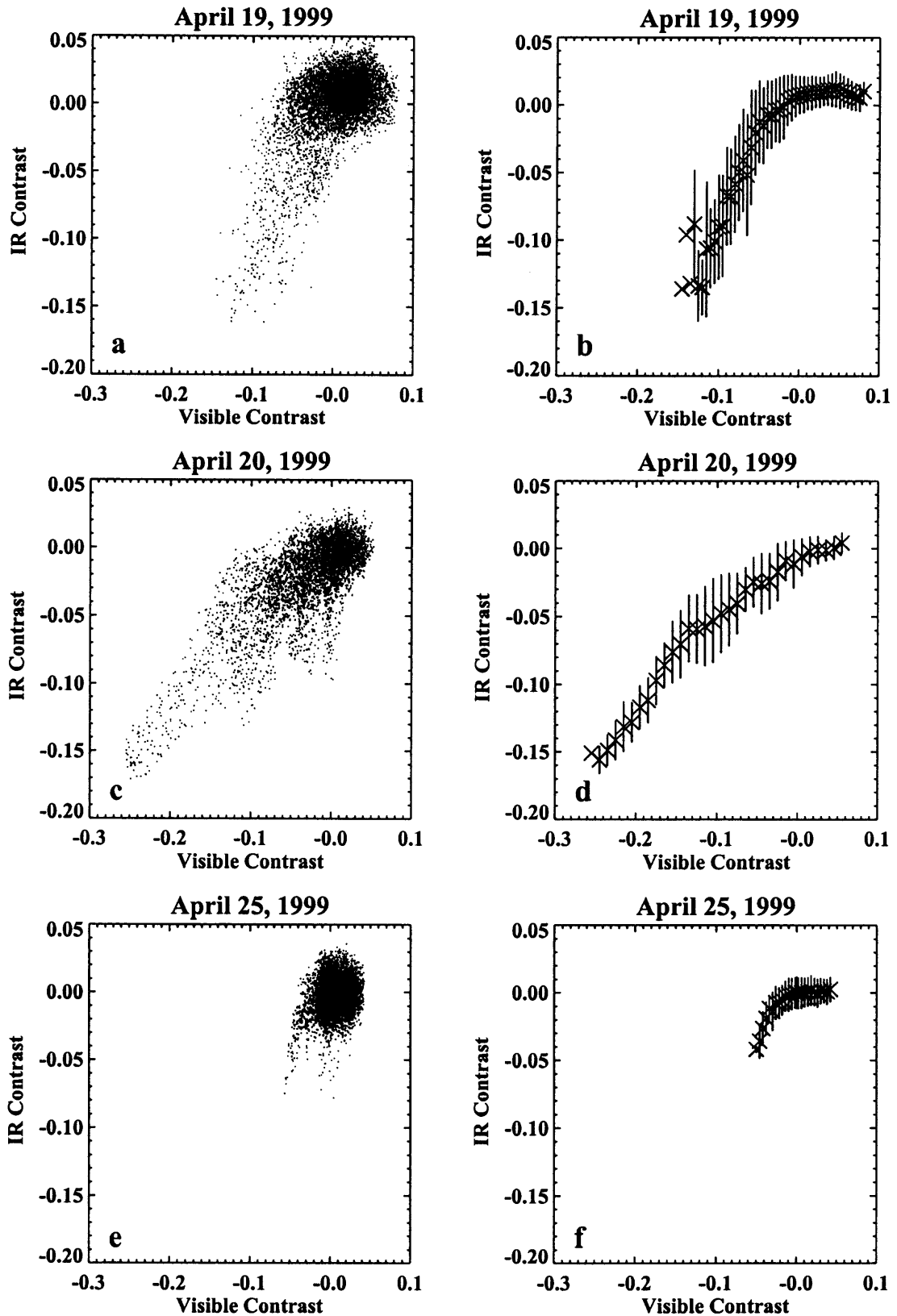


**Figure 3.7** Panels (a), (c), and (e) show scatter plots for the visible contrast as a function of the NIR contrast, and (b), (d), and (f) show plots for the averaged quantities.

We now discuss the threshold of magnetic flux density. We plotted the flux density as a function of the contrast in the NIR, which can be seen in Figures 3.8a, c, and e for April 19, 20, and 25, 1999, respectively. We plotted the flux density as a function of the contrast in the visible in Figures 3.8b, d, and f for the same dates. As can be seen in these plots, each curve can be divided into two sections. The first part of each curve, at the lower flux densities, exhibits a small slope in which the contrast does not change rapidly with increasing flux density. However, there is a region in each plot where, as the magnetic flux density increases, the slope of each curve begins to increase and the contrast changes much more rapidly as the magnetic flux increases. This typically occurs around 200 to 250 G. The two parts of the curve represent different solar features, which exhibit different relationships between contrast and magnetic field.

We fit both parts of each curve separately by a straight line and define the intersection as the “magnetic threshold”, which divides faculae and pores. The threshold values for both the visible and the NIR are shown in Table 3.3. Please note that this quantity is the flux density not true field strength. We can see that the average value for this threshold is approximately 220 G. This value can be translated into a flux per resolution element, which is of the order of  $10^{17}$  Mx. This value agrees with the results of (Moran et al. 1992), (Zirin & Wang 1992), and (Wang et al. 1998). Our results also show that the negative contrast increases with the flux density (Moran et al. 1992).

**Table 3.3:** Magnetic Threshold Values.

Date	$\mu$	NIR	Visible
April 19, 1999	0.74	$220 \pm 20$ G	$210 \pm 20$ G
April 20, 1999	0.82	$210 \pm 20$ G	$190 \pm 20$ G
April 25, 1999	0.85	$230 \pm 20$ G	$230 \pm 20$ G

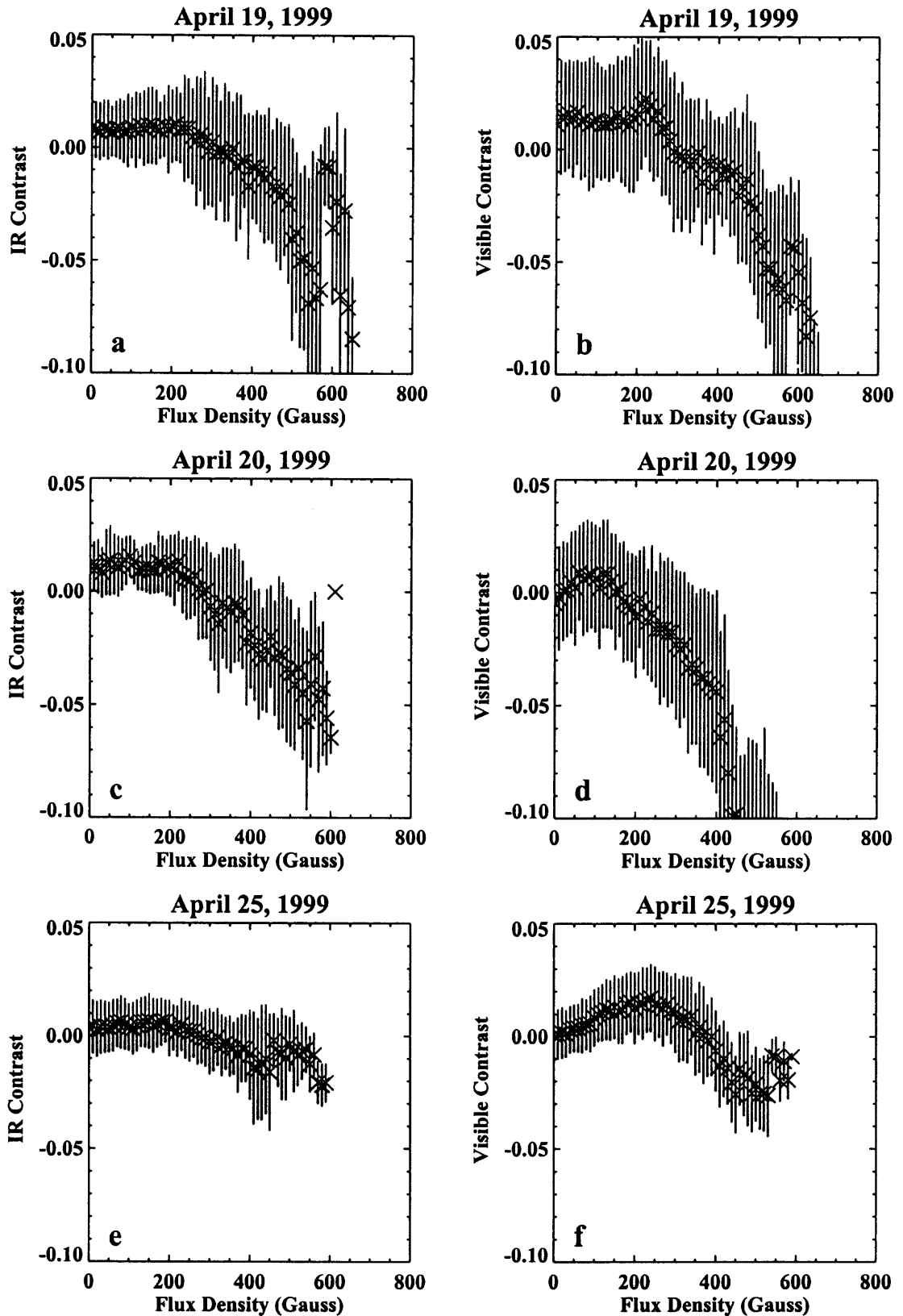


**Figure 3.8** Panels (a), (c), and (e) show plots for the NIR contrast as a function of magnetic flux density, and (b), (d), and (f) show plots for the visible contrast as a function of magnetic flux density.

### 3.3.3 Discussion

Our data show that the contrast of dark features at  $1.56 \mu\text{m}$  is less than the contrast at  $610.3 \text{ nm}$ . This is not surprising for any features following Planck's radiation law. We also find that the contrast of faculae has the same sign in both the visible and NIR. Therefore, there is no evidence shows the existence of dark faculae according to the original definition by Foukal et al. (1989) in our study. We find that what has been previously thought to be dark faculae are actually pores. Our observations were obtained at  $1.56 \mu\text{m}$  whereas Foukal used  $1.63 \mu\text{m}$ . However, such a difference in wavelength should not be the cause for the different results because the height of formation at both wavelengths differs by less than 5 km, which is insignificant (Wang et al. 1998). We believe that the different results arise due to the fact that Foukal was actually observing unresolved pores which were being mistaken for dark faculae. In addition, the dark faculae defined by Sobotka and Cuberes are not same as dark faculae in Foukal's original definition. Another result that we find is the threshold of magnetic flux density, which divides faculae and pores. Our data show that this value is between 200 and 250 G.

## 3.4 Second Approach of Searching Dark Faculae Using the Newly Developed Narrow Bandpass Lyot Filter

### 3.4.1 Observation

In this section, I present the very first images of pure  $1.56 \mu\text{m}$  continuum with diffraction limit resolution obtained with the DST and compare them with simultaneous obtained white-light images and the line-of-sight magnetograms from SoHO/MDI. The most important instrument of our observations is the newly developed system for NIR photometry, which can collect images in a "line-free" NIR continuum window with a very narrow bandpass of  $0.25 \text{ nm}$  near  $1.56 \mu\text{m}$ . An additional data set in the NIR with a relative wide bandpass of  $5 \text{ nm}$  is presented as well in order to compare with previous studies. Therefore,

a total of three data sets of NIR and visible continua from two separated observing runs are presented:

Active region NOAA 10707 was followed from 2004 December 1 to 7 when it moved from solar disk center to the west limb. The NIR photometry system includes a liquid nitrogen cooled Hg Cd Te/Al<sub>2</sub>O<sub>3</sub> Complementary Metal-Oxide Semiconductor (CMOS) camera with 1024 × 1024 pixels and 14-bit digitization depth (Cao et al. 2005a), an IR turnable Birefringent filter (Denker et al. 2003; Wang et al. 2001) which has a bandpass of 0.25 nm designed by CSTR/NJIT for Big Bear Solar Observatory (BBSO) and an interference filter with a 5 nm bandpass. The final bandpass was in a pure continuum region around 1.56 μm. When polarized light is passed through a birefringent crystal, it will be splitting into ordinary component and extraordinary component. If a birefringent crystal is sandwiched between two parallel polarizers, the output is the interference of the above two components. The transmission can be expressed as the former equation:

$$\tau = \tau_0 \cdot \tau_1 \cdot \tau_2 \cdot \tau_3, \quad (3.1)$$

in which:

$$\tau_0 = \cos^2\left(\frac{\mu d}{2^0 \lambda} \pi + \delta_0\right), \quad (3.2)$$

$$\tau_1 = \cos^2\left(\frac{\mu d}{2^1 \lambda} \pi + \delta_1\right), \quad (3.3)$$

$$\tau_2 = \cos^2\left(\frac{\mu d}{2^2 \lambda} \pi + \delta_2\right), \quad (3.4)$$

$$\tau_3 = \cos^2\left(\frac{\mu d}{2^3 \lambda} \pi + \delta_3\right). \quad (3.5)$$

where d is the thickness of crystal, μ is birefringent index. This plot illustrates the transmission profile. In this design (see Figure 3.9), four stacks of calcite module sandwiched between linear polarizers are combined to acquire ~ 2.5 Å bandpass being shown in Figure 3.10. The nematic liquid crystal variable retarders (LCVR) are attached to each stack

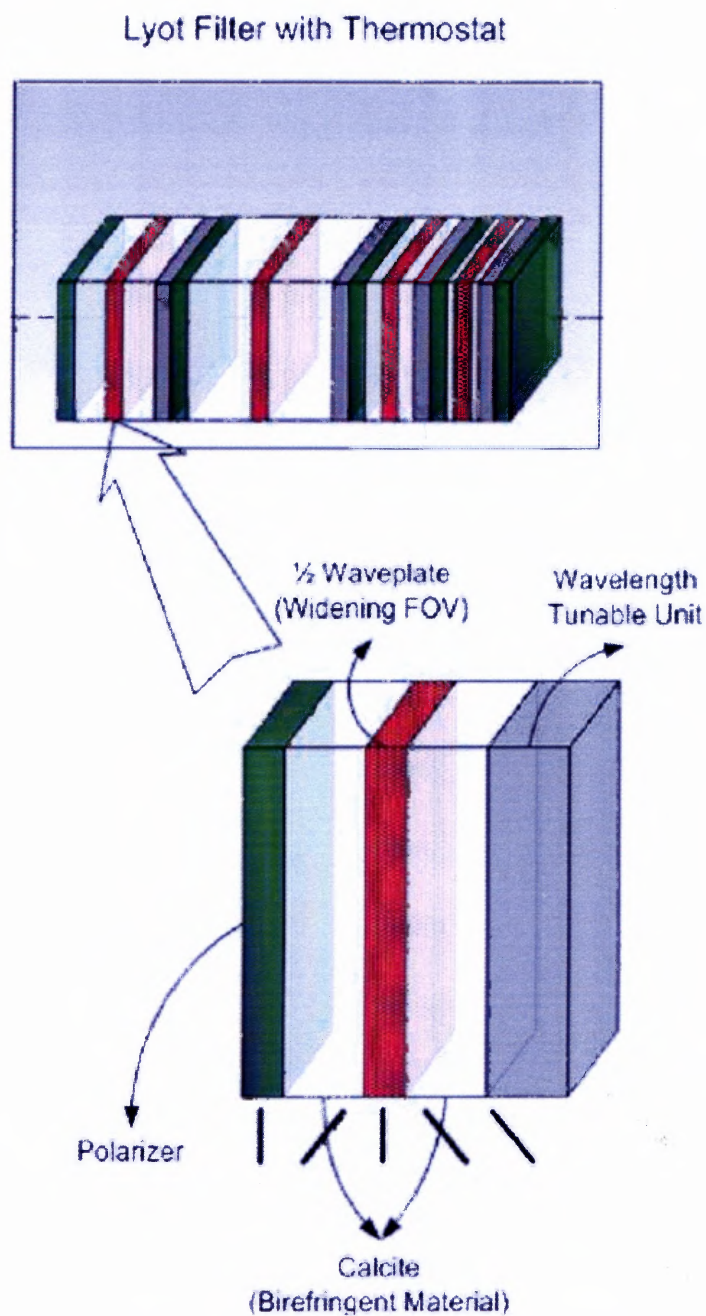


**Figure 3.9** Design of the Birefringent Lyot Filter. See Wang et al. (2001) for details.

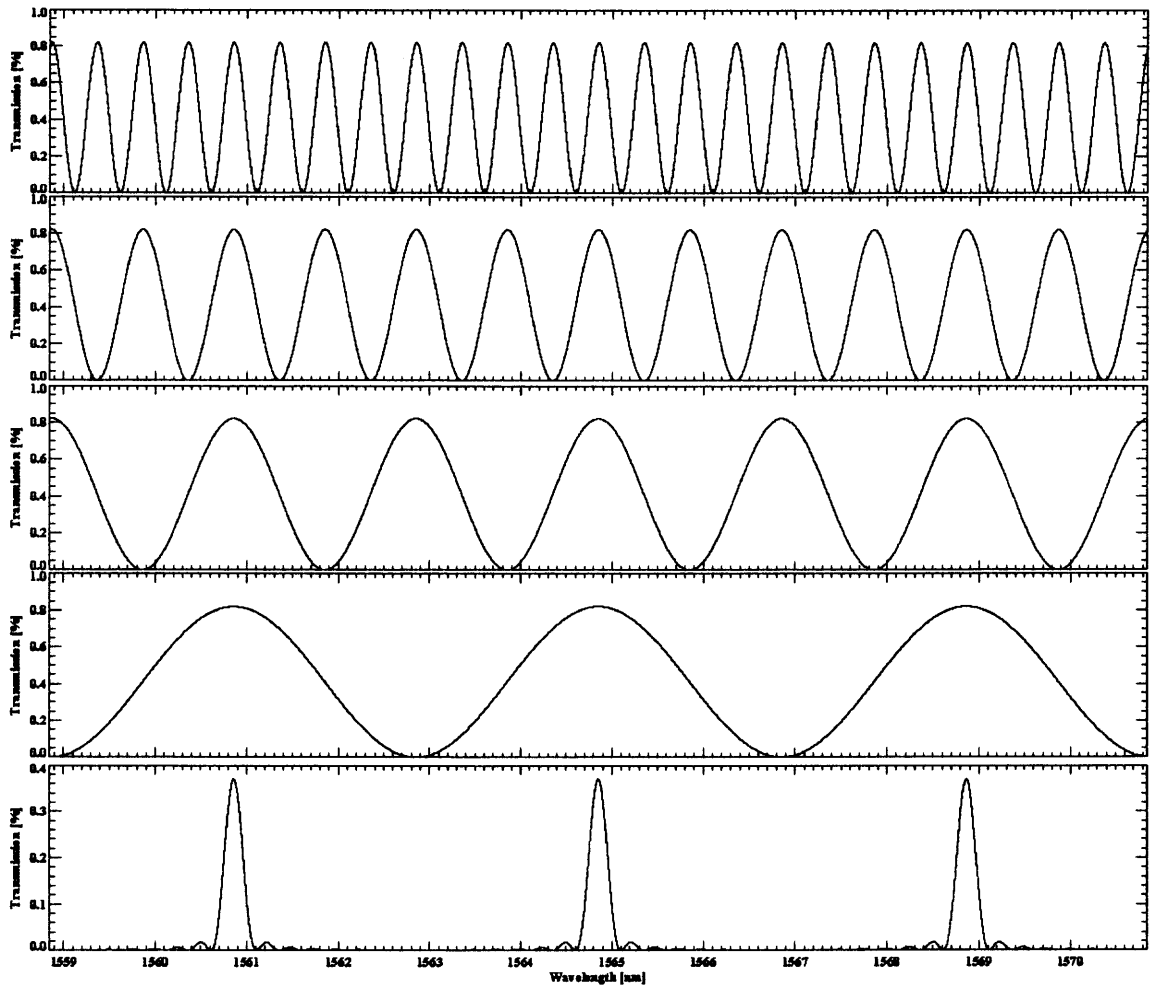


**Figure 3.10** This plot illustrates the transmission profile of each modular and the combination of them. (Cao et al. 2005b)

to tune the bandpass in range of  $\pm 100 \text{ \AA}$ . The calibration and characteristic evaluation have been carried out by using a horizontal spectrograph at the Evan's Facility of NSO, Sacramento Peak. The design requirements are listed in Table 3.4.

**Table 3.4:** Design Requirements of the Lyot Filter System.

Working Wavelength	Fe I 1.5648 & 1.5652 $\mu\text{m}$
Clear Aperture	37 mm
Passband FWHM	2.5 $\text{\AA}$
Tunable Range	$\pm 100 \text{ \AA}$
Peak Transmission	38 % for polarized light 18 % for non-polarized light
Internal Structure	4-module
Thermal Controller	$32.0 \pm 0.1^\circ\text{C}$

The observation in the visible spectrum was carried out simultaneously with the NIR observations. The wavelength range was from 500 nm to 552 nm. The FOV was  $122'' \times 122''$  for the NIR channel and  $105'' \times 105''$  for the visible channel, respectively. Atmospheric turbulence was corrected by the NSO HOAO system (Rimmele 2000; Rimmele et al. 2003). Ten NIR frames were obtained every second and the best one was selected. The frame rate of the visible observation was 0.5 frames per second. A few hours of continuous observations were obtained each day. Examples of two data sets taken on 2004 December 1 (data set I) and December 2 (data set II) are shown in Figure 3.11 and Figure 3.12, respectively. All images are dark and flat field corrected and selected according to the highest rms contrast.

A similar data set (data set III) is included in this paper in order to compare with previous observations and studies. We observed NOAA AR 10486 using the same instruments but without the IR Lyot birefringent filter. At that time, only the interference filter was used resulting a bandpass of 5 nm, which includes a few Fraunhofer lines. These lines contribute about 3% of the overall radiation. The FOV was  $91'' \times 91''$  for the NIR and  $81'' \times 81''$  for the green continuum, respectively. The best data set is shown in Figure 3.13.

Since the FOV of the NIR images, visible images and MDI magnetograms are all

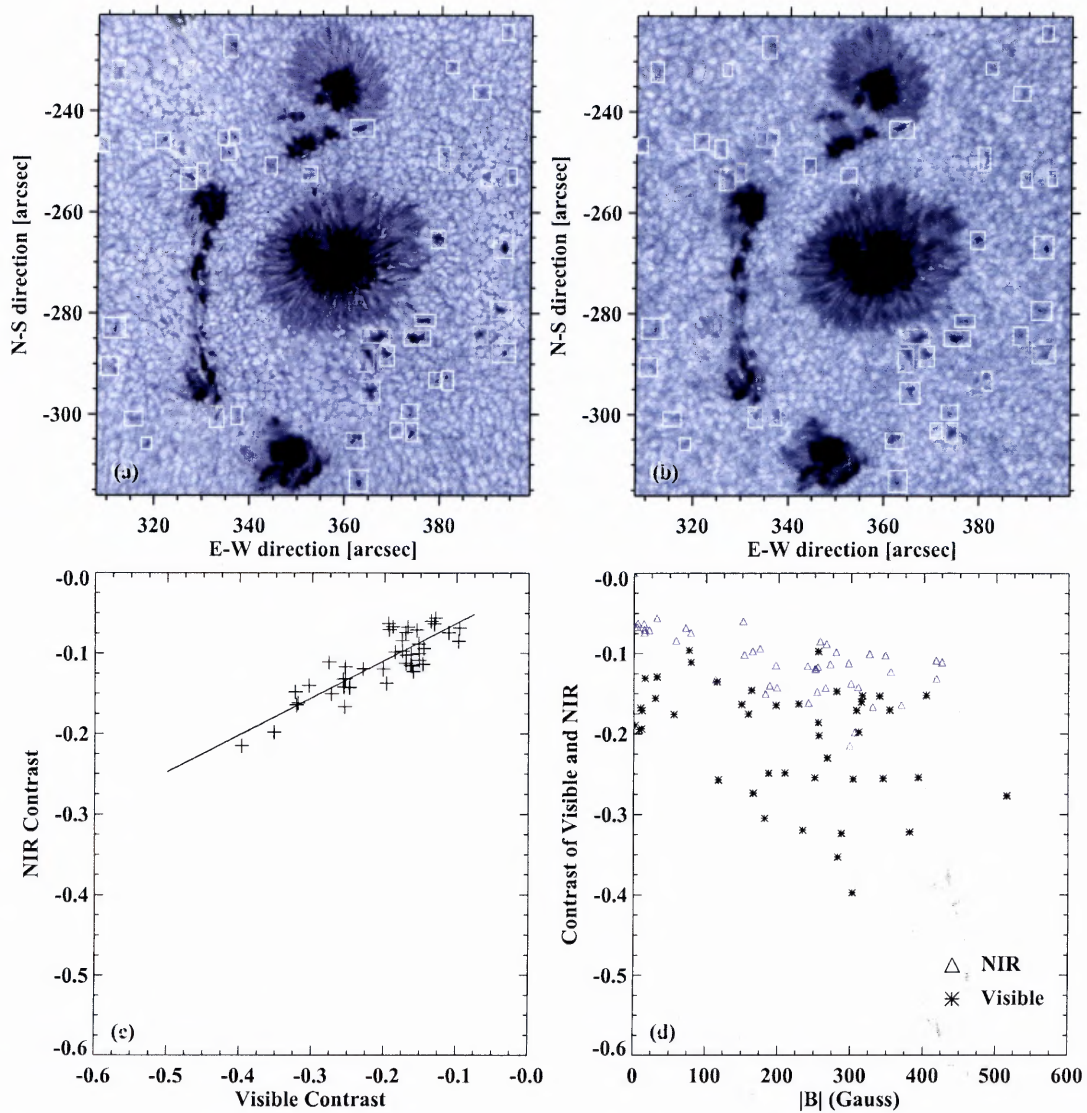


**Figure 3.11** Snapshot of active region NOAA 10707 on 2004 December 1. (a) NIR filtergram at 17:50 UT and (b) Visible light filtergram at 17:49 UT. The two images have the same FOV. Sub-areas marked by white boxes are dark pores selected visually. (c) The lowest contrasts of these small areas in the NIR are plotted as a function of those in visible. The straight line shows the linear fit of this plot. (d) Contrasts versus the absolute value of the corresponding magnetic flux density.

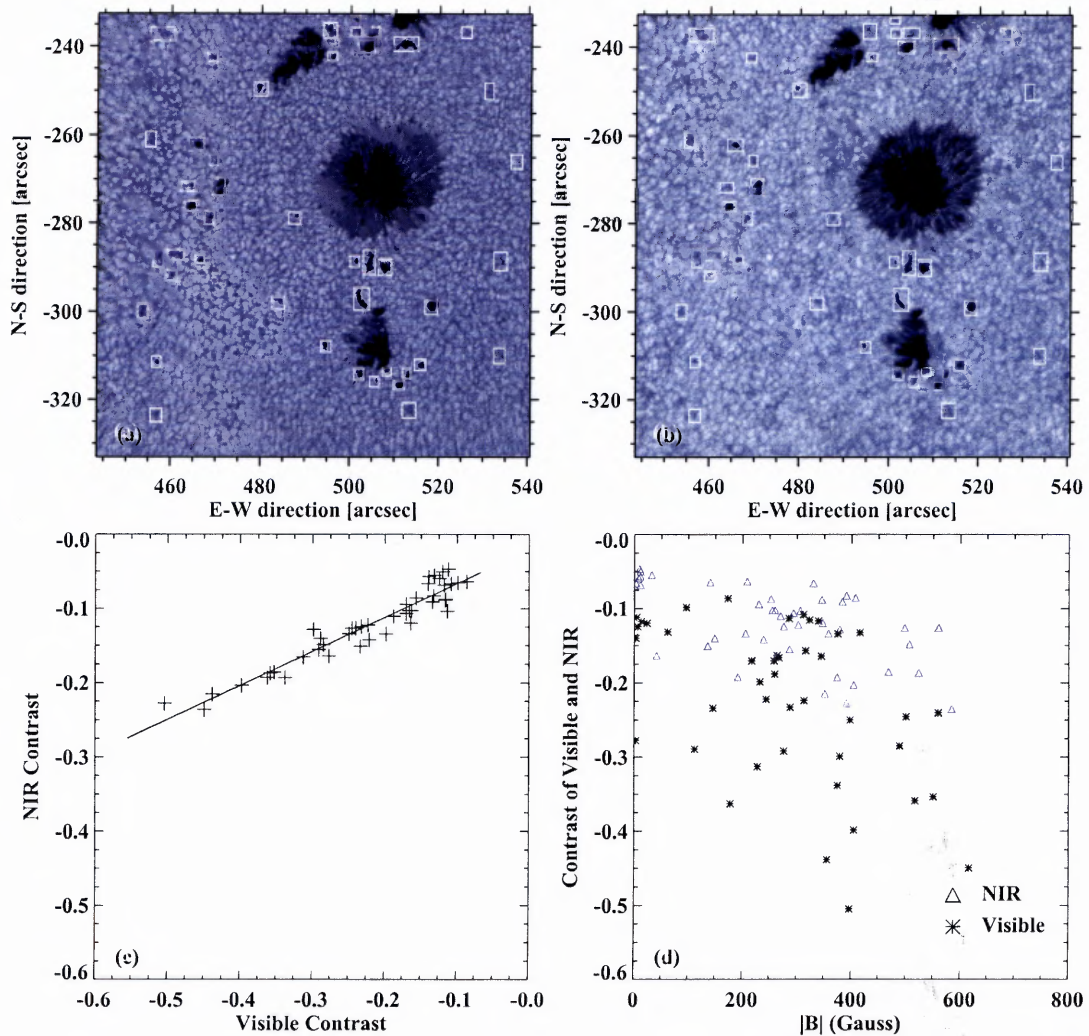


**Figure 3.12** Snapshot of active region NOAA 10707 on 2004 December 2. (a) NIR filtergram at 16:14 UT and (b) Visible light filtergram at 16:14 UT. The two images have the same FOV. Sub-areas marked by white boxes are dark pores selected visually. (c) The lowest contrasts of these small areas in the NIR are plotted as a function of those in visible. The straight line shows the linear fit of this plot. (d) Contrasts versus the absolute value of the corresponding magnetic flux density.

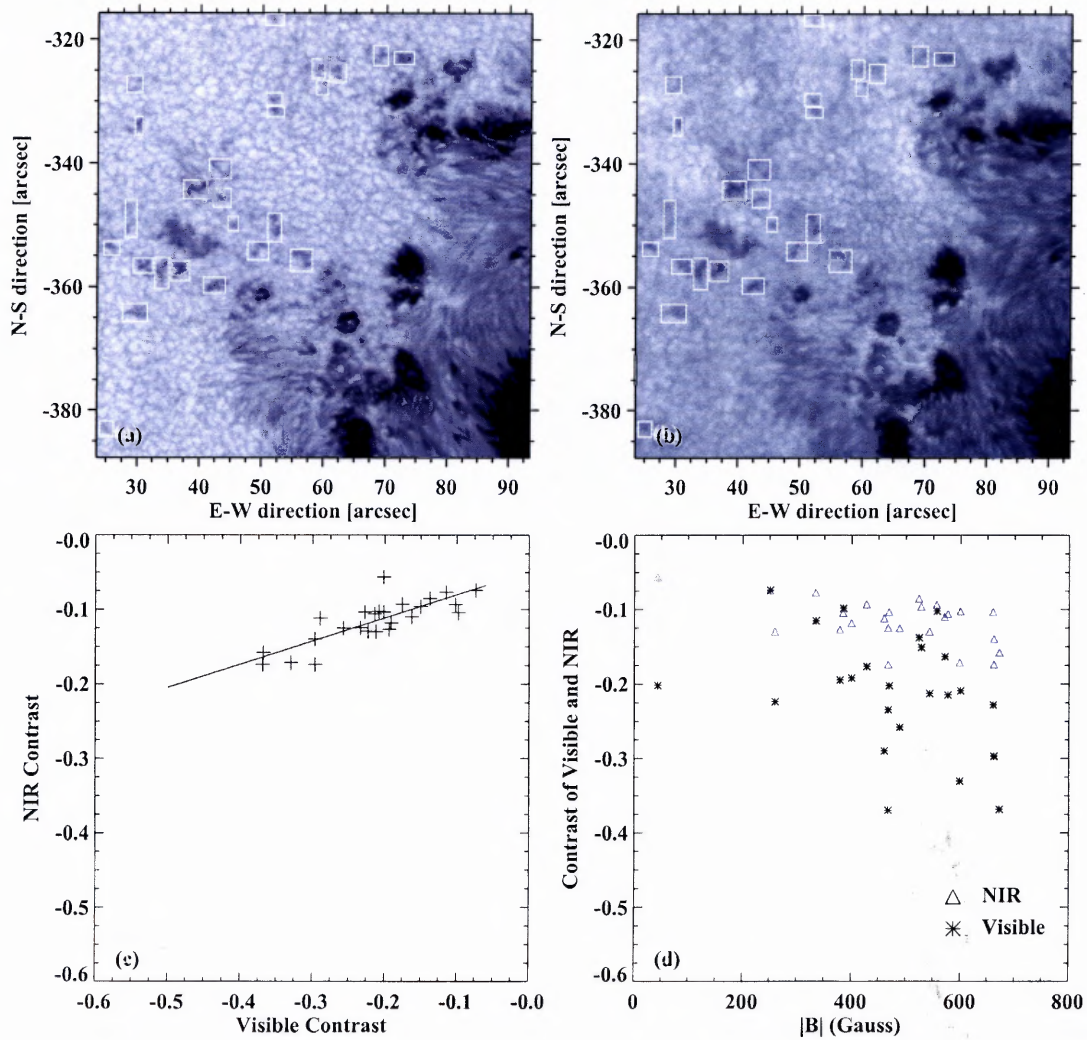


**Figure 3.13** Snapshot of active region NOAA 10486 on 2003 October 29. (a) NIR filtergram at 20:58 UT and (b) Visible light filtergram at 20:58 UT. The two images have the same FOV. Sub-areas marked by white boxes are dark pores selected visually. (c) The lowest contrasts of these small areas in the NIR are plotted as a function of those in visible. The straight line shows the linear fit of this plot. (d) Contrasts versus the absolute value of the corresponding magnetic flux density.

different, we limit the data analysis to a common FOV, which is same as the NIR, i.e., the visible images were demagnified and the MDI data was enlarged. Detailed information of the data sets and the comparison with other observations is listed in Table 3.5.

### 3.4.2 Data Analysis and Result

Figure 3.11, Figure 3.12, and Figure 3.13 show the images obtained in the NIR and visible wavelength bands taken on 2004 December 1, 2 and 2003 October 29.

#### *Relationship Between the Contrasts at NIR and Visible*

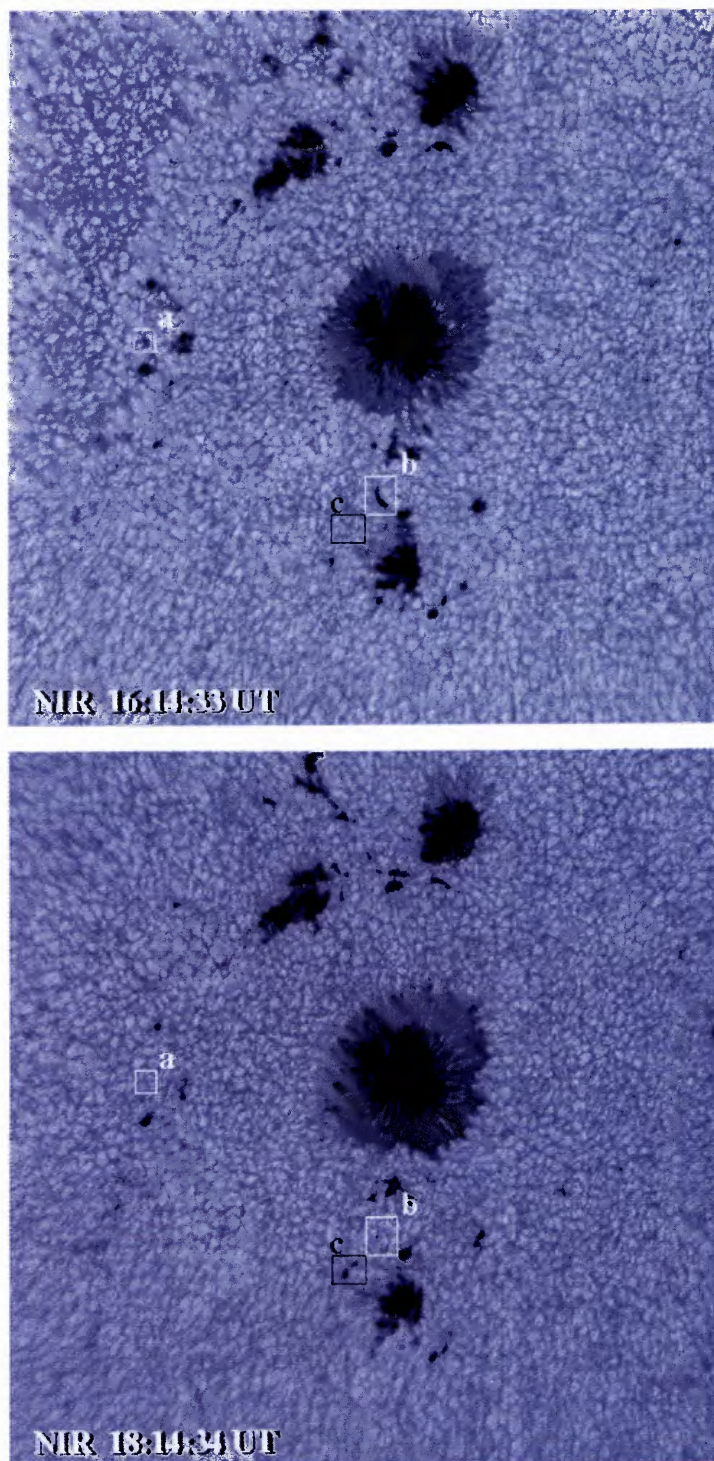
Figure 3.11(a) shows one of the best NIR frames of NOAA 10707 at 17:50 UT on 2004 December 1. This sunspot group was located at  $\mu \simeq 0.89$ . Figure 3.11(b) shows the same area in the visible. All the small pores that are darker than the surroundings are selected visually from the NIR image and marked with white boxes. Note that since dark faculae should have negative contrasts in the NIR and since our data sets have the highest spatial resolution, all the potential dark faculae candidates are selected. Corresponding features are marked accordingly with white boxes in the visible image. We show the correlation between peak negative contrasts of these small pores in the NIR and visible in Figure 3.11(c). All dark structures appearing in NIR images are also observed as dark structures in the visible light images. In addition, these small pores are darker in the visible than in the NIR. This contrast difference is also plotted in the same figure as a simple linear fit. The ratio between NIR contrasts and visible contrasts is about 0.5. A similar analysis has been performed for the other two data sets (see Figure 3.11 and Figure 3.12). Again, none of the selected features are bright in visible, i.e., we could not find any “dark faculae”. The contrast ratio in the two different wavelength ranges are 0.5 and 0.3 on 2004 December 1 and 2003 October 29, respectively.

Figure 3.14 shows two NIR images taken at 16:14 UT and 18:14 UT on 2004 De-

Table 3.5 Observation Details and Comparison with Previous Observations

Observation	Date	AR	$\mu$	$\lambda$ (nm)	$\Delta\lambda$ (nm)	Image Scale	Simultaneous?	DF?
Data set I	2004/12/01	NOAA 10707	0.89	1560	0.25	0.2"	Yes	No
Data set II	2004/12/02	NOAA 10707	0.75	1560	0.25	0.2"	Yes	No
Data set III	2003/10/29	NOAA 10486	0.92	1560	5	0.2"	Yes	No
Xu et al. (2004b)	1999/04/19	NOAA 8518	0.72	1560	50	0.6"	Yes	No
	1999/04/20	NOAA 8518	0.82	1560	50	0.6"	Yes	No
	1999/04/25	NOAA 8518	0.85	1560	50	0.6"	Yes	No
	1996/08/01	SPO 7981	$\geq 0.85$	1570	70	0.5"	Yes	No
Foukal et al. (1990)	1988/06/12	SPO 7657	$\geq 0.87$	1627.4	4	2.6"	No	Yes
	1988/06/12	SPO 7658	$\geq 0.83$	1627.4	4	2.6"	No	Yes
Foukal et al. (1989)	1988/03/29	SPO 7604	0.85	1627.4	4	3"	No	Yes

Note. —  $\lambda$  stands for the center wavelength,  $\Delta\lambda$  denotes the bandpass and DF indicate if Dark Faculae were detected.



**Figure 3.14** Two NIR images taken on 2004 December 2 at 16:14 UT and 18:14 UT. Sub areas marked (a), (b), and (c) show the evolution of small pores. This evolution can be misinterpreted as “dark faculae”.

ember 2, respectively. Small areas (a) and (b), which are marked with white boxes include two disappearing pores. A pore is forming within area (c). The evolution of these changing structures can also be seen in the visible and would lead to misinterpretations, considering the time difference were about six and two hours in previous observations, respectively. For instance, when a NIR image at 16:14 UT is being compared with a visible image at 18:14 UT, we see structures within areas (a) and (b) are dark in the NIR but bright in the visible. However, it shows the evolution of small pores instead of the geometric structure proposed by the definition of “dark faculae”.

### *Contrasts Versus Magnetic Flux Density*

In addition to the contrast comparison, we also studied the magnetic properties of these NIR and visible dark features. Because of the limited resolution of the MDI magnetograms, actual field strength of small flux tubes can not be measured directly. Instead, we measure the mean magnetic flux densities, i.e., the true field strength multiplied by a filling factor.

Contrasts in the NIR and visible versus the corresponding magnetic flux density are plotted in the lower-right panels of Figure 3.11, Figure 3.11 and Figure 3.12. Based on the models of small flux tubes, the magnetic field strength is correlated with the darkness of flux tubes, i.e., the stronger the magnetic field, the darker the flux tubes. The contrasts and magnetic flux density are not correlated very well. The discrepancy between our result and the theoretical models can be explained by an insufficient number of sample points. In a plot including all of the FOV, a better correlation will appear. In addition, we also need to take the filling factor of the intensity measurements into account. A detailed study of contrast of small magnetic structures as a function of their field strength will be presented in a separate paper.

### 3.4.3 Discussion

In this study, two data sets of pure NIR continuum at  $1.56 \mu\text{m}$  are compared with the corresponding visible data and MDI magnetograms. Our data using a new filter with a  $2.5 \text{ \AA}$  bandpass shows that there are no dark structures in the NIR appearing as bright structures in the visible light. An additional data set including image at  $1.56 \mu\text{m}$  with a bandpass of  $5 \text{ nm}$  shows the same result. Absorption lines within the  $5 \text{ nm}$  bandpass do not affect the conclusion that “dark faculae” do not exist in our data sets. Previous studies that found the “dark faculae” were using  $1.63 \mu\text{m}$  data instead of our  $1.56 \mu\text{m}$  observations. However, such a wavelength difference only result a depth difference of  $5 \text{ km}$ , which is not a crucial issue in the current discussion (Wang et al. 1998). In addition, we found that the life time of such small pores is in the order of few hours and one minute cadence is enough to track their evolution. If the comparison of the NIR and visible image is not strictly simultaneously, the emergence or the disappearance of dark pores will be misinterpreted as “dark faculae”. We summarize our most important result as follow: no “dark faculae” could be identified in our observations, i.e., facular points do not show opposite contrasts in two layers that are about  $50 \text{ km}$  apart.

## CHAPTER 4

### SUMMARY

This dissertation has presented several unprecedented data sets obtained at BBSO and NSO/SP. By taking the advantages of the state-of-the-art NIR imaging system developed by the Center for Solar-Terrestrial at NJIT and the HOAO system at NSO/SP, two important topics in solar physics are studied in details. One is the white-light flares and the other is faculae.

In Chapter 2, the very first NIR observations of two white-light flares are presented and related measurements are given, as well as the comparison with current flare models. These kind of observations were sought by other solar physicists for more than 30 years (Hudson 1972; Ohki & Hudson 1975) without success, As mentioned, the NIR emission during a white-light flare provides new information and additional constrains for understanding the physics of particle acceleration, energy transportation and heating processes associated with solar flares. In addition to the NIR images, visible continuum and G-band imaging systems were monitoring the same events simultaneously. Significant brightness enhancements were found in all the wavelengths during two event peaks. They are much higher than the prediction of current flare models, particularly, back-warming and  $H^-$  heating models (Metcalf et al. 1990b; Ding 2003a; Xu et al. 2004a, 2005b). By comparing with RHESSI observations, it is clear that the electrons were accelerated to extremely high energy greater than 800 keV which have never been found before. As an evidence, the derived electric fields, which are regarded as the sources of particle acceleration, show largest strengths in literature with an average value of 22 to 23  $V\text{ cm}^{-1}$ . Furthermore, the calculation shows that the original electron precipitation model alone can not explain the observed flare heating. The comparison of light curves in the NIR and RHESSI HXR and the presence of core-halo structures led us to a combined model, which put three flare

models together to interpret what we have observed, especially in the NIR band. The measurements provided in this part will benefit the future theoretical study of WLFs. Certainly, new observations and numerical simulation are necessary to lead further advances.

The second contribution of this dissertation is to demonstrate the non-existence of “dark faculae”. In Chapter 3, a preliminary statistical study of facular property is presented. The result is consistent with Wang et al. (1998) that facular points are always brighter than the background in both NIR and visible continua, but our data are diffraction limited. When the magnetic fields exceed a certain threshold, the small-scale magnetic structures become pores which is darker than the quiet sun area. With the sub-arcsecond resolution, the magnetic threshold in terms of flux density is about 200 G. Furthermore, the very first “line-free” NIR continuum images are presented in this chapter. These images provide the information fully coming from the deepest layer of photosphere. With the diffraction limited resolution, our more comprehensive investigation shows that no “dark faculae” can be found. The previous observed “dark faculae” are believed to be unresolved pores or as a result of non-simultaneous observations in different wavelengths. This finding will also provide important constrains in distinguishing among the magnetic flux tube models.

## REFERENCES

- Abouadarham, J., & Hènoux, J. C. 1986, *Astron. Astrophys.*, 156, 73.
- Abouadarham, J., & Hènoux, J. C. 1987, *Astron. Astrophys.*, 174, 270.
- Abouadarham, J., & Hènoux, J. C. 1989, *Sol. Phys.*, 121, 19.
- Aschwanden, M. J. 2002, *Particle acceleration and kinematics in solar flares*, Kluwer Academic Publishers.
- Benka, S. G. & Holman, G. D. 1994, *Astrophys. J.*, 435, 469.
- Berger, T. E. & Title, A. M. 2001, *Astrophys. J.*, 553, 449.
- Bromund, K. R., McTiernan, J. M., & Kane, S. R. 1995, *Astrophys. J.*, 455, 733.
- Brown, J. C. 1971, *Sol. Phys.*, 18, 489.
- Canfield, R. C., Gunkler, T. A., & Ricchiazzi, P. J. 1984, *Astrophys. J.*, 282, 296.
- Canfield, R. C., & Gayley, K. G. 1987, *Astrophys. J.*, 422, 999.
- Cao, W., Xu, Y., Ma, J., Denker, C., & Wang, H. 2005a, *SPIE*, in press.
- Cao, W., Hartkorn, K., Ma, J., Xu, Y., Wang, J., Spirock, T. J., & Wang, H. 2005b, *Sol. Phys.*, submitted.
- Cao, W., Ma, J., Xu, Y., Denker, C., Wang, H., & Goode, P. R. 2005c, *Astrophys. J.*, submitted.
- Chandrasekhar, S. & Breen, F. H. 1946, *Astrophys. J.*, 104, 430.
- Chapman, G. 1979, *Astrophys. J.*, 232, 923.
- Chapman, G. A., Cookson, A. M., & Dobias, J. J. 1997, *Astrophys. J.*, 482, 541.
- Chen, Q. R. & Ding, M. D. 2005, *Astrophys. J.*, 618, 537.
- Cheng, C. Z., Ren, Y., Choe, G. S., & Moon Y. J. 2003, *Astrophys. J.*, 596, 1341.
- Cook, J. W. 1979, *Astrophys. J.*, 234, 378.
- Cox, A. N. 2000, *Allen's Astrophysical Quantities*, Springer.
- Crosby, N. B., Aschwanden, M. J., & Dennis, B. R. 1993, *Sol. Phys.*, 143, 275.
- Crosby, N. B., Vilmer, N., Lund N., & Sunyaev R. 1998, *Astron. Astrophys.*, 212, 561.
- Cuberes, M., Vázquez, M., Bonet, J. A., & Sobotka, M. 2002, *Astrophys. J.*, 570, 886.

- Deng, N., Liu, C., Yang, G., Wang, H., & Denker, C. 2005a, *Astrophys. J.*, 623, 1195.
- Deng, N., Xu, Y., Yang, G., Cao, W., Rimmele, T. R., Wang, H., & Denker C. 2005b, *Astrophys. J.*, submitted.
- Denker, C., Ma, J., Wang, J., Didkovsky, L. V.; Varsik, J. R., Wang, H., & Goode, P. R. 2003, *SPIE*, 4853, 223.
- Denker, C., Mascarinas, D., Xu, Y., Cao, W., Yang, G., Wang, H., & Goode, P. R. 2005, *Sol. Phys.*, 227, 217.
- Dennis, B. R. 1985, *Sol. Phys.*, 100, 465.
- Dennis, B. R. & Zarro, D. M. 1993, *Sol. Phys.*, 146, 177.
- Devore, C. R. & Sheeley, N. R. Jr. 1987, *Sol. Phys.*, 108, 47.
- Ding, M. D., Fang, C., Gan, W. D., & Okamoto, T. 1994, *Astrophys. J.*, 429, 890.
- Ding, M. D., Fang, C., & Yun, H. S. 1999, *Astrophys. J.*, 512, 454.
- Ding, M. D. 2003a, *J. Korean Astro. Soc.*, 36, 49.
- Ding, M. D., Liu, Y., Yeh, C. T., & Li, P. J. 2003b, *Astron. Astrophys.*, 403, 1151.
- Doughty, N. A. & Fraser, P. A. 1966a, *Monthly Notices of the Royal Astronomical Society*, 132, 267.
- Doughty, N. A., Fraser, P. A., & McEachran, R. P. 1966b, *Monthly Notices of the Royal Astronomical Society*, 132, 255.
- Dunn, R. B. & Zirker, J. B. 1973, *Sol. Phys.*, 33, 281.
- Elson, J. M., Bennett, H. E., & Bennett, J. M. 1979, in R.R. Shanon and J. C. Wyatt (Eds), *Applied Optics and Optical Engineering*, Acad. Press New York, p.191.
- Elste, G. 1985, in *Theoretical Problems in High Resolution Solar Physics* ed. H.Schmidt (MPA Report 212), 185.
- Emslie, A. J. 1978, *Astrophys. J.*, 224, 241.
- Fligge, M., Solanki, S. K., & Unruh, Y. C. 2000, *Astron. Astrophys.*, 353, 380.
- Forbes, T. G. & Priest, E. R. 1984, in *Solar Terrestrial Physics: Present and Future*, ed. D. M. Butler and K. Paradupoulos (NASA), 1.
- Forbes, T. G., Malherbe, J. M., & Priest, E. R. 1989, *Sol. Phys.*, 120, 285.
- Forbes, T. G. & Acton, L. W. 1996, *Astrophys. J.*, 459, 330.
- Forbes, T. G. & Lin, J. 2000, *Atmos. Sol-Terr. Phys.*, 62, 1499.

- Foukal, P. & Lean, J. 1988, *Astrophys. J.*, 328, 347.
- Foukal, P., Little, R., & Mooney, J. 1989, *Astrophys. J.*, 336, 33.
- Foukal, P., Little, R., Graves, J., Rabin, D., & Lynch, D. 1990, *Astrophys. J.*, 353, 712.
- Foukal, P., Harvey, K., & Hill, F. 1991, *Astrophys. J.*, 383, 89.
- Foukal, P. & Moran, T. 1994, in D. Rabin et al. (eds), *Infrared Solar Physics*, World Scientific, p. 23.
- Foukal, P. 1996, American Astronomical Society Meeting, 188, 3620.
- Foukal, P., Bernasconi, P., Eaton, H., & Rust, D. 2004, *Astrophys. J.*, 611, 57.
- Frazier, E. N. & Stenflo, J. O. 1972, *Sol. Phys.*, 27, 330.
- Gan, W. Q., Rieger, E., Zhang, H. Q., & Fang, C. 1992, *Astrophys. J.*, 397, 694.
- Golub, L. & Pasachoff, J. M. 1997, *The Solar Corona*, Cambridge University Press.
- Hagyard, M. J., Teuber, D., West, E. A., & Smith, J. B. 1984, *Sol. Phys.*, 91, 115.
- Handy, B. N., Acton, L. W., Kankelborg, C. C., Wolfson, C. J., Akin, D. J., Bruner, M. E., Carvalho, R., Catura, R. C., Chevalier, R., Duncan, D. W., & 38 coauthors 1999, *Sol. Phys.*, 187, 229.
- Hartkorn, K. 2003, Application of Adaptive Optics to the Spectroscopic Investigation of Small-Scale Solar Structures. Ph.D. dissertation, Department of Physics, New Jersey Institute of Technology, Newark, New Jersey, USA.
- Harvey, K. L. & Harvey, J. W. 1976, *Sol. Phys.*, 47, 233.
- Hawley, S. L. & Fisher, G. H. 1994, *Astrophys. J.*, 426, 387.
- Hènoux, J. C., Aboudarham, J., Brown, J. C., van den Oord, G. H. J., van Driel-Gesztelyi, & Gerlei, O. 1990, *Astron. Astrophys.*, 233, 577.
- Hirayama, T. 1974, *Sol. Phys.*, 34, 323.
- Hollweg, J. V. 1984, *Astrophys. J.*, 277, 392.
- Holman, G. D. 1985, *Astrophys. J.*, 293, 584.
- Hudson, H. S. 1972, *Sol. Phys.*, 24, 414.
- Hudson, H. S., Acton, L. W., Hirayama, T., & Uchida, Y. 1992, *PASJ*, 44, 77.
- Jackson, J. D. 1962, *Classical Electrodynamics*, John Wiley & Son, Inc., New York.
- Jing, J., Yurchyshyn, V. B., Yang, G., Xu, Y., & Wang, H. 2004, *Astrophys. J.*, 614, 1054.

- Jing, J., Qiu, J., Lin, J., Qu, M., Xu, Y., & Wang, H. 2005, *Astrophys. J.*, 620, 1085.
- Kane, S. R., Love, J. J., Neidig, D. F., & Cliver, E. W. 1985, *Astrophys. J. Lett.*, 290, L45.
- Kaufmann, P., Correia, E., Costa, J. E. R., & Zodi Vaz, A. M. 1986, *Astron. Astrophys.*, 157, 11.
- Keller, C. U. 1992, *Nature*, 359, 307.
- Keller, C. U., Deubner, F.-L., Egger, U., Fleck, B., & Povel, H. P. 1994, *Astron. Astrophys.*, 286, 626.
- Keller, C. U., Schüssler, A., Vögler, A., & Zakharov, V. 2004, *Astrophys. J. Lett.*, 607, 59.
- Kitahara, T., & Kurokawa, H., 1990, *Solar Phys.* 125, 321.
- Korchak, A. A. 1971, *Sol. Phys.*, 18, 284.
- Kosovichev, A. G. & Zharkova, V. V. 2001, *Astrophys. J.*, 550, 105.
- Kraichnan, R. H. 1976, *Journal of Fluid Mechanics*, 77, 753.
- Kuhn, J., Libbrecht, K., & Dicke, R. 1988, *Science*, 242, 908.
- Künzel, H. 1960, *Astron. Nachr.*, 285, 271.
- Lee, S. W., Lee, J., Yun, H. S., Fang, C., & Hu, J. 1996, *Astrophys. J. Lett.*, 470, 65.
- Leighton, R. B. 1964, *Astrophys. J.*, 140, 1547.
- L'ena, P., Lebrun, F., & Mignard, F. 1998, *Observational Astrophysics*, 2nd ed., Springer.
- Li, X. Q., Song, M. T., Hu, F. M., & Fang, C. 1997, *Astron. Astrophys.*, 320, 300.
- Lin, J., and Forbes, T. G., 2000, *J. Geophys. Res.*, 105, 2375.
- Lin, J., Raymond, J. C., van Ballegooijen, A. A. 2004, *Astrophys. J.*, 602, 422.
- Lin, R. P., Hudson, H. S. 1976, *Sol. Phys.*, 50, 153.
- Lin, R. P., Dennis, B. R., Hurford, G. J., Smith, D. M., Zehnder, A., Harvey, P. R., Curtis, D. W., Pankow, D., Turin, P., Bester, M., & 56 coauthors 2002, *Sol. Phys.*, 210, 3.
- Litvinenko, Y. E. & Somov, B. V. 1993, *Sol. Phys.*, 146, 127.
- Litvinenko, Y. E. 1996, *Astrophys. J.*, 462, 997.
- Litvinenko, Y. E. & Craig, I. J. D. 2000, *Astrophys. J.*, 544, 1101.
- Liu, C., Deng, N., Liu, Y., Falconer, D., Goode, P. R., Denker, C., & Wang, H. 2005, *Astrophys. J.*, 622, 722.

- Liu, Y., Ding, M. D., & Fang, C. 2001, *Astrophys. J.*, 563, 169.
- Livingston, W. 1975, *Bulletin of the American Astronomical Society*, 7, 346.
- Machado, M. E., Emslie, A. G., & Brown, J. C. 1978, *Sol. Phys.*, 58, 363.
- Machado, M. E., Avrett E. H., Falciani R. 1986, in *The Lower Atmosphere of Solar Flares*, ed. D. F. Neidig (Sunspot: NSO/Sacramento Peak), 483.
- Machado, M. E., Emslie, A. G., & Avrett, E. H. 1989, *Sol. Phys.*, 124, 303.
- Mauas P. J. D., Machado, M. E., & Avrett, E. H. 1990, *Astrophys. J.*, 360, 715.
- Mauas P. J. D. 1993, *Astrophys. J.*, 414, 928.
- McClements, K. G. & Brown, J. C. 1986, *Astron. Astrophys.*, 165, 235.
- Mein P. 1966, *Annales d'Astrophysique*, 29, 153.
- Metcalf, T. R., Canfield R. C., Avrett, E. H., & Metcalf, F. T. 1990a, *Astrophys. J.*, 350, 463.
- Metcalf, T. R., Canfield R. C., & Saba, J. L. R. 1990b, *Astrophys. J.*, 365, 391.
- Metcalf, T. R., Alexander, D., Hundon, H. S., & Longcope, D. 2003, *Astrophys. J.*, 595, 483.
- Metcalf, T. R., Leka, K. D., & Mickey, D. L. 2005, *Astrophys. J.*, 623, 53.
- Miller, J. A., Cargill, P. J., Emslie, A. G, Holman, G. D., Dennis, B. R., LaRosa, T. N., Winglee, R. M., Benka, S. G., & Tsuneta, S. 1997, *J. Geophys. Res.*, 102, 14631.
- Moran, T., Foukal, P., & Rabin, D. 1992, *Sol. Phys.*, 142, 35.
- Muller, R. & Roudier, Th. 1984, *Sol. Phys.*, 94, 33.
- Najita, K., & Orrall, F. Q. 1970, *Sol. Phys.*, 15, 176.
- Neidig, D. F. & Cliver, E. W. 1983, *Sol. Phys.*, 88, 275.
- Neidig, D. F. 1989, *Sol. Phys.*, 121, 261.
- Neidig, D. F., Kiplinger, A. L., Cohl, H. S., & Wiborg, P. H. 1993a, *Astrophys. J.*, 406, 306.
- Neidig, D. F., Wiborg, P. H., & Gilliam, L. B. 1993b, *Sol. Phys.*, 144, 169.
- Neidig, D. F., Grosser, H., & Hrovat, M. 1994, *Sol. Phys.*, 155, 199.
- Neupert, W M. 1968, *Astrophys. J.*, 153, 59.
- Ohki, K., & Hudson, H. S. 1975, *Sol. Phys.*, 43, 405.

- Parker, E. N. 1958, Phys. Rev., 109, 1328.
- Parker, E. N. 1972, /apj, 174, 499.
- Parker, E. N. 1979, Astrophys. J., 234, 333.
- Parker, E. N. 1983, Astrophys. J., 264, 642.
- Peckover, R. S. & Weiss, N. O. 1978, Monthly Notices of the Royal Astronomical Society, 182, 189.
- Poletto, G., & Kopp, R. A. 1986, in *The Lower Atmosphere of Solar Flares*, ed. D. F. Neidig (Sunspot: NSO/Sacramento Peak), 453.
- Qiu, J., Lee, J., Gary, D. E., & Wang, H. 2002, Astrophys. J., 565, 1335.
- Qiu, J., Wang, H., Cheng, C. Z., & Gary, D. E. 2004, Astrophys. J., 604, 900.
- Ramaty, R., Kozlovsky, B., & Lingenfelter, R. E. 1975, Space Sci. Rev., 18, 341.
- Rimmele, T. 2000, Proc. SPIE, 4007, 218.
- Rimmele, T. R., Richards, K., Hegwer, S. L., Ren, D., Fletcher, S., Gregory, S., Didkovsky, L. V., Denker, C., Marquette, W., Marino, J., & Goode, P. R. 2003, Proc. SPIE, 4839, 635.
- Rust, D. M., & Hegwer, F. 1975, Sol. Phys., 40, 141.
- Rust, D. M. 1986, *The Lower Atmosphere of Solar Flares*, Neidig, D. F. (Eds), National Solar Observatory.
- Rutten, R. J., Kiselman, D., Rouppe van der Voort, L., & Plez, B. 2001, ASP Conf. Ser., 236, 453.
- Sakurai, K. 1974, Astrophysics & Space Science, 28, 275.
- Schatten, K., Mayr, H., Omidvar, K., & Maier, E. 1986, Astrophys. J., 311, 460.
- Schatten, K. 1988, Geophys. Res. Lett., 15, 121.
- Schatten, K. & Mayr G. 1991, Astrophys. J., 372, 728.
- Scherrer, P. H., Bogart, R. S., Bush, R. I., Hoeksema, J. T., Kosovichev, A. G., Schou, J., Rosenberg, W., Springer, L., Tarbell, T. D., Title, A., Wolfson, C. J., Zayer, I., & MDI Engineering Team 1995, Sol. Phys., 162, 129.
- Sheeley, N. R. Jr., Nash, A. G., & Wang, Y. M. 1987, Astrophys. J., 319, 481.
- Sobotka, M., Vázquez, M., Bonet, J. A.; Hanslmeier, A., & Hirzberger, J. 1999, Astrophys. J., 511, 436.

- Sobotka, M., Vázquez, M., Cuberes, M., & Bonet, J. A. 2000, *Astrophys. J.*, 544, 1155.
- Somov, B. V. & Kosugi, T. 1997, *Astrophys. J.*, 485, 859.
- Spirock, T. J., Yurchyshyn, V. B., & Wang, H. 2002, *Astrophys. J.*, 572, 1072.
- Spruit, H. C. 1976, *Sol. Phys.*, 50, 269.
- Spruit, H. C. & van Ballegooijen, A. A. 1982, *Astron. Astrophys.*, 106, 58.
- Steiner, O., Hauschildt, P. H., & Bruls, J. 2001, *Astron. Astrophys.*, 372, L13.
- Stix, M. 2002, *The Sun*, Springer.
- Tandberg-Hanssen, E. & Emslie, A.G. 1988, *The Physics of Solar Flares*, Cambridge University Press.
- Thomas, V. A., Winske, D., & Omid, N. 1990, *J. Geophys. Res.*, 95, 18809.
- Unsöld, A. & Baschek, B. 1999, *Der neue Kosmos*, 6th ed., Springer.
- Vernazza, J. E., Avrett, E. H., & Loeser, R. 1976, *Astrophys. J. Suppl. Ser.*, 30, 1.
- Vernazza, J. E., Avrett, E. H., & Loeser, R. 1981, *Astrophys. J. Suppl. Ser.*, 45, 635.
- Veronig, A., Vrsnak, B., Dennis, B. R., Temmer, M., Hanslmeier, A. & Magdalenic, J. 2002, *Astron. Astrophys.*, 392, 699.
- Walton, S. R., Preminger, D. G., & Chapman, G. A. 2003, *Astrophys. J.*, 590, 1088.
- Wang, H., Zirin, H. 1987, *Sol. Phys.*, 110, 281.
- Wang, H. & Tang, F. 1993, *Astrophys. J.*, 407, 89.
- Wang, H. 1997, *Sol. Phys.*, 174, 163.
- Wang, H., Spirock, T. J., Goode, P. R., Lee, C., Zirin, H., & Kosonocky, W. 1998, *Astrophys. J.*, 495, 957.
- Wang, H. 2001, *Solar Flare Magnetic Fields*, In: *Encyclopedia of Astronomy and Astrophysics*, Paul Murdin (Eds), article 2287. Bristol: Institute of Physics Publishing.
- Wang, H., Ji, H., Schmahl, E. J., Qiu, J., Liu, C., & Deng, N. 2002a, *Astrophys. J.*, 580, 177.
- Wang, H., Spirock, T. J., Qiu, J., Ji, H., Yurchyshyn, V., Moon, Y., Denker, C., & Goode, P. R. 2002b, *Astrophys. J.*, 576, 497.
- Wang, H., Qiu, J., Jing, J., & Zhang, H. 2003, *Astrophys. J.*, 593, 564.
- Wang, H., Qiu, J., Jing, J., Spirock, T. J., Yurchyshyn, V., Abramenko, V., Ji, H., & Goode, P. R. 2004, *Astrophys. J.*, 605, 931.

- Wang, J., Wang, H., Tang, F., Lee, J., & Zirin, H. 1995, *Sol. Phys.*, 160, 277.
- Wang, J., Wang, H., Goode, P. R., Spirock, T. J., Lee, C., Ravindra, N. M., Ma, J., & Denker C. 2001, *OE*, 1016, 1023.
- Worden, P. 1975, *Sol. Phys.*, 45, 521.
- Xu, Y., Cao, W., Liu, C., Yang, G., Qiu, J., Jing, J., Denker, C., & Wang, H. 2004a, *Astrophys. J. Lett.*, 607, 131.
- Xu, Y., Yang, G., Qiu, J., Spirock, T. J., Jing, J., Denker, C., & Wang, H. 2004b, *Chinese Journal of Astronomy and Astrophysics*, 4, 481.
- Xu, Y., Cao, W., Liu, C., Yang, G., Jing, J., Denker, C., & Wang, H. 2005a, *Astrophys. J.*, 628, 167.
- Xu, Y., Cao, W., Liu, C., Yang, G., Jing, J., Denker, C., & Wang, H. 2005b, *Astrophys. J. Lett.*, in revision.
- Yang, G., Xu, Y., Cao, W., Wang, H., Denker, C., & Rimmele, T. R. 2004, *Astrophys. J.*, 617, 151.
- Yurchyshyn, V., Wang, H., Abramenko, V., Spirock, T. J., & Krucker, S. 2004, *Astrophys. J.*, 605, 546.
- Zhang, H., Scharmer, G., Lofdahl, M. & Yi Z. 1998, *Sol. Phys.*, 183, 283.
- Zhao, J., Kosovichev, A. G., & Duvall, T. L. Jr. 2001, *Astrophys. J.*, 557, 384.
- Zhao, J. & Kosovichev, A. G. 2003, *Astrophys. J.*, 591, 446.
- Zhao, J. & Kosovichev, A. G. 2004a, *Astrophys. J.*, 603, 776.
- Zhao, J. 2004b, *Inference of Solar Subsurface Flows by Time-Distance Helioseismology*. Ph.D. dissertation, Department of Physics, Stanford University, California, USA.
- Zirin, H. 1988, *Astrophysics of The Sun*, Cambridge University Press.
- Zirin, H. & Wang, H. 1992, *Astrophys. J.*, 385, 27.